Katharina Rath, BSc

Overlap Criteria for Drift-Orbit Resonances in Tokamak Plasmas with Non-Axisymmetric Perturbations

MASTERARBEIT

zur Erlangung des akademischen Grades

Diplom-Ingenieurin

Masterstudium Technische Physik

eingereicht an der

Technischen Universität Graz

Betreuer

Ass.Prof. Dipl.-Ing. Dr.techn. Winfried Kernbichler

Mitbetreuer:
Dipl.-Ing. Dr.rer.nat. Christopher Albert, BSc

Institut für Theoretische Physik - Computational Physics

Graz, November 2017

EIDESSTATTLICHE ERKLÄRUNG

Ich erkläre an Eides statt, dass ich die vorliegende Arbeit selbstständig verfasst, andere als die angegebenen Quellen/Hilfsmittel nicht benutzt, und die den benutzten Quellen wörtlich und inhaltlich entnommenen Stellen als solche kenntlich gemacht habe.

Graz, am …………………………   ……………………………………………..
                                                                            (Unterschrift)

STATUTORY DECLARATION

I declare that I have authored this thesis independently, that I have not used other than the declared sources / resources, and that I have explicitly marked all material which has been quoted either literally or by content from the used sources.

……………………………   ……………………………………………..
           date   (signature)

Abstract

Within this thesis, Hamiltonian theory is used to describe the behaviour of non-linear oscillations near resonances and to study resonance overlap and the subsequent appearance of chaotic motion. Two concepts are discussed to study resonance overlap: the intuitive picture of Chirikov [4] and the standard map that represents an infinite set of interacting resonances. The concepts are first tested on a free particle in one dimension with a time-harmonic perturbation. Due to the analogy of trapped and passing orbits in a tokamak to the libration and rotation of the pendulum, the one-dimensional pendulum is studied in more detail. To complete the analogy to the tokamak, a second dimension of free motion is introduced to the pendulum, and a time-independent perturbation is applied in this direction instead. To test the range of validity of NEO-RT [1], drift-orbit resonances are analysed for a typical medium sized circular tokamak and equilibria from the experiment ASDEX Upgrade with ELM control coils with respect to resonance overlap and chaotic motion.

Kurzfassung

In dieser Arbeit werden nichtlineare Oszillationen mittels Hamiltonscher Theorie nahe Resonanzen sowie Resonanzüberlappung und das Auftreten stochastischer Bewegung untersucht. Zwei Konzepte zur Beschreibung von Resonanzüberlappung werden diskutiert: das Überlappungskriterium von Chirikov [4] und die Standard Map, das ein unendlich viele wechselwirkende Resonanzen beschreibt. Zunächst werden die Konzepte an einem freien Teilchen mit zeitharmonischer Störung in einer Dimension getestet und dieses System schließlich zu einem eindimensionalen Pendel erweitert um die Analogie von *trapped* und *passing* Orbits im Tokamak und Libration und Rotation im Pendel auszunutzen. Es wird dann eine zweite Dimension für freie Bewegung eingeführt und eine zeitunabhängige Störung angewendet. Das Modellsystem wird anhand des Überlappungskriteriums analysiert und die Bedingungen für stochastische Instabilität abgeschätzt. Schlussendlich werden Daten für Driftorbitresonanzen von NEO-RT [1] für einen mittelgroßen zirkulären Tokamak und für ASDEX Upgrade auf Resonanzüberlappung und Stabilität analysiert.

Contents

List of Figures

Introduction

Background

In a tokamak, a toroidally symmetric device, fusion power is maximized in the high-confinement mode (H-mode) as the energy confinement time is enhanced substantially. The H-mode has an high edge-plasma pressure gradient resulting in repetitive edge magneto-hydrodynamic instabilities known as *edge-localized modes* (ELMs) that cause a significant heat loss towards the wall of the tokamak. By inducing small resonant magnetic field perturbations (RMPs) via additional coils and thereby inducing chaotic behaviour in the magnetic field lines, the edge pressure gradient can be reduced and ELMs can be mitigated while maintaining the H-mode for highly rotating, low-collisional plasmas [21].

One side-effect of RMPs is the effect of toroidal rotation damping caused by non-ambipolar transport, called *neoclassical toroidal viscous (NTV) torque* in tokamak plasmas with non-axisymmetric magnetic perturbations [1]. Here, NTV torque is governed by resonant transport regimes that are not present in the axisymmetric case. Within a low-collisional plasma the bounce motion itself is not destroyed by collisions, which corresponds to the banana regime in the axisymmetric case. It is important to note that the NTV torque is related to drift-orbit resonances and not to the magnetic resonance of the RMPs. Orbit resonances are guiding-center orbits, where the bounce-averaged toroidal drift frequency is in resonance with the bounce frequency. To describe drift-orbit resonances accurately, Hamiltonian guiding-center theory is well suited, yielding canonical frequencies for the unperturbed system that appear in the resonance condition. The standard formulation for this, based on particle motion in an electromagnetic field, has been developed by [19] and will be sketched here. Depending on the strength of the harmonic of a perturbation corresponding to a specific resonance, non-linear oscillations and trapping occur close to this resonance. This can be described by secular perturbation theory, and is not to be confused with local trapping in a potential well in the perturbed electromagnetic field.

Taking collisions into account, there exist two limiting cases: The quasilinear limit, where a high number of collisions occurs during a non-linear oscillation period, and the non-linear limit, where the full non-linear (super-)oscillation can be completed without collisional decorrelation. In [1], a unified description of low-collisional quasilinear and non-linear resonant transport regimes leading to NTV torque has been developed. It was implemented in the code NEO-RT and benchmarked with NEO-2 [15] that treats

all collisionalities for quasilinear transport regimes. Using Hamiltonian theory, non-linear oscillations of orbit resonances are taken into account. As a restriction for the applicability of the method are well-separated resonances in phase space, this thesis is dedicated to study resonance overlap and the subsequent appearance of chaotic motion, to test the range of validity of the results of [1].

To study resonance overlap, two concepts are discussed here: The intuitive picture of Chirikov [4] and the mathematically more accurate description by the standard map. The former is applicable to any set of resonances but uses more heuristic argumentation, the latter is mathematically more exact, but strictly applies only to an infinite set of resonances of the same amplitude.

The concepts are first tested on a free particle in one dimension with a time-harmonic perturbation. Due to the analogy of trapped and passing orbits in a tokamak to the libration and rotation of the pendulum, the one-dimensional pendulum is studied in more detail. To complete the analogy to the tokamak, a second dimension of free motion is introduced to the pendulum, and a time-independent perturbation is applied in this direction instead.

To test the range of validity of NEO-RT, drift-orbit resonances are analysed with respect to resonance overlap and chaotic motion for a typical medium sized circular tokamak and equilibria from the experiment ASDEX Upgrade with ELM control coils.

Overview

In the first chapter, main concepts from Hamiltonian theory that are used in the following chapters are reviewed. The considered model of a one-dimensional pendulum is introduced and analysed in action-angle coordinates.

Canonical perturbation theory is presented in chapter 2, but fails to describe the system near resonances. Therefore, secular perturbation theory is presented and applied to the one-dimensional pendulum under an external perturbation and extended to a system with n degrees of freedom.

To study an infinite set of interacting resonances, the standard map is used: a set of difference equations that map the dynamics of the Hamiltonian system onto a subspace to easily visualize dynamic trajectories of periodic motion as introduced in chapter 3. Here, the stability of mappings for resonant and non-resonant tori using the Poincaré-Birkhoff and KAM theorem, respectively, is discussed.

A simple criterion for the transition to global stochasticity for the standard map is the *overlap criterion*, introduced by [4], that estimates a critical perturbation strength via the overlap of two resonances. Additionally, a second method is discussed in chapter 4 to determine the border of stability via the examination of linear stability of islands close to a Kolmogorov-Arnold-Moser (KAM) surface.

In chapter 5, different models with external perturbations are described and converted to the standard map. The stochasticity parameter can be calculated and serves as an indication for arising chaos. A numerical analysis of the models is presented in chapter 6 along with a discussion on the resonance width.

Chapter 7 reviews Hamiltonian theory for particle motion in a magnetic field and summarizes the transformation to action-angle variables for the guiding-center motion in the magnetic field of a tokamak as presented in [1].

Finally, data for drift-orbit resonances of NEO-RT [1] are analysed with respect to resonance overlap and stability. Drift-orbit resonances for test cases in a circular tokamak and equilibria from the experiment ASDEX Upgrade with ELM control coils are used for the validation of the results of [1].

Acknowledgements

Chapter 1

Theoretical background

1.1 Hamiltonian mechanics

In this chapter, classical Hamiltonian mechanics are reviewed closely following [9], [14] and [18].

1.1.1 Canonical equations

The Lagrangian $L(\boldsymbol{q},\dot{\boldsymbol{q}},t)$ that depends on n generalised coordinates q^i, n generalised velocities $\dot{q}^i$ and the time t represents a classical mechanical system with n degrees of freedom. The solution of the problem, the trajectory $\boldsymbol{q}(t)$, makes the action functional,

$$S = \int_{t_0}^{t_1} dt\, L(\boldsymbol{q}(t),\dot{\boldsymbol{q}}(t),t), \tag{1.1}$$

extremal. This variational problem is equivalent to a set of n second-order differential equations - the Euler-Lagrange equations,

$$\frac{d}{dt}\left(\frac{\partial L}{\partial \dot{q}^i}\right) - \frac{\partial L}{\partial q^i} = 0. \tag{1.2}$$

The n generalised coordinates q^i and the n generalised velocities $\dot{q}^i$ form a set of $2n$ independent variables that fully describe the trajectories of the system. If the Lagrangian does not explicitly depend on a variable q^i, the variable is called cyclic,

$$\frac{\partial L(\boldsymbol{q},\dot{\boldsymbol{q}},t)}{\partial q^i} = 0, \tag{1.3}$$

and the corresponding generalized momentum,

$$p_i = \frac{\partial L}{\partial \dot{q}^i}, \tag{1.4}$$

is then conserved along the trajectory. Therefore, the solution of the canonical equations for this pair of conjugate variables is trivial and the dimensionality of the problem is reduced by two.

The Hamiltonian H can be defined in terms of the Lagrangian L via a Legendre transformation $(\boldsymbol{q},\dot{\boldsymbol{q}},t) \rightarrow (\boldsymbol{q},\boldsymbol{p},t)$,

$$H(\boldsymbol{q},\boldsymbol{p},t) = p_i \dot{q}^i(\boldsymbol{q},\boldsymbol{p},t) - L(\boldsymbol{q},\dot{\boldsymbol{q}}(\boldsymbol{q},\boldsymbol{p},t),t). \tag{1.5}$$

As the Euler-Lagrange equations in Eq. (1.2) fully describe the motion of the system, Hamilton's canonical equations provide an equivalent description,

$$\dot{q}^i = \frac{\partial H}{\partial p_i}, \tag{1.6a}$$

$$\dot{p}_i = -\frac{\partial H}{\partial q^i}. \tag{1.6b}$$

If the time evolution of a set of $(\boldsymbol{q},\boldsymbol{p})$ is given by Eq. (1.6b), the set is said to be canonical, with p_i and q^i being canonically conjugate variables. If there is no explicit time-dependence of the system, it is called autonomous and the Hamiltonian given in Eq. 1.5 represents the total energy of the system, expressed via generalised coordinates and their conjugate momenta.

1.1.2 Hamiltonian mechanics using differential geometry

Here, the fundamental ideas of differential geometry for Hamiltonian mechanics are introduced for a better understanding of the following sections. A treatment in full detail is given in [14].

The motion of a dynamical system is described by n second order differential equations on the configuration manifold $\mathbb{Q}$. However, the Lagrangian itself depending on q^i and $\dot{q}^i$, is a function on a larger manifold $\boldsymbol{T}\mathbb{Q}$, with $2n$ coordinates. This manifold is usually called the tangent manifold or tangent bundle on $\mathbb{Q}$. It is called tangent bundle because the generalized velocities $\dot{q}^i$ lie along the tangents to all possible trajectories. The tangent bundle is constructed by adjoining to each point q^i the vector space of all possible velocities.

Now, the Lagrangian can be understood as a function on $\boldsymbol{T}\mathbb{Q}$: it assigns to each point $(\boldsymbol{q},\dot{\boldsymbol{q}})$ of $\boldsymbol{T}\mathbb{Q}$ a certain value, independent of the chosen system of generalized coordinates. In contrast to the solutions obtained by the Lagrangian formalism, the solutions of Eq.

1.6b yield local expressions for the trajectories in $\boldsymbol{T}^*\mathbb{Q}$. $\boldsymbol{T}^*\mathbb{Q}$ is the cotangent bundle, also called *phase space* or *phase manifold*.

The difference between those manifolds is that the tangent bundle is formed with $\mathbb{Q}$ and its tangent spaces, whereas the cotangent bundle is formed with $\mathbb{Q}$ and its cotangent spaces. So its fibers consist of covectors[1].

1.1.3 Canonical transformations

Any variable change $(\boldsymbol{q},\boldsymbol{p},t) \rightarrow (\boldsymbol{Q},\boldsymbol{P},t)$ which preserves the Hamiltonian structure of the equations of motion is called *canonical transformation.* The new variables $(\boldsymbol{Q},\boldsymbol{P},t)$ with the new Hamiltonian $K(\boldsymbol{Q},\boldsymbol{P},t)$[2] satisfy Hamilton's canonical equations. Such a transformation preserves the Hamiltonian structure of the dynamical system.

Satisfying Hamilton's equations is equivalent to invariance of the Poisson bracket under a canonical transformation,

$$\{f,g\} = \frac{\partial f}{\partial q^i}\frac{\partial g}{\partial p_i} - \frac{\partial f}{\partial p_i}\frac{\partial g}{\partial q^i}, \tag{1.7}$$

where f and g are arbitrary functions of the generalised coordinates.

Canonical transformations are usually performed using generating functions F_2 transforming the old Hamiltonian H into the new Hamiltonian K by,

$$K(\boldsymbol{Q},\boldsymbol{P},t) = H + \frac{\partial F_2}{\partial t}. \tag{1.8}$$

A method to find an especially useful canonical transformation is the Hamilton-Jacobi method. A system for which this strategy can be carried out is called integrable. A necessary condition for integrability is that there exist n independent integrals of motion that are well behaved functions of the old coordinates. If the trajectories remain in a bounded region of phase space, then the variables have to oscillate in a quasiperiodic fashion.

If a generalised coordinate q^i of a system is cyclic, L and H are independent of this coordinate and the respective conjugate momentum is conserved. Every cyclic coordinate simplifies the problem and reduces the dimension of the problem by two. The reduction in dimensionality can also be understood from the perspective of differential geometry. A cyclic coordinate defines a $(2n-2)$-dimensional submanifold of the cotangent bundle and if the motion starts on the submanifold, it remains on it. Therefore, it is an invariant submanifold for the dynamical system.

---

[1] A covector is a linear functional that map vector fields into functions.
[2] This function is sometimes called Kamiltonian.

If all generalised coordinates are cyclic, the Hamiltonian only depends on the conjugate momenta and the problem is solved completely. To ensure that the new variables are constants of motion, the transformation is chosen in a way that the transformed Hamiltonian K is identically zero. If this is the case, the whole problem is solved completely, as the new variables still satisfy Hamilton's canonical equations with respect to the new Hamiltonian K,

$$\dot{P}_i = -\frac{\partial K}{\partial Q^i} = 0, \tag{1.9}$$

$$\dot{Q}^i = \frac{\partial K}{\partial P_i} = 0. \tag{1.10}$$

According to Eq. 1.8, K will be zero if the generating function F_2 satisfies the equation,

$$K(\boldsymbol{P}(\boldsymbol{p},\boldsymbol{q},t),\boldsymbol{Q}(\boldsymbol{p},\boldsymbol{q},t),t) = H + \frac{\partial F_2}{\partial t} = 0. \tag{1.11}$$

To perform the transformation $(\boldsymbol{p},\boldsymbol{q}) \to (\boldsymbol{P},\boldsymbol{Q})$, we use $F_2(\boldsymbol{q},\boldsymbol{P},t)$ and the following transformation equations,

$$p_i = \frac{\partial F_2}{\partial q^i},$$
$$Q^i = \frac{\partial F_2}{\partial P_i}. \tag{1.12}$$

Using the definition of p_i of Eq. (1.12), we obtain,

$$H\left(\frac{\partial F_2}{\partial \boldsymbol{q}},\boldsymbol{q},t\right) + \frac{\partial F_2}{\partial t} = 0, \tag{1.13}$$

the Hamilton-Jacobi equation to determine the generating function. Usually, F_2 is denoted by S and called *Hamilton's principal function*. This equation is a non-linear, partial differential equation of first order in $n+1$ variables. As in Eq. 1.13 only partial derivatives are present, we suppose there exists a solution of the form,

$$S = S(q^1,...,q^n,\alpha_1,...,\alpha_n,t), \tag{1.14}$$

where α_i are independent constants of integration. The Hamilton-Jacobi equation only determines the $q-$ and $t-$ dependences of the solution, but does not give any information about the momenta. Hence, we choose the integration constants to be the new momenta,

$$
\begin{aligned}
Q^i &= \beta^i = \frac{\partial S(q^i, \alpha_i, t)}{\partial \alpha_i}, & \text{(1.15a)} \\
P_i &= \alpha_i. & \text{(1.15b)}
\end{aligned}
$$

When the Hamilton-Jacobi equation is solved, we obtain at the same time a solution for the problem.

For the physical meaning of the function S, we construct the total time derivative[3],

$$
\frac{dS}{dt} = \frac{\partial S}{\partial q^i} \dot{q}_i + \frac{\partial S}{\partial t} = p_i \dot{q}_i - H = L. \tag{1.16}
$$

Hence, Hamilton's principal function is the integral over the Lagrangian, corresponding to the action.

If the Hamiltonian does not depend on time explicitly, there is a standard procedure to separate the time dependence of S. S can be written as,

$$
S(\boldsymbol{q}, \boldsymbol{P}, t) = W(\boldsymbol{q}, \boldsymbol{P}) - \alpha_1 t, \tag{1.17}
$$

where $W(\boldsymbol{q}, \boldsymbol{P})$ is known as *Hamilton's characteristic function* and α_1 is a constant. The Hamilton-Jacobi equation reduces to,

$$
H\left(\boldsymbol{q}, \frac{\partial W}{\partial \boldsymbol{q}}\right) = \alpha_1, \tag{1.18}
$$

the *time-independent Hamilton-Jacobi equation*. α_1 is equal to the value of the Hamiltonian.[4] This characteristic function generates a canonical transformation in which all the new coordinates are cyclic. Therefore, all new momenta P_i are constants of motion,

$$
\dot{P}_i = -\frac{\partial H}{\partial Q^i} = 0 \rightarrow P_i = \alpha_i. \tag{1.19}
$$

The new Hamiltonian only depends on the momenta, and we get for the equations of motion for $\dot{Q}_i$,

---

[3]The momenta P_i are independent of time.

[4]If there are no explicit time-dependencies, the Hamiltonian is equal to the total energy of the system, such that $\alpha_1 = E$.

$$\dot{Q}_i = \frac{\partial H}{\partial \alpha_i} = \text{const.} \rightarrow Q^i = \Omega_i t + \beta_i, \tag{1.20}$$

where β_i and α_i are integration constants that are determined by the initial conditions of the problem. As we did before, we will examine the physical meaning of the characteristic function W by taking the total time derivative,

$$\frac{dW}{dt} = \frac{\partial W}{\partial q^i} \dot{q}_i = p_i \dot{q}_i. \tag{1.21}$$

W is called an abbreviated action integral[5],

$$W = \int p_i(\boldsymbol{q}, \boldsymbol{\alpha}) dq^i, \tag{1.22}$$

with $p_i(\boldsymbol{q}, \boldsymbol{\alpha})$ as a function of $\boldsymbol{q}$ and contants of motion $\boldsymbol{\alpha}$.

The most commonly used technique for solving the Hamilton-Jacobi equation is the method of separation of variables. It is assumed that the solution can be written as,

$$W(\boldsymbol{q}, \boldsymbol{\alpha}) = \sum_{i=1}^{n} W_i(q^i, \boldsymbol{\alpha}), \tag{1.23}$$

where W_i only depends on one variable q^i. Hence, $H(\frac{\partial W}{\partial q^i}, q^i) = \text{const.}$ and it can be separated into n ordinary differential equations and written in its separated form [18],

$$H = \sum_i H_i \left(\frac{\partial W_i}{\partial q^i}, q^i \right) = \alpha_i. \tag{1.24}$$

Such a system is called completely integrable.

1.1.4 Action-angle variables

If the Hamiltonian is independent of time and completely integrable, it can be written in its separated form (Eq. 1.24) and therefore the Hamilton-Jacobi equation splits into n independent equations,

$$K(\alpha_i) = H_i \left(\frac{\partial W_i}{\partial q^i}, q^i \right) = \alpha_i. \tag{1.25}$$

---

[5]The abbreviated action integral obeys Mauperthuis' principle, a special case of the principle of least action. Here, the shape of the trajectory in generalised coordinates is determined with both endpoint states given and energy conservation along every trajectory.

K is now a function only of the momenta α_i and the corresponding equations of motion can be solved easily. The choice of the new momenta α_i is completely arbitrary and can be changed to any quantity J_i, which are independent functions of α_i, $J_i = J_i(\alpha_i)$.

For systems in which the motion is periodic, we choose the J_i in a very special way and this variation of the Hamilton-Jacobi procedure provides a powerful method of solving those systems. A periodic system is a system in which either p_i and q^i are periodic functions of time with the same period or with p_i being a periodic function of q^i.

- Libration: The orbit is closed, can be contracted to one single point and this type of motion corresponds to a pendulum oscillating around its equilibrium position.

- Rotation: p_i is a periodic function of q^i and this corresponds to a pendulum rotating completely around its support. The orbit is now open.

The trajectories of such periodic systems lie on tori $\mathbb{T}^n$ on the cotangent bundle $\boldsymbol{T}^*\mathbb{Q}$. The tori and the rate at which each curve $\mathcal{C}_i$ of that torus is traversed can be completely specified by the coordinates $(\boldsymbol{\theta}, \boldsymbol{J})$. The idea of action-angle variables in bounded regions is to find new canonical coordinates $(\boldsymbol{\theta}, \boldsymbol{J})$ for which

- *action variable*, $\boldsymbol{J}$, specifies the torus and is therefore an invariant of motion along this phase curve as the tori are invariant manifolds,

$$\dot{J}_i = -\frac{\partial H}{\partial \theta^i} = 0, \tag{1.26}$$

- θ^i specifies the coordinate on the torus and is normalized to increase by 2π each time a curve is traversed,

$$\oint_{\mathcal{C}_i} d\theta^i = 2\pi. \tag{1.27}$$

As θ^i increases by 2π after one trip around $\mathcal{C}_i$, they are only local coordinates and are called *angle variables*. The Hamiltonian is only dependent on $\boldsymbol{J}$ and the conjugate variables $\boldsymbol{\theta}$ have linear time dynamics,

$$\dot{\theta}^i = \frac{\partial H}{\partial J_i} = \Omega_i(J), \tag{1.28a}$$

$$\theta^i(t) = \Omega^i t + \theta_0^i, \tag{1.28b}$$

where Ω^i are frequencies that describe the rate of traversing the $\mathcal{C}_i$ curves and θ_0^i is an integration constant determined by the initial conditions.

Using the characteristic function of the Hamiltonian $W(\boldsymbol{q},\boldsymbol{J})$[6], a canonical transformation $(\boldsymbol{q},\boldsymbol{p}) \rightarrow (\boldsymbol{\theta},\boldsymbol{J})$ variables can be found. The transformation equations read as,

$$p_i = \frac{\partial W}{\partial q^i},$$
$$\theta^i = \frac{\partial W}{\partial J_i}. \tag{1.29}$$

Rewriting Eq. (1.27) using Eq. (1.29),

$$\oint_{\mathcal{C}_i} \frac{\partial^2 W}{\partial q^i \partial J_i} dq^i = \frac{\partial}{\partial J_i} \oint_{\mathcal{C}_i} p_i dq^i = 2\pi, \tag{1.30}$$

hence, the definition for the action variables reads as,

$$J_i = \frac{1}{2\pi} \oint_{\mathcal{C}_i} p_i(\boldsymbol{q},\boldsymbol{\alpha}) dq^i. \tag{1.31}$$

Finally, we can write the equation of motions in action-angle variables,

$$\dot{\theta}^i = \frac{\partial H}{\partial J_i} = \Omega^i, \tag{1.32a}$$

$$\dot{j}^i = -\frac{\partial H}{\partial \theta^i} = 0. \tag{1.32b}$$

1.2 A simple example: pendulum

We will now consider a pendulum of mass m on a rigid, massless rod with position x and (angular) momentum p. The same system represents a particle in a cosine-shaped potential. The Hamiltonian of this one-dimensional system is given by the sum of the kinetic, $E_{\text{kin}} = p^2/2m$, and the potential energy, $U = U_0(1 - \cos x)$,

$$H(p,x) = \frac{p^2}{2m} + U_0(1 - \cos x). \tag{1.33}$$

The equations of motion are given by,

$$\dot{x} = \frac{p}{m}, \tag{1.34a}$$

$$\dot{p} = -U_0 \sin x. \tag{1.34b}$$

---

[6]A generating function of type 2.

As the energy of this system is conserved $H(p,x) = E$, we can rewrite the equations of motion to obtain $p = p(x,H)$,

$$p = \sigma\sqrt{2m(H - U_0(1 - \cos x))}, \qquad (1.35)$$

where $\sigma = \pm 1$ specifies the direction of the motion ($\sigma = +1$ denotes the positive x-direction).

Using Eq. 1.35, Hamilton's characteristic function can be expressed as

$$W = \int dx' p(x,H) = \int_0^{x'} dx' \sigma\sqrt{2m(H - U_0(1 - \cos x))}. \qquad (1.36)$$

The determining factor for the motion of the pendulum is the energy that yields considerable information on the motion of the pendulum. Introducing the parameter κ, the dimensionless pendulum energy,

$$\kappa = \frac{H}{2U_0}, \qquad (1.37)$$

as used in [2], the types of motion can be classified. For $\kappa < 1$, the motion is bounded (libration) between two turning points given by

$$H = U(x^{\pm}) = U_0(1 - \cos x), \qquad (1.38a)$$
$$x^{\pm} = \pm\arccos(1 - 2\kappa). \qquad (1.38b)$$

Otherwise, if $\kappa > 1$, the pendulum is unbounded, but periodic (rotation) and the momentum p is always positive. In the limit $\kappa = 1$, the motion lies on the separatrix that separates the libration from the rotation.

In the phase space of the pendulum shown in Fig. 1.1, there are two singular points at $p = 0$: a stable elliptical singular point at $(0,0)$ and an unstable hyperbolic singular point at $\theta^i = \pm\pi$. Elliptic trajectories are surrounding the elliptic point and remain in its neighborhood, while the hyperbolic trajectories diverge from the hyperbolic fixed point. Considering the motion on the separatrix, we see that the period becomes infinite for the limit $\kappa \to 1$. Also trajectories very close to the separatrix have a similar behaviour.

Here, the Hamiltonian only depends on J and therefore, J is a constant of motion along the phase curve. Along the same lines, we calculate the action by performing the same integral (Eq. 1.31) over an entire period if the motion is unbounded or over an entire cycle if the motion is bounded.

The action variable is obtained by Eq. 1.31,

$$
\begin{aligned}
J &= \frac{1}{2\pi} \int dx' p(x,H) \\
&= \frac{1}{2\pi} \int dx' \sqrt{2m(H - U_0(1 - \cos x))} - \frac{1}{2\pi} \int dx' \sqrt{2m(H - U_0(1 - \cos x))}, \\
&= \frac{1}{\pi} \int dx' \sqrt{2m(H - U_0(1 - \cos x))}.
\end{aligned} \tag{1.39}
$$

The limits of the integration depend on the type of motion, libration or rotation, and are discussed below.

The corresponding conjugate variable to the action J is the angle θ, that is calculated by,

$$
\begin{aligned}
\theta &= \frac{\partial W}{\partial J} = \frac{\partial H}{\partial J}\frac{\partial W}{\partial H} \\
&= \left(\frac{\partial J}{\partial H}\right)^{-1} \frac{\partial}{\partial H} \int_{-x'}^{x'} dx' \sqrt{2m(H - U_0(1 - \cos x))} \\
&= \left(G\frac{\partial J}{\partial E}\right)^{-1} \int_{0}^{x'} dx' \frac{1}{\sqrt{2m(H - U_0(1 - \cos x))}}.
\end{aligned} \tag{1.40}
$$

The canonical frequency Ω corresponds to the bounce frequency ω_b and is related to the bounce time τ_b by

$$
\Omega = \frac{\partial H}{\partial J} = \left(\frac{\partial J(H)}{\partial H}\right)^{-1} = \frac{2\pi}{\tau_b} = \omega_b. \tag{1.41}
$$

1.2.1 Libration

For libration, the turning points are given by Eq. 1.38b. The action is then calculated by integrating forth and back between the turning points,

$$
\begin{aligned}
J &= \frac{1}{2\pi} \int_{-x'}^{x'} dx' p(x,H) \\
&= \frac{1}{2\pi} \int_{-x'}^{x'} dx' \sqrt{2m(H - U_0(1 - \cos x))} - \frac{1}{2\pi} \int_{x'}^{-x'} dx' \sqrt{2m(H - U_0(1 - \cos x))} \\
&= \frac{1}{\pi} \int_{-x'}^{x'} dx' \sqrt{2m(H - U_0(1 - \cos x))} \\
&= \sqrt{U_0 m}\,\frac{8}{\pi}(\mathcal{E}(\kappa) - (1 - \kappa^2)\mathcal{K}(\kappa)),
\end{aligned} \tag{1.42}
$$

where the normalized pendulum energy κ was used. We used the definition of complete elliptic integrals of the first and second kind for the last expression, given by

$$
\begin{aligned}
\mathcal{K}(\kappa) &= \mathcal{F}(\pi/2,\kappa) = \int_0^{\frac{\pi}{2}} \frac{dx}{\sqrt{(1 - \kappa^2 \sin^2 x)}}, & (1.43\text{a}) \\
\mathcal{E}(\kappa) &= \mathcal{E}(\pi/2,\kappa) = \int_0^{\frac{\pi}{2}} \sqrt{(1 - \kappa^2 \sin^2 x)}\, dx. & (1.43\text{b})
\end{aligned}
$$

For the bounded case, the angle variable becomes

$$
\theta = \frac{\pi}{2} \frac{\mathcal{F}(x/2,\kappa)}{\mathcal{K}(\kappa)}. \tag{1.44}
$$

The canonical frequency can be calculated using Eq. 1.41,

$$
\Omega(\kappa) = \sqrt{\frac{U_0}{m}} \frac{\pi}{2\mathcal{K}(\kappa)}. \tag{1.45}
$$

1.2.2 Rotation

For passing orbits, we integrate over one entire period of the motion

$$
\begin{aligned}
J &= \frac{1}{2\pi} \int_{-\pi}^{\pi} dx'\, p(x,H) \\
&= \frac{1}{2\pi} \int_{-\pi}^{\pi} dx' \sqrt{2m(H - U_0(1 - \cos x))} \\
&= U_0 m \frac{4}{\pi} \sqrt{\kappa} \mathcal{E}(\kappa^{-1}). \tag{1.46}
\end{aligned}
$$

The angle variable becomes

$$
\theta = \frac{\pi \mathcal{F}(x/2,\kappa^{-1})}{\mathcal{K}(\kappa^{-1})}, \tag{1.47}
$$

where $\mathcal{F}(x/2,\kappa)$ denotes the incomplete form of $\mathcal{K}$ given in Eq. 1.43a.

The canonical frequency becomes,

$$\Omega(\kappa) = \sqrt{\frac{U_0}{m}} \frac{\pi \kappa}{\mathcal{K}(\kappa^{-1})}. \tag{1.48}$$

As the canonical frequency is indirectly proportional to the elliptic function $\mathcal{K}(\kappa)$, it behaves asymptotically near the separatrix $\kappa = H/2U_0 = 1$. For values near this region, the following series expansion at $\kappa = 1$ has been used,

$$\mathcal{K}(\kappa) \propto -\frac{1}{2} \log|1 - \kappa| + \log(4) \tag{1.49}$$

Hence, we arrive at the following asymptotical expressions for the canonical frequency for the trapped and the passing orbits close to the separatrix,

$$\Omega_t = \sqrt{\frac{U_0}{m}} \frac{\pi}{-\log|1 - \kappa| + 2\log(4)}, \tag{1.50}$$

$$\Omega_p = 2\sqrt{\frac{U_0}{m}} \frac{\pi\sqrt{\kappa}}{-\log|1 - 1/\kappa| + 2\log(4)}, \tag{1.51}$$

where the subindices t and p denote trapped and passing orbits respectively.

The given example of a one dimensional pendulum exhibits the most important property of non-linear oscillators, *non-isochronicity*, the dependence of the free oscillation period or the bounce time on the energy of the system (Fig. 1.1). Moreover, non-linear oscillators are also characterized by their anharmonicity, the presence of higher harmonics of the canonical frequency. As the amplitude of higher harmonics is small for small oscillations, it is valid to approximate a non-linear system with a linear system for small oscillations.
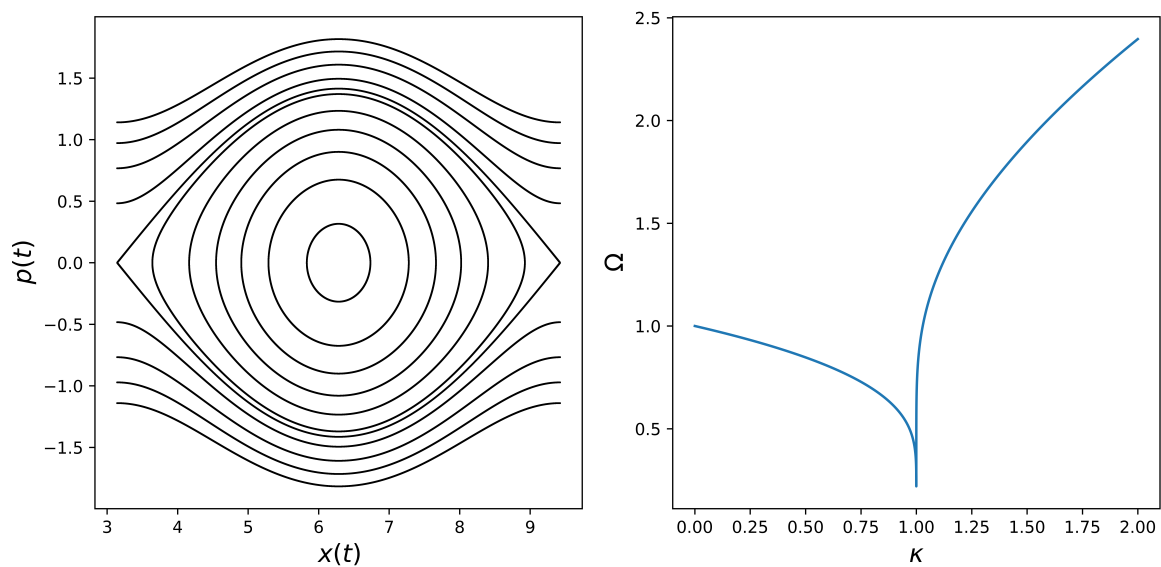
Figure 1.1: Left: Phase space of pendulum motion showing rotation and libration separated by the separatrix. Right: Dependence of the canonical frequency on the normalized energy. It approaches zero at the separatrix, where $\kappa = 1$, as the bounce time τ_b tends towards ∞.

Chapter 2

Canonical perturbation theory

As the majority of nonlinear dynamical problems cannot be solved exactly, methods have been developed to find approximate solutions. One approach introduces perturbations from known, integrable solutions to approximate the insoluble system.

We begin with perturbation theory for an integrable system with one degree of freedom using classical perturbation theory to see the rise of *secular terms* that cause the divergence of the series near resonances. To overcome the resonant denominator, a transformation to a coordinate system rotating with the resonance frequency is performed. This *secular perturbation theory* is described for both an one-dimensional and N-dimensional system.

2.1 Classical perturbation theory

To study non-integrable systems that do not differ much from a similar integrable system, solutions can be found by expanding the generating function in powers of the perturbation parameter and solving the Hamilton-Jacobi equation (Eq. 1.11) for each power separately [18].

The Hamiltonian can be written in terms of the unperturbed Hamiltonian and a sufficiently small perturbation,

$$H(\boldsymbol{J},\boldsymbol{\theta}) = H_0(\boldsymbol{J}) + \epsilon H_1(\boldsymbol{J},\boldsymbol{\theta}), \tag{2.1}$$

where H_0 is the unperturbed Hamiltonian with the N-dimensional actions and angles, $\boldsymbol{J}$ and $\boldsymbol{\theta}$ respectively. H_1 is a multiply periodic function on the canonical angles and given by

$$H_1(\boldsymbol{J}, \boldsymbol{\theta}) = \sum_{\boldsymbol{m}} H_{1m}(\boldsymbol{J})e^{i\boldsymbol{m}\cdot\boldsymbol{\theta}}. \tag{2.2}$$

Here, the system is autonomous. Explicit time dependence can also be treated with this method by introducing an extended phase space [18].

The solution of the equations of motion for the unperturbed Hamiltonian is

$$
\begin{aligned}
\boldsymbol{J} &= \boldsymbol{J}_0, & (2.3)\\
\boldsymbol{\theta} &= \boldsymbol{\Omega}t + \boldsymbol{\beta}, & (2.4)\\
\boldsymbol{\Omega} &= \frac{\partial H_0}{\partial \boldsymbol{J}}, & (2.5)
\end{aligned}
$$

where $\boldsymbol{J}_0, \boldsymbol{\beta}, \boldsymbol{\Omega}$ are constants. A generating function S should now be chosen such that the new Hamiltonian $\bar{H}$ is only a function of new actions $\bar{\boldsymbol{J}}$. We are looking for a generating function of the following type,

$$
S(\bar{\boldsymbol{J}}, \boldsymbol{\theta}) = \bar{\boldsymbol{J}} \cdot \boldsymbol{\theta} + \epsilon \sum_{\boldsymbol{m}} S_{1\boldsymbol{m}}(\bar{\boldsymbol{J}}) e^{i\boldsymbol{m}\cdot\boldsymbol{\theta}}, \tag{2.6}
$$

where the zeroth-order term gives the identity transformation $\boldsymbol{J} = \bar{\boldsymbol{J}}$ and $\boldsymbol{\theta} = \bar{\boldsymbol{\theta}}$. To find the new Hamiltonian, the defining relations, written as a power series in ϵ,

$$
\begin{aligned}
\boldsymbol{J} &= \bar{\boldsymbol{J}} + \epsilon \frac{\partial S_1(\bar{\boldsymbol{J}}, \boldsymbol{\theta})}{\partial \boldsymbol{\theta}}, & (2.7)\\
\bar{\boldsymbol{\theta}} &= \boldsymbol{\theta} + \epsilon \frac{\partial S_1(\bar{\boldsymbol{J}}, \boldsymbol{\theta})}{\partial \bar{\boldsymbol{J}}}. & (2.8)
\end{aligned}
$$

have to be inverted[1],

$$
\begin{aligned}
\boldsymbol{J} &= \bar{\boldsymbol{J}} + \epsilon \frac{\partial S_1(\bar{\boldsymbol{J}}, \bar{\boldsymbol{\theta}})}{\partial \bar{\boldsymbol{\theta}}}, & (2.9)\\
\boldsymbol{\theta} &= \bar{\boldsymbol{\theta}} - \epsilon \frac{\partial S_1(\bar{\boldsymbol{J}}, \bar{\boldsymbol{\theta}})}{\partial \bar{\boldsymbol{J}}}. & (2.10)
\end{aligned}
$$

Expanding Eq. 1.11 to first order, we get

$$
\bar{H}_0(\bar{\boldsymbol{J}}) + \epsilon\bar{H}_1(\bar{\boldsymbol{J}}, \bar{\boldsymbol{\theta}}) = H_0(\boldsymbol{J}(\bar{\boldsymbol{J}}, \boldsymbol{\theta})) + \epsilon \frac{\partial H_0(\bar{\boldsymbol{J}})}{\partial \bar{\boldsymbol{J}}} \frac{\partial S_1(\bar{\boldsymbol{J}}, \bar{\boldsymbol{\theta}})}{\partial \bar{\boldsymbol{\theta}}}. \tag{2.11}
$$

---

[1]The generating function can be written both as $S_1(\bar{\boldsymbol{J}}, \bar{\boldsymbol{\theta}})$ and $S_1(\bar{\boldsymbol{J}}, \boldsymbol{\theta})$, using the transformation $\bar{\boldsymbol{\theta}}(\bar{\boldsymbol{J}}, \boldsymbol{\theta})$.

As the new Hamiltonian $\bar{H}$ should be a function only dependent of $\bar{\boldsymbol{J}}$, S_1 is chosen such that the $\boldsymbol{\theta}$-dependent part of H_1 is eliminated. Therefore, we average the first order terms in Eq. 2.11 over $\bar{\boldsymbol{\theta}}$ to find

$$\bar{H} = H_0(\bar{\boldsymbol{J}}) + \epsilon \langle H_1(\bar{\boldsymbol{J}}, \bar{\boldsymbol{\theta}}) \rangle. \tag{2.12}$$

Hence, the generating function S_1 is given by

$$\boldsymbol{\Omega} \frac{\partial S_1(\bar{\boldsymbol{J}}, \bar{\boldsymbol{\theta}})}{\partial \bar{\boldsymbol{\theta}}} = -H_1(\bar{\boldsymbol{J}}, \boldsymbol{\theta}) + \langle H_1(\bar{\boldsymbol{J}}, \boldsymbol{\theta}) \rangle, \tag{2.13}$$

where $\boldsymbol{\Omega}$ are the canonical frequencies of the unperturbed system. To solve for S_1, Eq. 2.2 is integrated term by term and we get

$$S(\bar{\boldsymbol{J}}, \bar{\boldsymbol{\theta}}) = \bar{\boldsymbol{J}} \cdot \bar{\boldsymbol{\theta}} + i\epsilon \sum_{m \neq 0} \frac{H_{1\boldsymbol{m}}(\bar{\boldsymbol{J}})}{\boldsymbol{m} \cdot \boldsymbol{\Omega}(\bar{\boldsymbol{J}})} e^{i\boldsymbol{m}\bar{\boldsymbol{\theta}}}. \tag{2.14}$$

From the last term it is obvious that S diverges for

$$\boldsymbol{\Omega} \cdot \boldsymbol{m} = 0, \tag{2.15}$$

hence, for every resonance. As for a non-linear oscillator perturbed in real space all harmonics in canonical angles of a perturbation are present, there is a resonance whenever Ω_i/Ω_j is rational.

2.2 Secular perturbation theory

To study a system near a resonance, the resonant denominator has to be eliminated. The idea of *secular perturbation theory* is to canonically transform to a coordinate system that rotates with the resonance frequency to get rid of the resonant denominator.

Again, the Hamiltonian can be written as

$$H = H_0(\boldsymbol{J}) + H_1(\boldsymbol{J}, \boldsymbol{\theta}, t) \tag{2.16}$$

now also allowing for harmonic time dependency, where H_1 represents the perturbation that can be represented by a Fourier series

$$H_1(\boldsymbol{J}, \boldsymbol{\theta}, t) = \sum_{\boldsymbol{m}} H_{\boldsymbol{m}}(\boldsymbol{J}) e^{i(\boldsymbol{m} \cdot \boldsymbol{\theta} - \omega t)}. \tag{2.17}$$

Here, $(\boldsymbol{J}, \boldsymbol{\theta}, \boldsymbol{m})$ are N-tuples, treated as vectors by the notation, where N is the number of degrees of freedom.

The resonance condition of canonical frequencies Ω and perturbation frequency ω has the form

$$\boldsymbol{m} \cdot \boldsymbol{\Omega} - \omega = 0. \tag{2.18}$$

In a system of one degree of freedom, the resonant phase is introduced via a Galilean transformation to get rid of the resonance,

$$\bar{\theta} = m\theta - \omega t + \bar{\theta}_0, \tag{2.19}$$

where the constant $\bar{\theta}_0$ is chosen such that the complex phase of H_m is shifted to a similar expression as we had for the pendulum,

$$\mathfrak{Re}(H_m e^{i(m\theta - \omega t)}) = -|H_m|\cos\bar{\theta}. \tag{2.20}$$

Doing this transformation, we transform now to a coordinate system that rotates with the resonance frequency. To find a set of canonical conjugate variables, we use the generating function of type 2,

$$
\begin{aligned}
F_2(\theta, \bar{J}) &= \bar{J}\bar{\theta}(\theta) \\
&= \bar{J}(m\theta - \omega t + \bar{\theta}_0).
\end{aligned} \tag{2.21}
$$

Hence, we get for the transformed action

$$J = \frac{\partial F_2}{\partial \theta} = m\bar{J}. \tag{2.22}$$

The Hamiltonian becomes,

$$\bar{H}_0(\bar{J}) = H_0 + \frac{\partial F_2}{\partial t} = H_0 - \omega\bar{J}. \tag{2.23}$$

The transformed canonical frequency $\bar{\Omega}$ should vanish at the resonance condition. This can be checked by calculating

$$\bar{\Omega} = \frac{\partial}{\partial \bar{J}}(H_0(\bar{J}) - \omega\bar{J}) = \frac{\partial J}{\partial \bar{J}}\frac{\partial H_0(J)}{\partial J} - \omega = m\Omega - \omega. \tag{2.24}$$

This is exactly the resonance condition given in Eq. 2.18.

We can easily extend this procedure to N dimensions. In contrast to the one-dimensional case, a specific action J_N is now chosen to be replaced by the resonant action as this is sufficient to remove the secularity. Here, we chose J_N to be the resonant action to be definite in notation, but it is possible to choose any action. Again, a generating function of the type

$$F_2(\boldsymbol{\theta},\bar{\boldsymbol{J}}) = \sum_{k \neq N} \bar{J}_k \theta^k + \bar{J} \bar{\theta}^N(\boldsymbol{\theta}), \tag{2.25}$$

which defines a canonical transformation from $(\boldsymbol{J},\boldsymbol{\theta})$ to $(\bar{\boldsymbol{J}},\bar{\boldsymbol{\theta}})$, is used.

The canonical angle is transformed in the same way as in the one dimensional case. However, the non-resonant angles stay the same,

$$\bar{\theta}^N = \boldsymbol{m} \cdot \boldsymbol{\theta} - \omega t + \bar{\theta}_0, \tag{2.26}$$
$$\bar{\theta}^{k \neq N} = \theta^k. \tag{2.27}$$

According to the generating function, the new actions $\bar{J}$ are defined as

$$\bar{J}_N = \frac{J_N}{m_N}, \tag{2.28}$$
$$\bar{J}_{k \neq N} = \bar{J}_k + \frac{m_k}{m_N} J_N. \tag{2.29}$$

The actions $\bar{J}_{k \neq N}$ are invariants of motion and can therefore be omitted in the Hamiltonian, that is now equivalent to the one dimensional case,

$$\begin{aligned} \bar{H}(\bar{\theta},\bar{J}) &= \bar{H}_0(\bar{J}) - |H_{\boldsymbol{m}}(\bar{J})|\cos\bar{\theta} \\ &= H_0(\bar{J}) - \omega\bar{J} - |H_{\boldsymbol{m}}(\bar{J})|\cos\bar{\theta}. \end{aligned} \tag{2.30}$$

As in one dimension, the canonical frequency satisfies the resonance condition,

$$\bar{\Omega} = \frac{\partial}{\partial\bar{J}}(H_0(\bar{J} - \omega\bar{J}) = \frac{\partial J_k}{\partial J}\frac{\partial H_0(J)}{\partial J_k} = \boldsymbol{m} \cdot \boldsymbol{\Omega} - \omega. \tag{2.31}$$

To describe the motion in the vincinty of the resonance, we expand the Hamiltonian around $\bar{\Omega} = 0$ up to quadratic order in $\Delta\bar{J} = \bar{J} - \bar{J}_{res}$. With the expansion of the unperturbed Hamiltonian $\bar{H}_0(\Delta\bar{J})$,

$$\bar{H}_0(\Delta\bar{J}) \;=\; \bar{H}_0(\bar{J}) - \bar{H}_0(\bar{J}_{res}) = \Delta J \frac{\partial \bar{H}_0}{\partial \bar{J}} + \frac{1}{2}\Delta\bar{J}^2 \frac{\partial^2 \bar{H}_0}{\partial \bar{J}^2} \tag{2.32}$$

$$=\; \bar{\Omega}\Delta\bar{J} + \frac{1}{2}\bar{\Omega}'\Delta\bar{J}^2, \tag{2.33}$$

and the evaluation of Eq. 2.30 at $\bar{J} = \bar{J}_{res}$, we arrive at the Hamiltonian of the form

$$\Delta\bar{H}(\bar{\theta},\Delta\bar{J}) = \frac{1}{2}\bar{\Omega}'\Delta\bar{J}^2 - |H_{\boldsymbol{m}}(\bar{J})|\cos\bar{\theta}, \tag{2.34}$$

where we used that the first term in Eq. 2.33 vanishes at the resonance. Performing now a translation by adding $|H_{\boldsymbol{m}}(\bar{J}_{res})|$, we obtain an Hamiltonian of the form of a simple pendulum in $(\bar{\theta}, \Delta\bar{J})$

$$\Delta\bar{H}(\bar{\theta},\Delta\bar{J}) = \frac{1}{2}\bar{\Omega}'\Delta\bar{J}^2 + |H_{\boldsymbol{m}}(\bar{J})|(1 - \cos\bar{\theta}). \tag{2.35}$$

$\bar{\Omega}'$ is the nonlineary parameter of the system defined as,

$$\bar{\Omega}' = \frac{\partial^2 \bar{H}_0}{\partial \bar{J}^2}. \tag{2.36}$$

Hence, near a resonance the motion is similar to that of a pendulum, with libration, rotation and separatrix, shown in Fig. 2.1. This result is the basis for the treatment of chaotic motion in the vincinity of resonances. Eq. 2.35 is therefore called *standard Hamiltonian*.
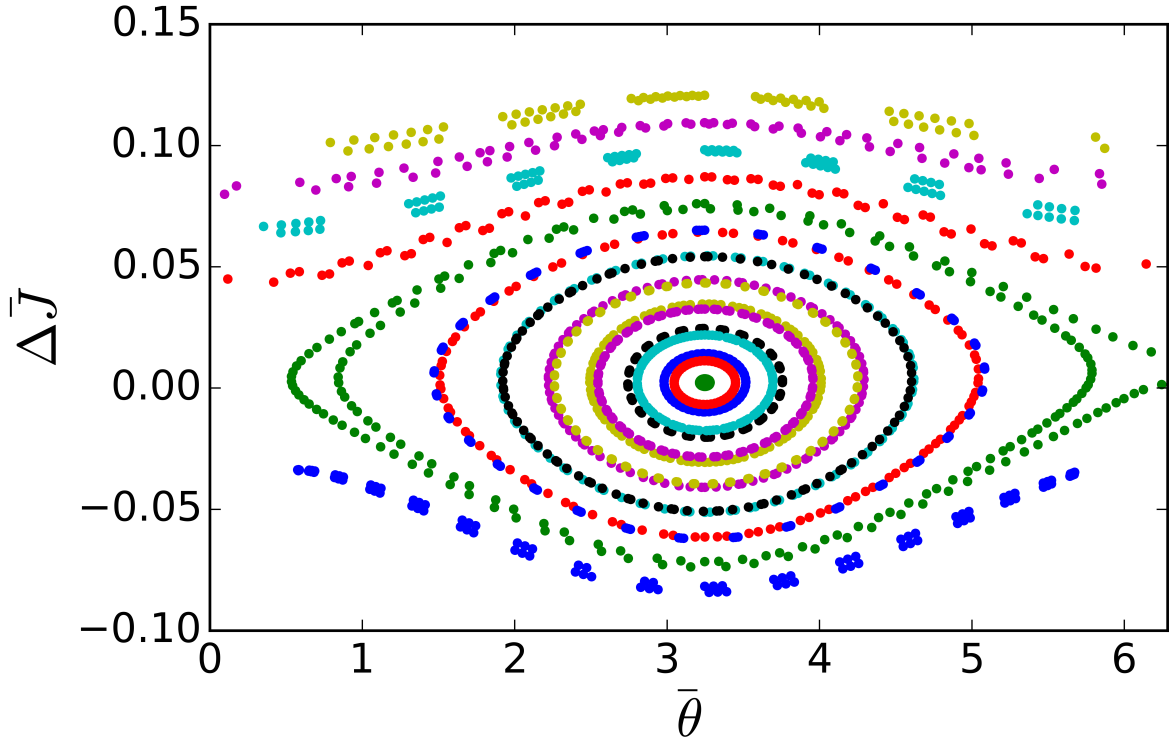
Figure 2.1: Motion in the vicinity of the resonance in the $(\Delta\bar{J}, \bar{\theta})$ phase space. Poincaré cut after an integer number of bounce times.

If the deviation of the action is small enough, the phase trajectories are closed and the pendulum is trapped inside the resonance separatrix. The energy and the phase of the oscillator are varying then in restricted limits; the oscillations are typically referred to *phase oscillations*. The frequency of small phase oscillations is given by

$$\Omega_{\bar{\theta}} = \sqrt{H_m \bar{\Omega}'}. \tag{2.37}$$

Near the resonance, a non-linear oscillator deviates from the exact resonance due to the variation of its frequency. Hence, the non-linearity stabilizes the resonance as the distance from the resonance in phase space along the resonant action is restricted via the variation of its frequency.

The size of the region of the resonance where the motion is trapped is characterized by the width of the separatrix of the resonance as the maximum excursion $\Delta\bar{J}$ occurs at the separatrix (at $\bar{\theta} = 0$),

$$\Delta\bar{J} = 2\left(\frac{|H_m|}{\bar{\Omega}'}\right)^{1/2}. \tag{2.38}$$
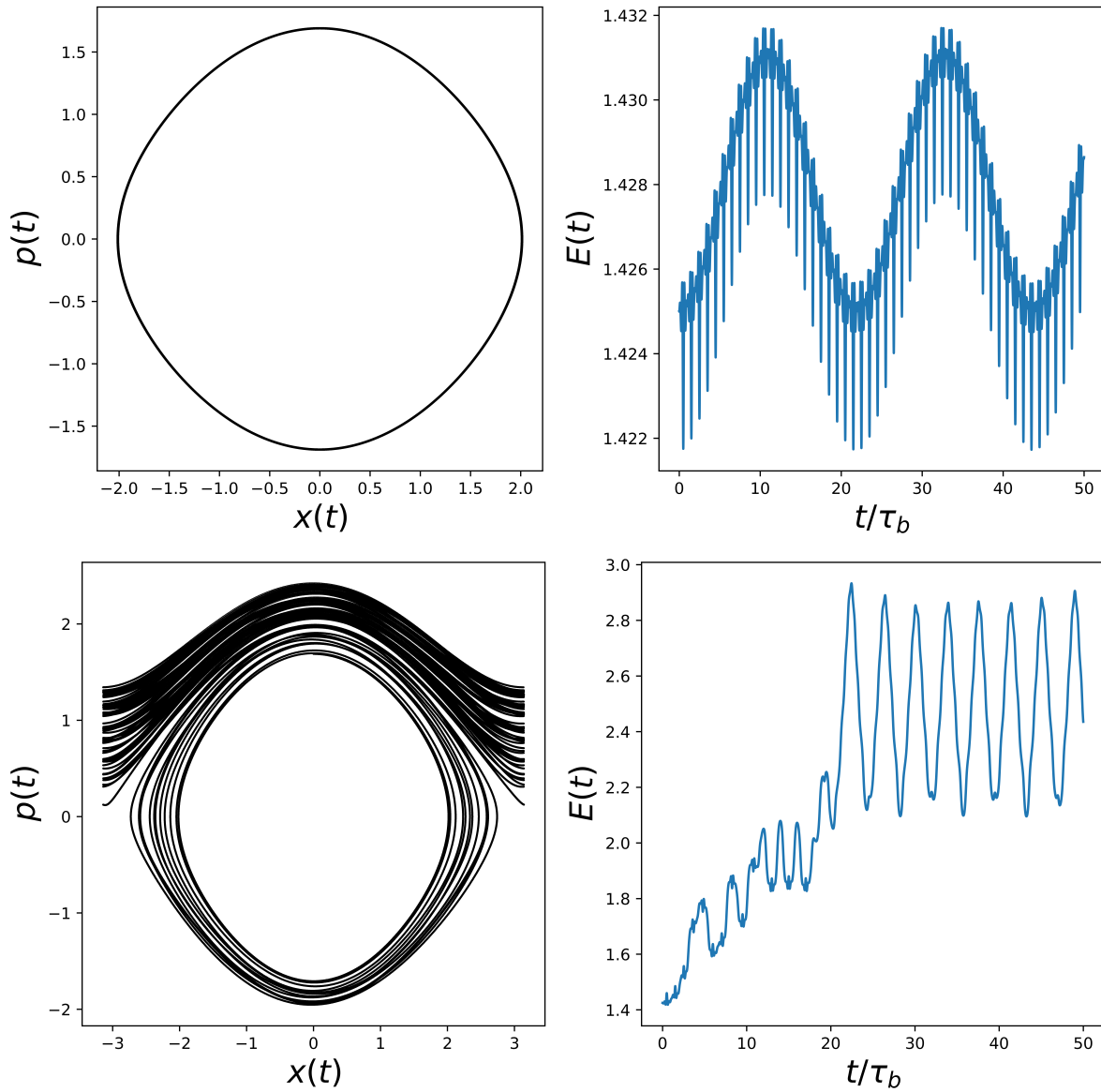
Figure 2.2: Left: Orbits of a pendulum in one dimension near the resonance for $H_m/U_0 = 0.004$ and 0.046 for the upper and lower plot respectively. The mass was set to $m = 1$, the perturbation frequency $\omega = 1.5\omega_0$, where ω_0 is the frequency of the unperturbed system. Right: total energy of the system.

Chapter 3

Mappings

For periodic motion it is convenient to visualize dynamic trajectories by studying inter-
sections of the trajectories with a surface. We can rewrite the Hamiltonian as a set of
difference equations and map the dynamics of a system onto a subspace [18].

In this chapter, we discuss the connections between Hamiltonian systems and mappings
for integrable and near-integrable systems. Several types of mappings are introduced and
how to recover the Hamiltonian description of a system from a mapping is discussed. This
chapter focuses mainly on the standard map introduced by [4] that allows to describe
the interaction of an infinite set of resonances.

Secondly, the properties of stability of the standard map are investigated. For reso-
nant tori, the Poincaré-Birkhoff theorem and the structure of the broken orbits is de-
scribed. Hyperbolic and elliptic fixed points are classified and examined. Finally, the
Kolmogorov-Arnold-Moser theorem (KAM theorem) for non-resonant tori is presented
along with numerical experiments for the standard map.

3.1 Canonical mappings for Hamiltonian systems

3.1.1 Integrable systems

We consider a two dimensional, time independent system,

$$H(J_1, J_2) = E, \tag{3.1}$$

where J_i are constants of motion and E is the conserved energy of the system. The
conjugate variables to J_i are the angles θ^i, that parametrize the motion,

$$\theta^i = \Omega^i t + \theta_0^i, \tag{3.2}$$
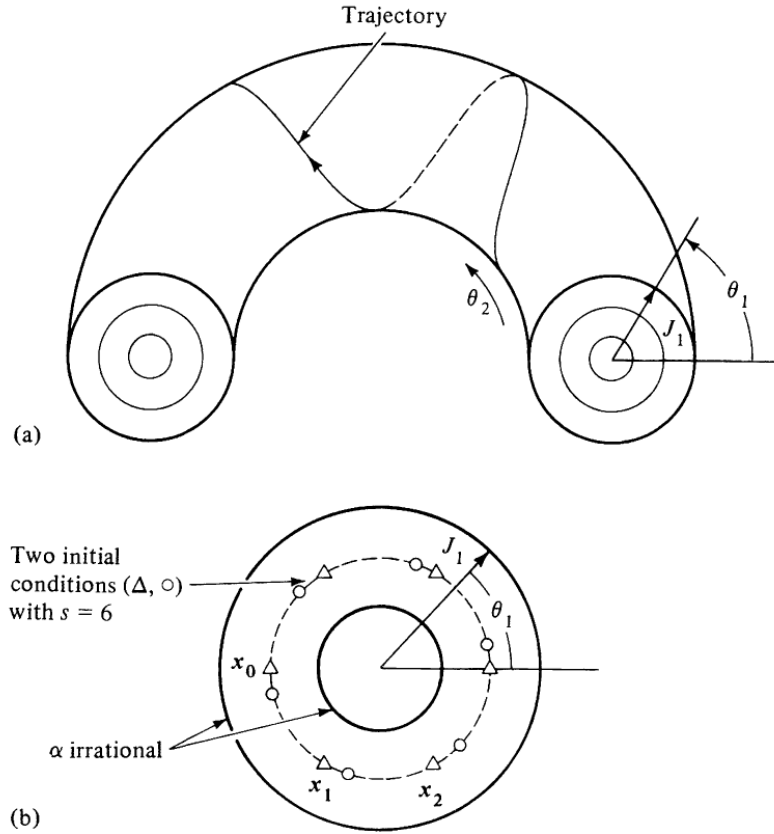
Figure 3.1: Trajectory of a phase space point for an integrable system with two degrees of freedom. (a) Motion on a torus. (b) Mapping of this system for a rational surface ($s = 6$) (from [18]).

with the index $i = (1,2)$ and θ_0^i is the integration constant, dependent on initial conditions. The trajectory can be described as being on a torus in phase space. Fixing the energy E and one of the actions, e.g. J_1, the other action is automatically fixed, and so is the ratio of the frequencies,

$$\alpha = \frac{\Omega^1}{\Omega^2} = \frac{r}{s}. \tag{3.3}$$

The last equality in Eq. 3.3 holds, if r,s are integers and hence, the frequencies are resonant and the motion is then a one dimensional curve on the torus that closes itself after r revolutions in θ^1 and s revolutions in θ^2, as illustrated in Fig. 3.1 (a).

For the examination of phase space trajectories, it is convenient to use a mapping: we set one of the angle variables constant ($\theta^2 = $ const.) and study the intersections of the trajectory on the torus with the $J_1 - \theta^1$ surface of section (Fig. 3.1 (b)). The time between two intersections is $\Delta t = 2\pi/\omega_2$ and θ^1 increases by $\omega_1 \Delta t = 2\pi\alpha$. Using both
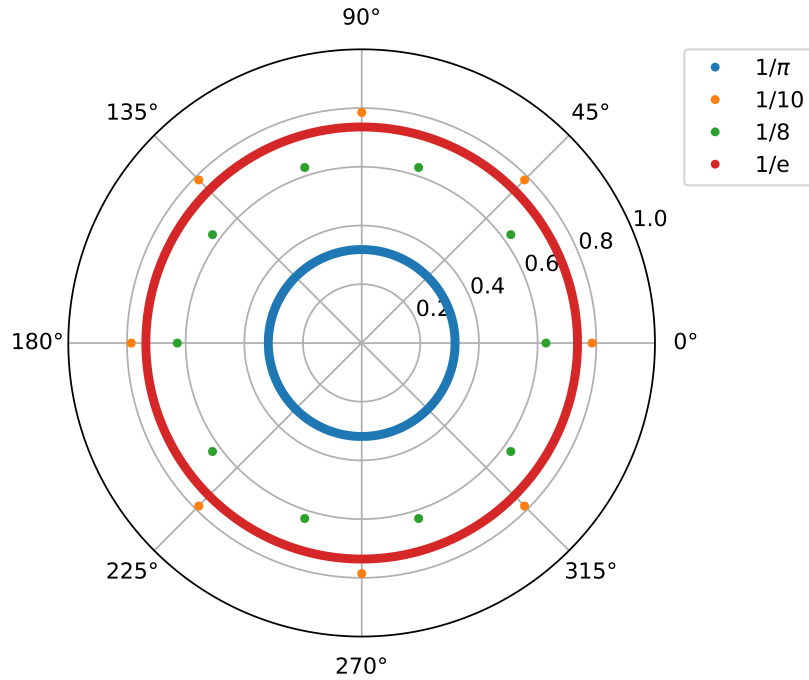
Figure 3.2: Mapping of an integrable system for different rational and irrational surfaces.

expressions and dropping the subscript 1, we arrive at the following set of difference equations describing the motion from the n-th to the $(n+1)$-th intersection,

$$
\begin{aligned}
J_{(n+1)} &= J_{(n)}, & (3.4) \\
\theta_{(n+1)} &= \theta_{(n)} + 2\pi\alpha, & (3.5)
\end{aligned}
$$

where n now is the iteration number. From now on, we keep action and angle fixed. This mapping is of the form of a *twist mapping*, where circles are mapped into circles, but with a rotation number depending on the radius.

As shown in Fig. 3.2, if α is irrational, the mapping fills a circle uniformly as $n \to \infty$. On the contrary, if α is rational, the map has fixed points, reoccuring after s iterations.

3.1.2 Near-integrable systems

A two-dimensional integrable system is perturbed slightly in the following way,

$$
H(\mathbf{J},\boldsymbol{\theta}) = H_0(\mathbf{J}) + \epsilon H_1(\mathbf{J},\boldsymbol{\theta}). \tag{3.6}
$$

If we examine again the $J_1 - \theta^1$ surface of section, we can represent the Hamiltonian in the perturbed twist mapping,

$$
\begin{aligned}
J_{(n+1)} &= J_{(n)} + \epsilon f(J_{(n+1)}, \theta_{(n)}), & \text{(3.7a)} \\
\theta_{(n+1)} &= \theta_{(n)} + 2\pi\alpha(J_{(n+1)}) + \epsilon g(J_{(n+1)}, \theta_{(n)}), & \text{(3.7b)}
\end{aligned}
$$

where f and g are periodic functions in θ. For many mappings $g \equiv 0$ and f is independent of J, we get for Eq. 3.7 the form of a perturbed radial twist mapping,

$$
\begin{aligned}
J_{(n+1)} &= J_{(n)} + \epsilon f(\theta_{(n)}), & \text{(3.8a)} \\
\theta_{(n+1)} &= \theta_{(n)} + 2\pi\alpha(J_{(n+1)}). & \text{(3.8b)}
\end{aligned}
$$

Linearizing the motion about a period 1 fixed point $J_{(n+1)} = J_{(n)} = J_{(0)}$ and introducing $I_{(n)} = 2\pi\alpha\Delta J_{(n)}$ by considering a nearby action $J_{(n)} = J_{(0)} + \Delta J_{(n)}$, Eq. 3.8 transforms into the *Chirikov standard map*,

$$
\begin{aligned}
I_{(n+1)} &= I_{(n)} + K f(\theta_{(n)}) & \text{(3.9a)} \\
\theta_{(n+1)} &= \theta_{(n)} + I_{(n+1)}, & \text{(3.9b)}
\end{aligned}
$$

where K is the stochasticity parameter and f is a periodic function in θ. As can be shown by calculating the Jacobian, this map is an area preserving map. This mapping is a canoncial mapping, generated by the function

$$
F_2 = I_{(n+1)}\theta_{(n)} + \frac{I_{(n+1)}^2}{2} + K\mathcal{F}(\theta_{(n)}), \tag{3.10}
$$

where $f(\theta_{(n)})$ and $\mathcal{F}(\theta_{(n)})$ are related by

$$
f(\theta_{(n)}) = -\frac{d\mathcal{F}(\theta_{(n)})}{d\theta}. \tag{3.11}
$$

As shown in [18], a mapping can be conversed into a Hamiltonian form and vice versa by introducing periodic δ-functions in their Fourier expansion, where the iteration number n is equivalent to the time,

$$
\delta(n) = \sum_{m=-\infty}^{\infty} \delta(n-m) = \frac{1}{2\pi}\left(1 + 2\sum_{m=1}^{\infty}\cos(mn)\right). \tag{3.12}
$$

Using the δ-functions, the equations of motions given in Eq. 3.9 become,

$$
\begin{aligned}
\frac{\partial I}{\partial n} &= Kf(\theta)\delta(n), & (3.13) \\
\frac{\partial \theta}{\partial n} &= I_{(n+1)}. & (3.14)
\end{aligned}
$$

The Hamiltonian represented by the mapping given in Eq. 3.9 can be calculated from,

$$
H(I,\theta,n) = \int^I I'dI' - \frac{K}{2\pi}\delta(n) \int^\theta f(\theta')d\theta' = \frac{\tilde{I}^2}{2} + \frac{K}{2\pi}\mathcal{F}(\theta)\delta(n). \qquad (3.15)
$$

By choosing the perturbation $\mathcal{F}(\theta) = \cos(\theta)$, the Hamiltonian becomes

$$
H(I,\theta,n) = \frac{I^2}{2} + \frac{K}{(2\pi)^2} \sum_{m=-\infty}^{\infty} \cos(\theta - mn). \qquad (3.16)
$$

This Hamiltonian describes the motion of a simple mechanical system known as the *kicked rotator*. The unperturbed system is a plane rigid body that rotates freely in a plane around an axis located in one of its tips. It is perturbed by an external, periodically applied force of fixed magnitude and direction on the other tip. K measures the magnitude of the *kicks*.

It describes an infinite set of non-linear resonances equidistant in phase space. Various dynamical systems can locally be reduced to the standard map and hence, several systems in physics can by approximated by the standard map [5, 12].

3.2 Stability of mappings

Perturbed mappings have different characteristics dependent on the nature of the surface. In the case of rational surfaces, the Poincaré-Birkhoff theorem describes the general behaviour of the structure near this surface. If the winding number is irrational, the KAM theorem is applicable.
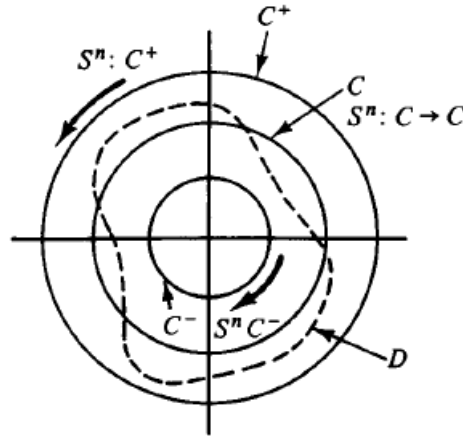
Figure 3.3: Three orbits of the unperturbed Standard map S_0^n ($\mathcal{C}, \mathcal{C}^+, \mathcal{C}^-$) and one orbit of the perturbed map S^n ($\mathcal{D}$) (from [13]).

3.2.1 Rational surfaces - Poincaré-Birkhoff theorem

We consider the unperturbed Standard Map S_0^n given by Eq. 3.9, with $K = 0$, near a rational surface $\mathcal{C} = I/2\pi = r/s$ [14],

$$S_0^n(\theta, I) = (\theta, I). \tag{3.17}$$

This means that the unperturbed standard map maps every point of $\mathcal{C}$ to its original position. For a nearby curve $\mathcal{C}^+$, outside $\mathcal{C}$ $\alpha > r/s$, all points are mapped counterclockwise, on the contrary for the curve $\mathcal{C}^-$ inside the circle $\alpha < r/s$, where the points are mapped clockwise. For all considered regions, the mapping is purely angular, as the radial component I does not change as shown in Fig. 3.3.

If we now consider $K > 0$, but still sufficiently small, the mapping is not purely angular, but the radial component changes: By continuity in K, there must be a closed curve $\mathcal{D}$ between $\mathcal{C}^-$ and $\mathcal{C}^+$, where there exist points whose θ values are not changed by the mapping as shown in Fig. 3.3. Hence, the mapping is defined as

$$S^n : (I(\theta), \theta) \to (i(\theta), \theta). \tag{3.18}$$

If we now map this curve $\mathcal{D}$ again and consider that the map S^n is area-preserving, the region enclosed by $\mathcal{E} = S^n \mathcal{D}$ is the same as the one enclosed by $\mathcal{D}$. They intersect an even number of times and every intersection is a fixed point, as θ does not change. Consequently, S^n has an even number of fixed points on $\mathcal{D}$ and $\mathcal{E}$. It was shown by Poincaré and Birkhoff, that S^n has at least $2n$ fixed points as shown in Fig. 3.4 [13].
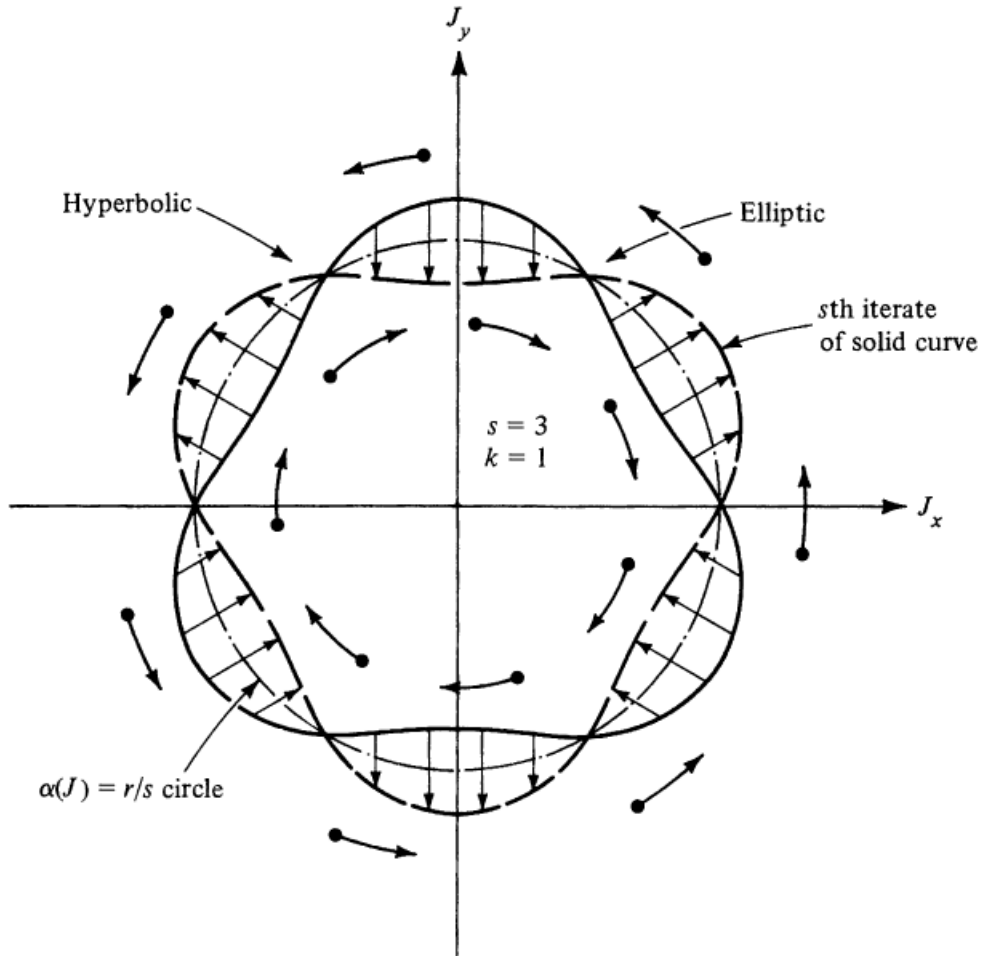
Figure 3.4: Illustration of the Poincaré-Birkhoff theorem: A KAM surface breaks up into $2n$ fixed points for a small perturbation K (from [18]).

To understand the general behaviour of an Hamiltonian system under perturbation, we investigate the nature of those fixed points by the study of the motion in their vicinity. Therefore we calculate the eigenvectors of this map,

$$\begin{vmatrix} \mathcal{J}_{11} - \lambda & \mathcal{J}_{12} \\ \mathcal{J}_{21} & \mathcal{J}_{22} - \lambda \end{vmatrix} = 0, \tag{3.19}$$

with its characteristic equation given by

$$\lambda^2 - \lambda tr(\mathcal{J}) + det(\mathcal{J}) = 0, \tag{3.20}$$

where $det(\mathcal{J}) = 1$ as the map is area-preserving. The eigenvalues are given by

$$\lambda = \frac{1}{2}(tr(\mathcal{J}) \pm \sqrt{(tr(\mathcal{J})^2 - 4)}). \tag{3.21}$$

Two cases have to be analysed,

1. λ_1 and λ_2 are real with $|\lambda_1| \geq 1$ and $|\lambda_2| = |1/\lambda_1| \leq 1$,

2. λ_1 and λ_2 are complex conjugates with $\lambda_{1,2} = exp(\pm i\theta)$.

In case (1), the point is an *hyperbolic* fixed point. This is clear by Fig. 3.4 or when applying the standard map several times to a point in the neighborhood of the hyperbolic point as the mapping moves either inward or outward. For case (2), the considered point is *elliptic*. Here, the mapped point stays in the vincinity of the fixed point and circles around it.

We conclude that all mapped circles that were invariant curves under S_0^n are deformed for the standard mapping S^n, where $K > 0$. They break up into chains of alternating elliptic and hyperbolic fixed points. The hyperbolic points are connected via a separatrix trajectory, whereas the elliptic points are surrounded by closed trajectories.

3.2.1.1 Hyperbolic points

At each hyperbolic point, four curves join belonging to two incoming trajectories of a *stable* ($\mathcal{W}^s$) and two outgoing trajectories of an *unstable* ($\mathcal{W}^u$) manifold [18]. Those manifolds are defined as

$$\mathcal{W}^u = \{x : \lim_{n \to \infty} S^{-n}x = x_0\}, \tag{3.22}$$

$$\mathcal{W}^s = \{x : \lim_{n \to \infty} S^n x = x_0\}, \tag{3.23}$$

with x_0 representing a hyperbolic fixed point. The manifolds $\mathcal{W}^s$ and $\mathcal{W}^u$ cannot cross themselves[1], but they can intersect each other. Again, two cases have to be distinguished: if the intersecting stable and unstable manifold are associated with the same fixed point, the point of intersection is called *homoclinic* point, whereas intersecting manifolds of different fixed points cross at *heteroclinic* points as illustrated in Fig. 3.5. If there is one point of intersection, homoclinic or heteroclinic, there must be an infinite number of intersections[2].

We also have to consider that by approaching the fixed point x_0 the distance between the intersections gets smaller. However, the map is area preserving and consequently

---

[1] follows from invertibility

[2] If x_0 is a heteroclinic point, it is part of both manifolds $\mathcal{W}^s$ and $\mathcal{W}^u$. If we now apply a mapping $S^n x_0$, it must be again an element of both manifolds, as the manifolds map onto themselves.
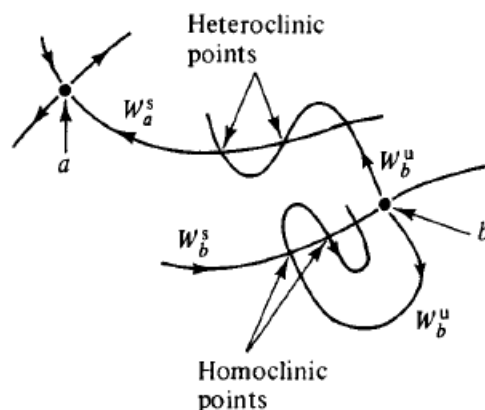
Figure 3.5: Illustration of the hetero- and homoclinic points (from [13]).

the loops have to get longer, leading to even more intersections and a dense set of homoclinic or heteroclinic points as illustrated for one trajectory in Fig. 3.6. As there are also higher order resonances present with their own set of elliptic and hyperbolic fixed points, the oscillating trajectories are filling densely the space. If orbits are intersecting in homoclinic points, no KAM surface[3] can exist at such a point as there is a change in topology of the trajectory as shown in [8]. However, for a sufficient small perturbation, the motion is still bounded between adjacent KAM surfaces.

We have to keep in mind that those curves are not integral curves of the dynamical system, but only intersections of the Poincaré manifold. Hence, points don't move along the manifolds, but rather jump to the next position as illustrated in Fig. 3.7.

3.2.1.2 Elliptic points

In contrast to hyperbolic points, fixed elliptic points are surrounded by isolated closed curves that form barriers to the stable and unstable manifolds of the hyperbolic points. But for $K > 0$, those invariant curves split again into elliptic and hyperbolic fixed points forming an infinite number of higher order resonances (Fig. 3.8). Again there are homoclinic and heteroclinic points that fill the space densely. As was shown in [8], if intersections of orbits are crossing in homoclinic points, an invariant torus in phase space (KAM torus) cannot exist as the trajectory changes its topology. If the perturbation is sufficiently small, not all KAM surfaces break up and hence, the motion is restricted in phase space.

---

[3]A KAM surface is a closed curve in R^2, that is invariant under the mapping, and divides R^2 into two disjoint regions.
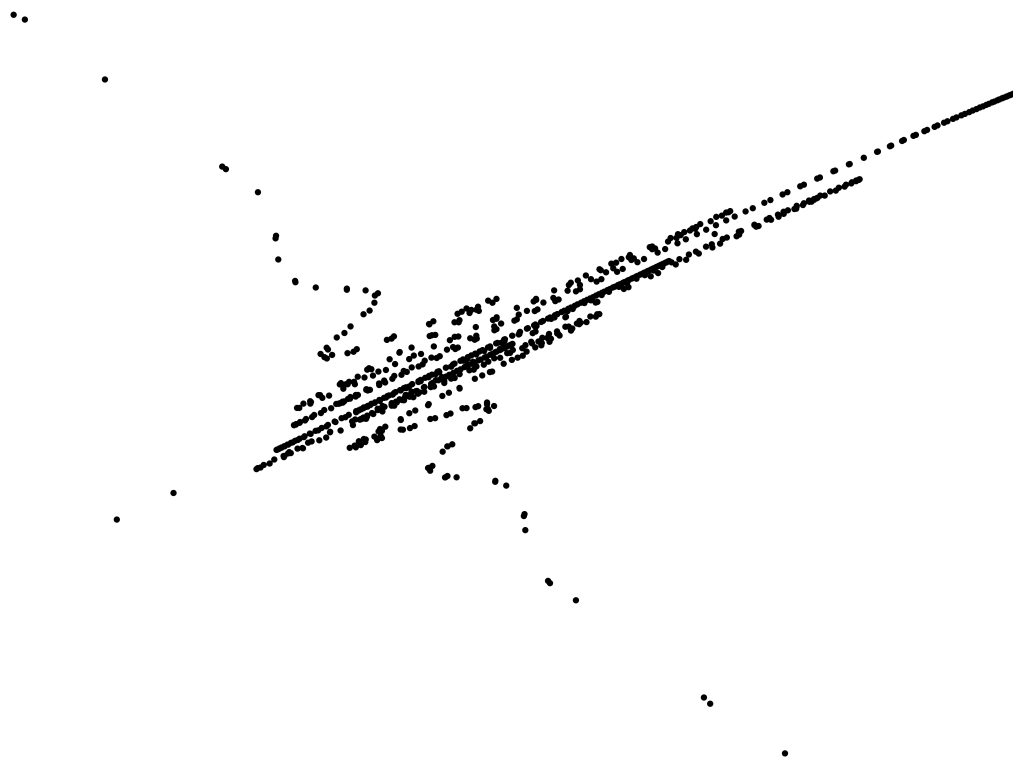
Figure 3.6: Illustration of homoclinic and heteroclinic points near a hyperbolic fixed point. A line segment on $\mathcal{W}^s$ near the fixed point was chosen and mapped for $n = 18$.

3.2.2 Irrational surfaces - KAM theory

After the Poincaré-Birkhoff theorem was published, it was believed that if the resonant tori were destroyed, there would be no hope for the irrational ones. But in 1954, Kolmogorov (later Arnold and Moser) showed that for sufficiently small perturbations, most of the irrational tori are preserved and only slightly deformed. Hence, for most initial conditions the system is stable for small perturbations.

As explained before, a KAM surface is a closed curve in R^2, that is invariant under the mapping, and divides R^2 into two disjoint regions. Thus, a point in the interior cannot map onto the outside, and vice versa. So, as long as a KAM surface is not destroyed, the motion is confined in this surface. Even though the motion can be chaotic, it is restricted in the phase space. Whereby if the KAM surface breaks, there is no longer a restriction for the motion.

The mapping for $K = 0.5$ is shown in Fig. 3.9. The first order fixed points are surrounded by KAM surfaces, represented by solid lines Fig. 3.9 (a) and are calculated using secular
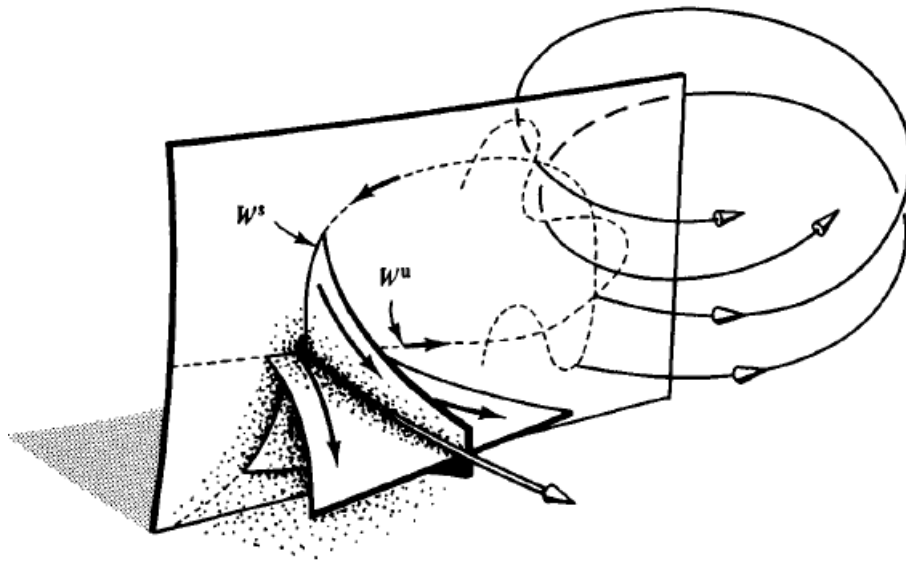
Figure 3.7: Illustration of the trajectories of the mappings resulting in stable and unstable manifolds of hyperbolic fixed points (from [13]).
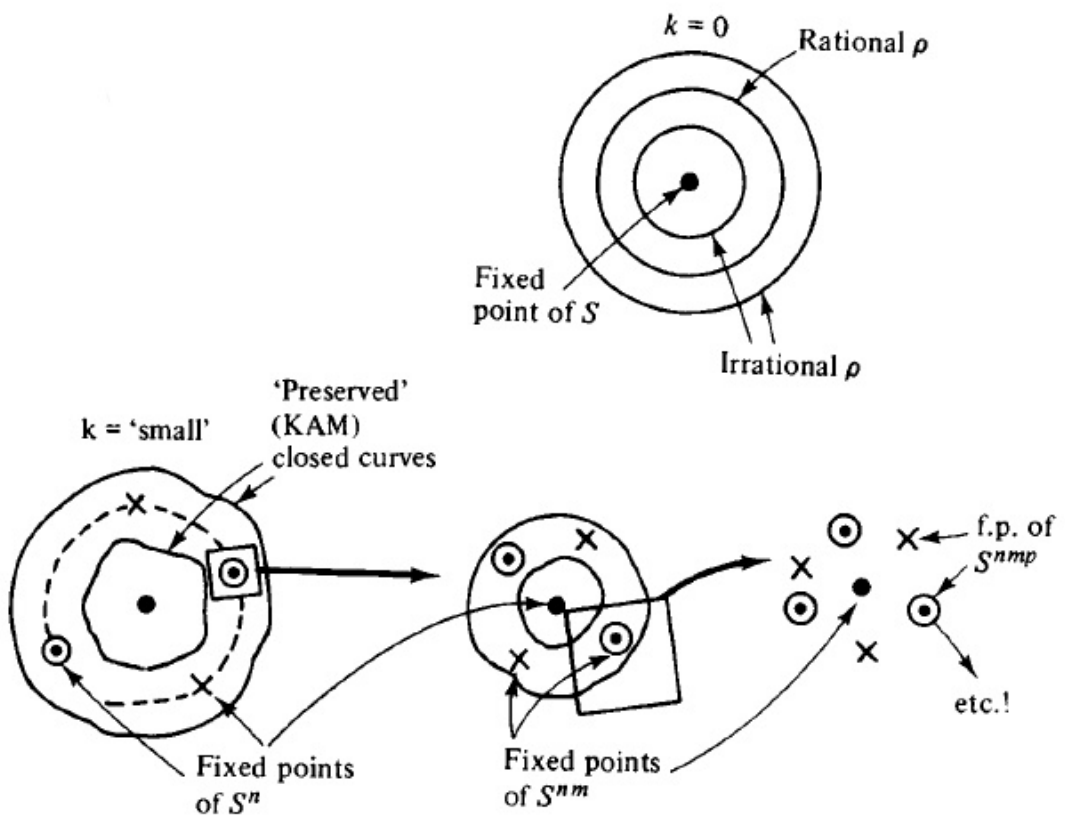
Figure 3.8: Illustration of the elliptic fixed points in higher orders (from [13]).

perturbation theory as presented in chapter 2. In between non-destroyed surfaces, island chains are visible with smaller amplitude. By expanding the scale to one of the island chains, higher order chains are revealed, but with even smaller amplitude. As shown in [18], the amplitude and frequency depend on the rotation number α as given in Eq. 3.3, with $(1/\alpha)^{1/2}$. Hence, higher order islands are of negligible amplitude as evident in Fig. 3.9 (c) and (d).

As stated by the KAM theorem, for sufficient small perturbations, most of irrational tori are not destroyed and thus most of phase space is covered by invariant curves. As there is a exponential dependency of occupied space and amplitude for higher-order resonances, the KAM theorem is reinforced. By repeatingly expanding the region around a random point in phase space, the underlying structure becomes visible as shown in Fig. 3.9. If the chosen perturbation is small enough, the point lies with high probability on a smooth KAM surface. As less and less space is stochastic, the probability of lying on a KAM surface is even higher with increasing expansion.

The structure is self-similar and this property is used to study properties of mappings. Around every fixed point of any order, *cantori* exist formed by the broken KAM surfaces. As discussed in [18], Arnold diffusion is explained by the gaps in the cantori.

To better understand the behaviour of KAM surfaces under perturbation, a numerical experiment for the standard map was performed. Several initial conditions

$$
\begin{align}
I_{(0)} &= 0.97 - 0.02i, \tag{3.24a} \\
\theta_{(0)} &= 0.49, \tag{3.24b}
\end{align}
$$

with $i = (0,...55)$, were selected for different values of the stochasticity parameter K.

In the unperturbed system (Fig. 3.10 (a)), $K = 0.0$, each orbit with a constant value of I is replaced by a sequence of of discrete values of θ on that orbit. For rational values of I, a finite number of values of θ exist; whereas the map is ergodic if I is irrational. For $K = 0.0$, we see horizontal lines in I that cover all values for θ. The selected initial conditions are low order rationals, e.g. $p_0 = 0.25$ with a periodicity of 4.

If the perturbation is switched on as shown in Fig. 3.10 (b) , $K = 0.02$, some curves start to deform and form closed curves centered on the elliptic fixed point $(\theta,I) = (\pi,0)$ and $(\theta,I) = (-\pi,0)$. Those curves are contractible and represent oscillations around $\theta = \pi$. Enhancing K further, the first KAM surfaces are destroyed and break into islands. They are still separated by adjacent noncontractible orbits.

The breaking of the KAM surfaces continues when K is raised further, e.g. to $K = 0.75$. As shown in Fig. 3.10 (c), a local stochastic region arises. However, those disordered scattered points are confined locally between the separatrices of adjacent noncontractible orbits. Still, this is the first occurence of chaos.
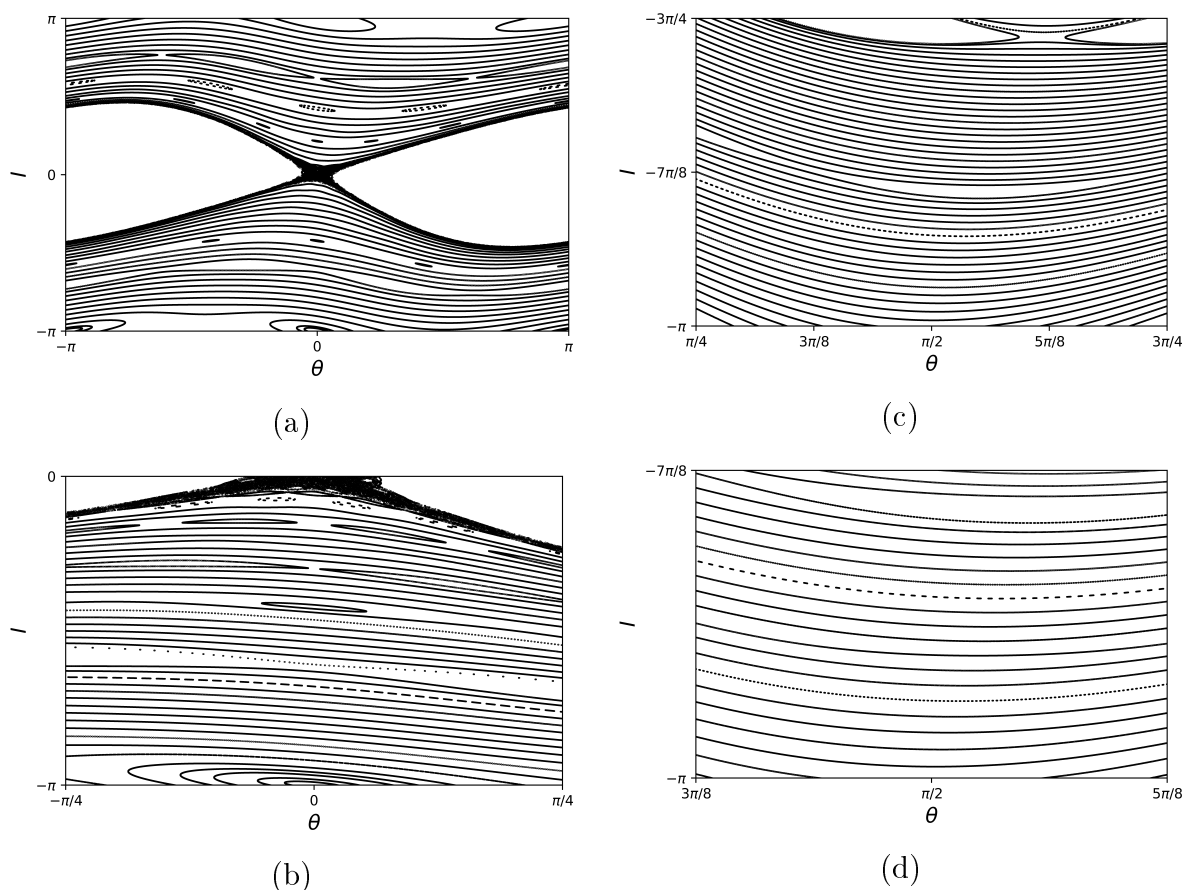
Figure 3.9: Standard map for $K = 0.5$ with magnification of the phase space. 1000 initial conditions for each map. The number of iterations increases from (a) to (d) with $n = 300, 1000, 5000, 10000$. (a) $\theta = [-\pi, \pi]$, $I = [-\pi, \pi]$, (b) $\theta = [-\pi/4, \pi/4]$, $I = [-\pi, 0]$, (c) $\theta = [\pi/4, 3\pi/4]$, $I = [-\pi, -3\pi/4]$, (d) $\theta = [3\pi/8, 5\pi/8]$, $I = [-\pi, -\pi/7]$.

For the critical value of $K = 0.9716$, as will be shown in chapter 4, the last KAM surface breaks and the motion is not confined in phase space anymore.

Increasing K further, the motion becomes more chaotic and leads finally to global stochasticity as shown in Fig. 3.10 (f).

The standard map is evaluated at $K = 0.9716$ to discuss the complexity in higher orders of the system. The initial conditions are presented in Fig. 3.11 (a) around one first order resonance. As K is exactly the critical value where the last KAM surface breaks, there are no solid lines visible anymore. Higher order chains are evolving around the first order fixed elliptic points. In Fig. 3.11 (b) the mapping near a second order elliptic fixed point is examined. Chains of third and higher orders are visible surrounding the fixed point. Magnifying further (Fig. 3.11 (c)), even higher orders are revealed and a

(a) $K = 0.0$

(b) $K = 0.02$

(c) $K = 0.75$

(d) $K = 0.9716$

(e) $K = 1.5$

(f) $K = 4.5$
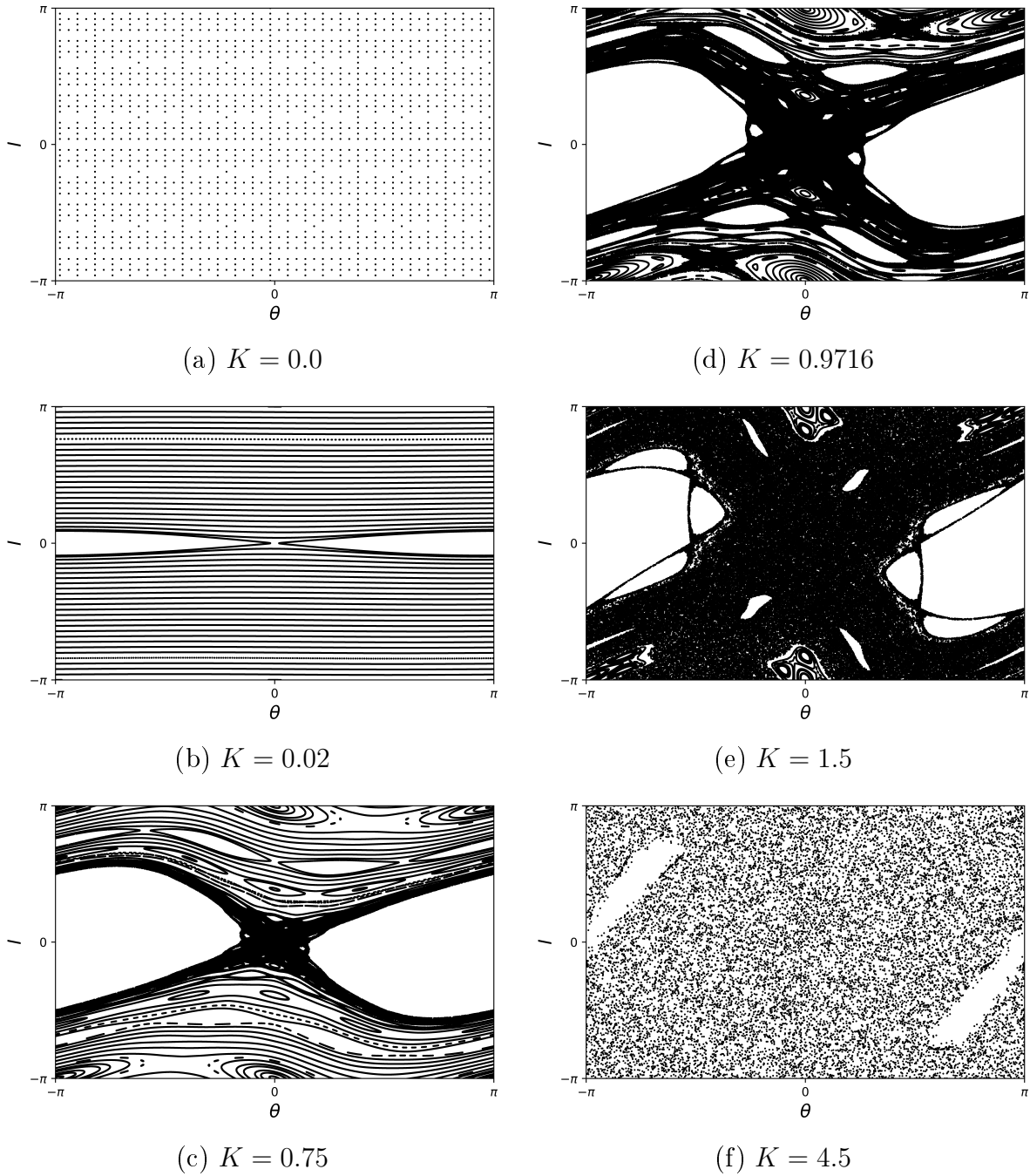
Figure 3.10: Standard map for different values of K. The map is iterated 2000 times for all figures. The initial points are chosen using Eq. 3.24b.
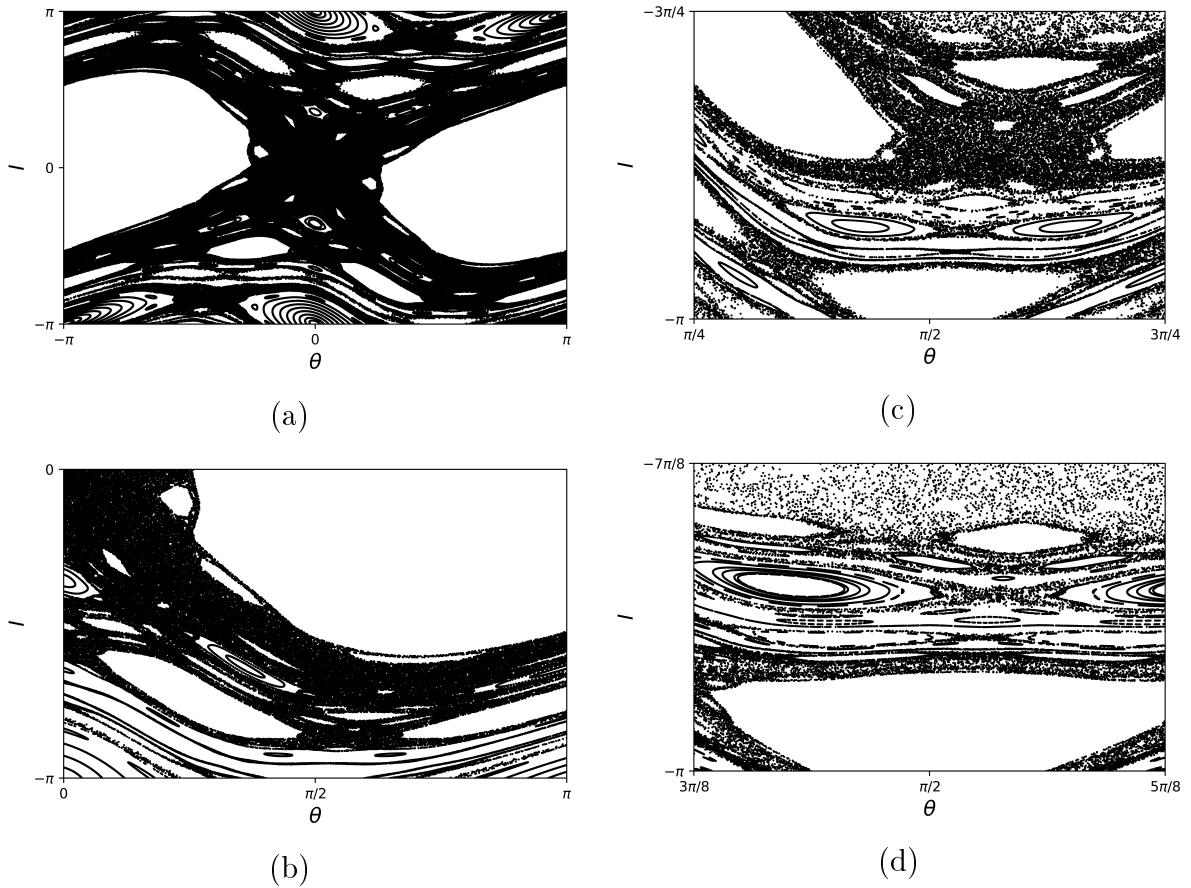
Figure 3.11: Standard map for $K = 0.9716$ with magnification of the phase space. 1000 initial conditions for each map. The number of iterations increases from (a) to (d) with $n = 300, 1000, 5000, 10000$. (a) $\theta = [-\pi, \pi]$, $I = [-\pi, \pi]$, (b) $\theta = [-\pi/4, \pi/4]$, $I = [-\pi, 0]$, (c) $\theta = [\pi/4, 3\pi/4]$, $I = [-\pi, -3\pi/4]$, (d) $\theta = [3\pi/8, 5\pi/8]$, $I = [-\pi, -\pi/7]$.

similar picture is produced by an even higher magnification (Fig. 3.11 (d)).

An evaluation for one single trajectory shows the missing restriction in phase space. In Fig. 3.12, the phase space for one trajectory for regular and stochastic motion for $n = 10^6$ steps is shown. If $K < K_{crit}$, the motion is bounded around the resonance and cannot pass to the adjacent resonance. Hence, the resonances do not overlap. However, the trajectory fills densely a region between two KAM surfaces and we conclude that there is local, confined instability of motion (*stochastic layer*). For $K > K_{crit}$, the particle wanders from one resonance to another and the variation in I becomes indefinitely large. However, there are still some regions of stability that the particle cannot enter, e.g. the central part of an integer resonance. Further smaller stable domains are visible even far inside the stochastic region. As studied by [4], there exist stability domains around the fixed points, even if $K \rightarrow \infty$. For sufficiently large values of K, the system becomes
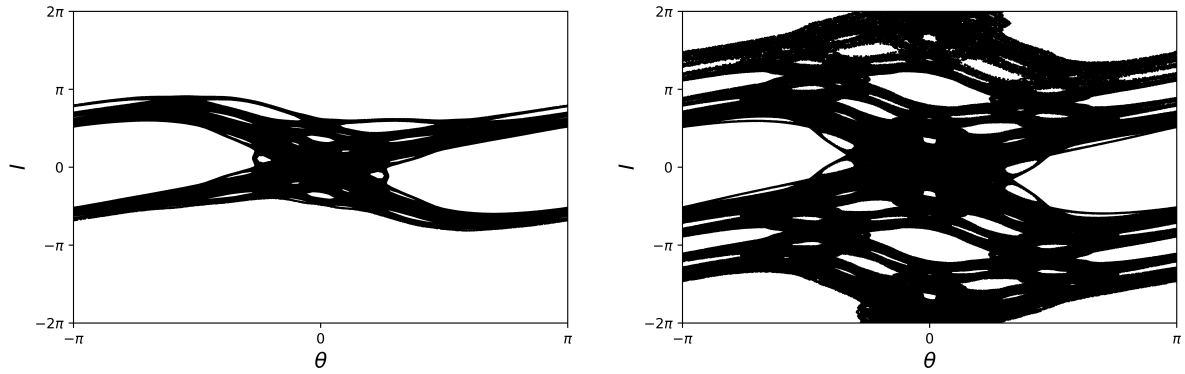
Figure 3.12: Standard map for one single trajectory. Left: $K = 0.96$, right: $K = 1.13$.

almost stochastic, with the exclusion of small but finite domains of regular motions. This is called a *divided phase space*, with regular and stochastic motion.

Chapter 4

Transition to chaos

In this chapter, two methods to determine the critical value of the stochasticity parameter K for the standard map are presented. In Ref. [4], a method to determine the transition to global stochasticity using the overlap of two resonances was proposed. This method is now known as the *overlap criterion*. The second method that is presented in this chapter examines linear stability of islands close to a KAM surface. As presented in [11], the correspondence of linear stability of high K numbers islands close to a KAM surface and its destruction was used to define a criterion for the transition to chaos.

4.1 Overlap criterion

To characterize the border of stability of the standard map, the *overlap criterion* was introduced in [4], as the separatrix width characterizes the motion near a resonance. If the domains of the resonances are situated sufficiently far from each other, the resonances can be treated separately as the perturbed region is small in phase space. We can expect that the motion of the system is locked within the domain of one of the resonances depending on the initial conditions. However, if the resonances are approaching each other, the motion might not be locked around one of the resonances but passes from one resonance to the other. This kind of motion is called *stochastic oscillations* as it becomes irregular. The *overlap criterion* states that as long as the separatrices of two neighbouring resonances do not touch each other, the motion is stable. In a rough first estimation, the separatix width of the first order resonances (period 1) is calculated from the unperturbed parameters, which is correct in order of magnitude. To increase the accuracy of the criterion, higher orders are included. Finally, also the thickness of the separatrix layer is included and a improved value of the critical stochasticity parameter $K = 1.2$ is found. This procedure is illustrated in Fig. 4.1.

4.1.1 First order

The maximum excursion of the pendulum at $\theta = 0$ with the separatrix energy ($\kappa = 1$) is given by,
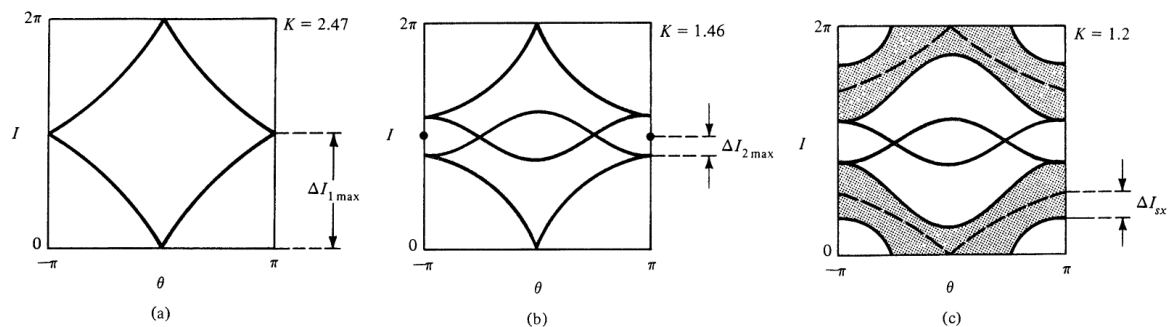
Figure 4.1: Overlap criterion: (a) First order. (b) First and second order. (c) Improved overlap criterion including the thickness of the separatrix layer (from [18]).

$$\Delta I_{max} = 2\sqrt{K}. \tag{4.1}$$

In the simplest approximation, the separatices of two adjacent resonances touch each other when the following equation is satisfied,

$$2\Delta I_{max} = \delta I, \tag{4.2}$$

where δI is the spacing between the resonances that is equal to 2π in the standard mapping. Hence, if,

$$K = \left(\frac{\pi}{2}\right)^2 = 2.47, \tag{4.3}$$

the separatrices touch and the motion might get stochastic.

4.1.2 Second order

In second order, the overlap criterion is defined as,

$$\Delta I_{1\mathrm{max}} + \Delta I_{2\mathrm{max}} = \delta I_{12} = \pi, \tag{4.4}$$

where the subindex (1,2) stands for period (1,2) resonances, respectively. $\Delta I_{1\mathrm{max}}$ is given by Eq. 4.1 and for $\Delta I_{2\mathrm{max}}$, the second harmonic Fourier component is needed, appearing in the second order of the expansion. For second order expansion, we use the Lie transformation method that is presented in Appendix A.

Using Eq. A.22, we can calculate the second order Fourier component of the Hamiltonian, starting from the perturbed Hamiltonian in the form $H = H_0 + \epsilon H_1$

$$H = \frac{I^2}{2} + \epsilon K \sum_m \cos(\theta - 2\pi m t), \tag{4.5}$$

where ϵ was introduced to order the perturbation, the Lie generating function w_1 is calculated using the first order Deprit equation,

$$\left(\frac{\partial}{\partial t} + J\frac{\partial}{\partial \theta}\right) w_1 = \bar{H}_1 - H_1. \tag{4.6}$$

We choose now $\bar{H}_1 = 0$, as $\langle H_1 \rangle = 0$, where $\langle\rangle$ denotes the average over zeroth order orbits, and get for w_1,

$$w_1 = K \sum_m \frac{\sin(\theta - 2\pi m t)}{2\pi m - I}. \tag{4.7}$$

Using the second order Deprit equation,

$$\left(\frac{\partial}{\partial t} + I\frac{\partial}{\partial \theta}\right) w_2 = 2(\bar{H}_2 - H_2) - [w_1, \bar{H}_1 + H_1], \tag{4.8}$$

where H_2 and $\bar{H}_1$ are zero, the transformed Hamiltonian in second order is chosen to eliminate the average of the right hand side,

$$\bar{H}_2 = \frac{1}{2}\langle [w_1, H_1] \rangle = -\frac{1}{2}\left\langle \frac{\partial w_1}{\partial I}\frac{\partial H_1}{\partial \theta} \right\rangle. \tag{4.9}$$

We assume that the second order resonances lie in the middle between primary resonances for I,

$$I = (2p+1)\pi, \tag{4.10}$$

where p is an integer. Using Eq. 4.9 and the series expansions for w_1 and H_1, we arrive at[1]

$$\bar{H}_2 = -\frac{K^2}{4} \sum_m \frac{\cos(2\theta - 2\pi(2p+1)t)}{(2\pi)^2(m - p - \frac{1}{2})^2}. \tag{4.13}$$

---

[1] $\bar{H}_2 = \frac{K^2}{4}\left\langle \sum_m \frac{\sin(\theta - 2\pi m t)}{2\pi m - I)^2} \sum_m' \sin(\theta - 2\pi m' t) \right\rangle = \frac{K^2}{4}\left\langle \sum_{m,m'} \frac{\cos(2\pi(m'-m)t) - \cos(2\theta - 2\pi(m'+m)t)}{(2\pi m - I)^2} \right\rangle$.

We average over $\theta = It$, the zero-th order orbit. The first term vanishes unless $m = m'$, leading only to a constant term that will be ignored, whereas the second term vanishes unless

$$2I - 2\pi(m' + m) = (m + m') - (2p+1) = 0. \tag{4.11}$$

Hence we get

As $\sum_m 1/(m - p - \frac{1}{2})^2 = \pi^2$, we get for the transformed Hamiltonian $\bar{H}$ up to second order (with $\bar{H}_1 = 0$),

$$\bar{H} = \frac{I^2}{2} - \left(\frac{K^2}{16}\right)\cos(2\hat{\theta}), \tag{4.14}$$

where $\hat{\theta} = \theta - \pi(2p + 1)t$.

Therefore, the maximum excursion reads as

$$\Delta I_{2\text{max}} = \frac{K}{2}. \tag{4.15}$$

The overlap criterion in second order becomes,

$$2\sqrt{K} + \frac{K}{2} = \pi, \tag{4.16}$$

resulting in $K = 1.46$. This value is a very rough estimate of K. As adding higher orders does not improve the value found for K as shown in [5], the width of the stochastic layer near the separatrix is included.

4.1.3 Separatrix width

To describe the motion in the vincinity of the separatrix, in [5] a separatrix mapping was developed,

$$w_{n+1} = w_n - w_0\sin(\phi_n), \tag{4.17a}$$

$$\phi_{n+1} = \phi_n + Q_0\ln|\frac{32}{w_{n+q}}|, \tag{4.17b}$$

where $w = \frac{\Delta H}{K}$ is the deviation of energy from the separatrix energy K and ϕ is the phase of the driving term and $Q_0 = \frac{2\pi}{\sqrt{K}}$, the ratio of the driving frequency to the primary island frequency at the elliptic fixed point.

To obtain the half-width of the primary stochastic layer, we linearize w to bring Eq. 4.17 in the form of a standard mapping. For K, we obtain

$$\bar{H}_2 = -\frac{K^2}{4}\sum_m \frac{\cos(2\theta - 2\pi(2p + 1)t)}{(2\pi)^2(m - p - \frac{1}{2})^2}. \tag{4.12}$$

$$K = \frac{8\pi Q_0^3}{w_1} \exp\left(\frac{-\pi Q_0}{2}\right), \tag{4.18}$$

and therefore

$$w_1 = \frac{4(2\pi)^2}{K^{5/2}} \exp\left(\frac{-\pi^2}{K^{1/2}}\right). \tag{4.19}$$

If the phase is $\theta = \pi$ at the elliptic fixed point and the energy $K + \Delta H = K(1 + w_1)$, we get for the action, assuming $w \ll 1$,

$$I = 2\sqrt{K}\left(1 + \frac{w_1}{4}\right). \tag{4.20}$$

Therefore, for the width of the separatrix ΔI_{sx}, we get

$$\Delta I_{sx} = I - I_0 = \frac{1}{2} w_1 \sqrt{K}, \tag{4.21}$$

as $I_0 = 2\sqrt{K}$.

The overlap criterion including second order and the separatrix width is then

$$2\sqrt{K}\left(1 + \frac{w_1}{4}\right) + \frac{K}{2} = \pi, \tag{4.22}$$

and the obtained value is $K = 1.2$.

4.2 Greene's method

The second method to estimate the transition to chaos is based on the correspondence between the destruction of a irrational KAM surface and the destabilization of elliptic fixed points of the high-harmonic rational iterates, that approach the irrational winding number α of that KAM surface [11] as illustrated in Fig. 4.2.

Greene proposed to consider a sequence of periodic orbits $\alpha_N = R_N/S_N$, that converge for $N \to \infty$ to the irrational rotation number α of the KAM curve of interest,

$$\lim_{N\to\infty} \alpha_N = \lim_{N\to\infty} \frac{R_N}{S_N} = \alpha. \tag{4.23}$$

As shown in [16], the best way to approximate irrationals by rationals is by using the unique continued fraction representation
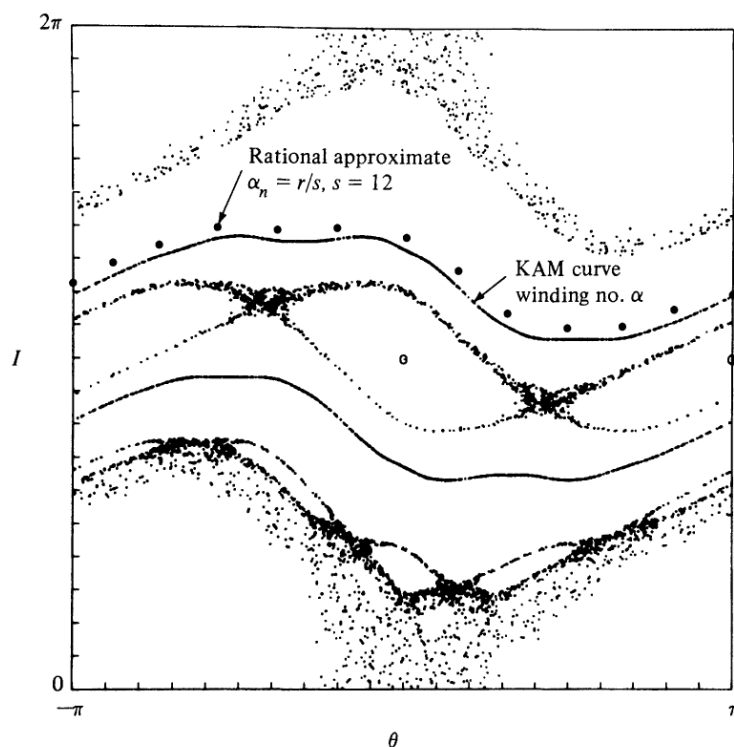
Figure 4.2: Five orbits for the standard mapping at $K = 0.97$ illustrating the basic correspondence in Greene's method: the destabilization of elliptic fixed points of rational approximates correspond to the destruction of the approximated KAM surface (from [18]).

$$\alpha = a_0 + \cfrac{1}{a_1 + \cfrac{1}{a_2 + \cfrac{1}{a_3 + \ldots}}} \equiv [a_0, a_1, a_2, a_3, \ldots], \qquad (4.24)$$

where a_n are positive integers. This expansion is the best approximation for α as no other r/s is closer to α for $s \leq S_n$.

To determine the last KAM surface that is destroyed, we expect that it is the number that is least easily approximable by rationals. The group of irrationals that is the most difficult to approximate is the one with the fraction form of $[a_0, a_1, \ldots, a_m, 1, 1, 1 \ldots]$, with $a_k = 1$ for $k > m$. Hence, the irrational number least easily approximated by rationals is the golden mean,

$$\alpha^* = [1, 1, 1, \ldots] = \frac{\sqrt{5} + 1}{2}. \qquad (4.25)$$

For this KAM surface the conditions for KAM theory are most easily satisfied as the

problem with small denominators in perturbation theory is minimal. It was verified by numerical simulations, that indeed the last KAM surface to be destroyed is the one with the winding number equal to the golden mean [11]. This is only true for the standard mapping.

Greene investigated the stability of periodic orbits with rotation numbers equal to the convergent fraction approximates. Orbits in the vincinity of fixed points can be approximated by the linearization in tangent space [10]. The tangent space orbit $n(\delta J_n, \delta \theta_0)$ is calculated by

$$\begin{pmatrix} \delta J_n \\ \delta \theta_n \end{pmatrix} = \mathcal{J} \begin{pmatrix} \delta J_0 \\ \delta \theta_0 \end{pmatrix}, \tag{4.26}$$

where $(\delta J_0, \delta \theta_0)$ is the orbit of the initial conditions at the point (J_0, θ_0). $\mathcal{J}$ denotes the product of s Jacobian matrices and results in,

$$\mathcal{J} = \prod_{n=1}^{s} \begin{pmatrix} 1 & K\cos(\theta_n) \\ 1 & 1 + K\cos(\theta_n) \end{pmatrix}, \tag{4.27}$$

where θ is the phase shift per period. Rational surfaces are either of the hyperbolic or the elliptic type, depending on the residue of the fixed point in the tangent mapping, that characterizes the displacement of a point along an invariant curve [10],

$$R = \frac{1}{4}(1 - tr(\mathcal{J})). \tag{4.28}$$

For elliptic fixed points, the trace simplifies to,

$$tr(\mathcal{J}) = 2\cos\theta, \tag{4.29}$$

thus, Eq. 4.27 becomes,

$$R = \sin^2\left(\frac{\theta}{2}\right). \tag{4.30}$$

Thus, to have stable motion around an elliptic point, we require that $0 < R < 1$. If this condition is satisfied, tangent space orbits stay on elliptic orbits in the vincinity of the elliptic fixed point. However, R is increasing with K and former stable orbits become unstable.

The dependence of R on K can be estimated by using a different representation of R, following a procedure of Bountis and Helleman ([10]),

$$R = -\frac{1}{4}\det \begin{pmatrix} 2 - K\cos\theta_1 & -1 & ... & -1 \\ -1 & 2 - K\cos\theta_2 & & \\ 0 & & & \\ ... & & & \\ -1 & & & 2 - K\cos\theta_s \end{pmatrix}. \qquad (4.31)$$

If K is large, we assume from Eq. 4.31 that $R \propto K^s$. Greene showed that this is true also for small K and postulated that it is true for all K [10]. The residue increases exponentially with the orbit length, and this is proportional to s. Hence it is practical to observe the *mean residue*,

$$f = \left(\frac{|R|}{\beta}\right)^{1/s}, \qquad (4.32)$$

where β is a constant for rapid convergence.

Greene observed that if $K < K_{cr}$, $R \to 0$ and the KAM curve is preserved. Whereas for $K > K_{cr}$, $R \to \infty$ and the curve is destroyed. At the critical value of K, R remains bounded and the KAM curve still exists but appears to be non-smooth. Hence, the value of K that destroys a KAM curve depends on the rotation number α.

For the KAM curve with the rotation number equal to the golden mean, Greene found the critical value to be [11]

$$K_{cr} = 0.971635... \qquad (4.33)$$

Both methods, the overlap criterion and Greene's method, estimate the critical value of $K \approx 1$ for the standard map. The overlap criterion is a more heuristic approach that serves as a rough estimation of the transition to stochasticity, whereas Greene's method examines the destruction of KAM surfaces. The lower value of K resulting from the second method becomes clear when we consider that the last KAM surface breaks up well before islands overlap due to the interaction of slowly varying terms outside of the two separatrices. Moreover, Greene's method is only true for the standard map as discussed in [18]. For general systems where two resonances are interacting with arbitrary separation and amplitudes, a renormalization procedure was introduced to estimate the amplitudes of two neighbouring island chains that are required to destroy the last KAM surface between their stochastic separatrix layers. It was found that for only two resonances, the critical value of K is larger than for the standard map that has an infinite number of resonances.

Chapter 5

Models to describe resonances and mappings

In this chapter, different models are described and converted into the standard map. Starting with the free particle in one dimension with a time dependent perturbation, the system is first extended to a one-dimensional pendulum with a time dependent perturbation and then to a one-dimensional pendulum with free motion in the second dimension. Those systems are mathematically equivalent. Secular perturbation theory presented in chapter 2 is used to transform the actions and angles to resonant action-angle variables. The resulting Hamiltonian allows an analysis of the motion in the vicinity of the resonance. Using the equations of motion, the standard map can be calculated and compared to the exact equations of motion. Via this comparison, the stochasticity parameter K is calculated and is an indication for arising chaos depending on the perturbation strength.

5.1 Standard map

For all models, the Hamiltonian is expanded around the resonance, leading to the *standard Hamiltonian*, given in Eq. 2.35:

$$\Delta \bar{H}(\bar{\theta}, \Delta \bar{J}) = \frac{1}{2}\bar{\Omega}'\Delta \bar{J}^2 + |H_{\boldsymbol{m}}(\bar{J})|(1 - \cos\bar{\theta}). \tag{5.1}$$

The equations of motion are derived from the Hamiltonian and read:

$$\dot{\bar{\theta}} = \bar{\Omega}'\tau_b \Delta \bar{J}, \tag{5.2a}$$

$$\Delta \dot{\bar{J}} = -|H_{\boldsymbol{m}}|\tau_b \sin\bar{\theta}. \tag{5.2b}$$

The corresponding mapping can be constructed by using the equations of motion and approximating time derivatives by forward-backward finite differences,

$$\bar{\theta}(t + \Delta t) \approx \bar{\theta}(t) + \dot{\bar{\theta}}(t)\Delta t, \tag{5.3a}$$

$$\Delta \bar{J}(t + \Delta t) \approx \bar{J}(t) + \dot{\bar{J}}(t)\Delta t. \tag{5.3b}$$

The mapping becomes

$$\bar{\theta}_{(n+1)} = \bar{\theta}_{(n)} + \tau_b \bar{\Omega}' \Delta \bar{J}_{(n)}, \tag{5.4a}$$

$$\Delta \bar{J}_{(n+1)} = \Delta \bar{J}_{(n)} - \tau_b |H_{\boldsymbol{m}}| \sin \bar{\theta}_{(n+1)}. \tag{5.4b}$$

To compare it to the *standard map*, we introduce $\Delta \bar{I} = \tau_b \bar{\Omega}' \Delta \bar{J}$. The mapping becomes

$$\bar{\theta}_{(n+1)} = \bar{\theta}_{(n)} + \Delta \bar{I}_{(n)}, \tag{5.5a}$$

$$\Delta \bar{I}_{(n+1)} = \Delta \bar{I}_{(n)} - K \sin \bar{\theta}_{(n+1)}, \tag{5.5b}$$

with the stochasticity parameter

$$K = \tau_b^2 |H_{\boldsymbol{m}}| \bar{\Omega}'. \tag{5.6}$$

This is valid for an arbitrary system with an arbitrary number of degrees of freedom.

5.2 Free particle motion in one dimension, time-dependent

The unperturbed Hamiltonian for a free one-dimensional particle is

$$H_0(p) = \frac{p^2}{2m}, \tag{5.7}$$

implying the equations of motion:

$$\dot{p} = 0, \tag{5.8}$$

$$\dot{x} = v = \frac{p}{m}. \tag{5.9}$$

The bounce (transit) time τ_b corresponding to the bounce frequency ω_b is calculated using Eq. 1.41:

$$\tau_b = \pi \sqrt{\frac{2m}{H}} = \frac{2\pi m}{p}. \tag{5.10}$$

The action-angle variables become

$$J = \frac{1}{2\pi} \int_0^{2\pi} p(H) dx = \frac{1}{2\pi} \int_0^{2\pi} \sqrt{2mH} dx = p, \tag{5.11}$$

$$\theta = 2\pi \frac{\tau}{\tau_b} = \sigma x, \tag{5.12}$$

where $\sigma = \pm 1$ distinguishes co-passing from counter-passing orbits. The canonical frequency is given by

$$\Omega = \frac{dH}{dJ} = \frac{2\pi}{\tau_b} = \frac{p}{m} = \frac{J}{m}. \tag{5.13}$$

The equations of motion in action-angle variables are

$$\dot{J} = 0, \tag{5.14}$$

$$\dot{\theta} = \Omega = \frac{p}{m}. \tag{5.15}$$

A time-dependent perturbation H_1 in θ is introduced:

$$H_1 = H_l \cos(l\theta - \omega t). \tag{5.16}$$

Hence, the equations of motion in the perturbed system are

$$\dot{J} = -l H_l \sin(l\theta - \omega t), \tag{5.17}$$

$$\dot{\theta} = \Omega = \frac{J}{m}. \tag{5.18}$$

The resonant action and angle are calculated using Eq. 2.22:

$$\bar{J} = \frac{J}{l}, \tag{5.19}$$

$$\bar{\theta} = l\theta - \omega t + \bar{\theta}_0. \tag{5.20}$$

For the conversion to the standard map, $\Delta\bar{J}$ is defined as

$$\Delta\bar{J} = \bar{J} - \bar{J}_{\text{res}}, \tag{5.21}$$

with $\bar{J}_{\text{res}} = \sqrt{2mE_{\text{res}}}$.

The resonance condition is given by

$$\bar{\Omega} = l\Omega - \omega = \frac{lp}{m} - \omega, \tag{5.22}$$

and its derivative by

$$\bar{\Omega}' = \frac{l^2}{m}. \tag{5.23}$$

5.3 One-dimensional pendulum

Let us now extend the system of the free particle to an one-dimensional pendulum,

$$H_0(x,p) = \frac{p^2}{2m} + U_0(1 - \cos(x)). \tag{5.24}$$

The system is transformed to action-angle variables as explained in chapter 1.2.

A perturbation is introduced, in terms of harmonics in canonical angle θ, action J, time t and a perturbation frequency ω:

$$H_1(\theta,J,t) = \sum_l \bar{H}_l(J)e^{i(l\Omega - \omega t)}. \tag{5.25}$$

Again, the action and angle are transformed to the resonant set of variables equivalent for the free particle in Eq. 5.19 and 5.20,

$$\bar{J} = \frac{J}{n}, \tag{5.26}$$

$$\bar{\theta} = n\theta - \omega t + \bar{\theta}_0. \tag{5.27}$$

For the conversion to the standard map, $\Delta\bar{J}$ is defined as

$$\Delta \bar{J} = \bar{J} - \bar{J}_{\mathrm{res}}, \tag{5.28}$$

with $\bar{J}_{\mathrm{res}}(E_{\mathrm{res}})$ as defined for trapped and passing particles in Eq. 1.42 and 1.46, respectively.

To investigate the resonances, the resonance condition has to be satisfied:

$$\bar{\Omega} = l \cdot \Omega - \omega = 0, \tag{5.29}$$

with Ω as defined in Eq. 1.45 and Eq. 1.48 for trapped and passing particles respectively. Its derivative is given by

$$\bar{\Omega}_t' = n^2 \frac{\pi^2}{16m} \frac{(\kappa - 1)\mathcal{K}(\kappa) + \mathcal{E}(\kappa)}{(\kappa - 1)\kappa \mathcal{K}^3}, \tag{5.30}$$

$$\bar{\Omega}_p' = n^2 \frac{\kappa \pi^2 \mathcal{E}(\kappa)}{4m(\kappa - 1)\mathcal{K}(\kappa)^3}, \tag{5.31}$$

for trapped and passing particles respectively, with $\kappa = H/(2U_0)$.

5.4 Pendulum with two degrees of freedom

The finally considered system is the one-dimensional pendulum extended with a second dimension of free motion,

$$H(x, p_x, p_y) = \frac{p_x^2}{2m} + \frac{p_y^2}{2m} + U_0(1 - \cos x), \tag{5.32}$$

with the following equations of motion

$$\dot{x} = \frac{p_x}{m}, \tag{5.33}$$

$$\dot{y} = \frac{p_y}{m}, \tag{5.34}$$

$$\dot{p}_x = -U_0 \sin x, \tag{5.35}$$

$$\dot{p}_y = 0. \tag{5.36}$$

Using Eq. 1.31, action-angle variables can be calculated,

$$J_x = \sqrt{mU_0}\frac{8}{\pi}(\mathcal{E}(\kappa_x) - (1 - \kappa_x)\mathcal{K}(\kappa_x)), \tag{5.37}$$

$$J_y = p_y, \tag{5.38}$$

$$\theta^x = \frac{\pi\mathcal{F}(\frac{x}{2}, \kappa_x)}{2\mathcal{K}(\kappa_x)}, \tag{5.39}$$

$$\theta^y = y, \tag{5.40}$$

where $\kappa_x = (H - p_y^2/(2m))/(2U_0)$. We find for the canonical frequencies

$$\Omega^x = \frac{U_0}{m}\frac{\pi}{2\mathcal{K}(\kappa_x)}, \tag{5.41}$$

$$\Omega^y = \frac{2\pi}{\Delta y}\langle v^y \rangle_b = \langle \frac{p_y}{m} \rangle_b = \frac{p_y}{m}, \tag{5.42}$$

where $\langle \rangle_b$ denotes the bounce average defined as

$$\langle b(\tau) \rangle_b = \frac{1}{\tau_b}\int_0^{\tau_b} d\tau b(\tau). \tag{5.43}$$

The perturbation is chosen to be of the form

$$H_1 = \sum_{\boldsymbol{m}} H_{\boldsymbol{m}}e^{i(l\theta^x + n\theta^y)}, \tag{5.44}$$

from which follows the resonance condition:

$$\bar{\Omega} = l\Omega^x + n\Omega^y = 0. \tag{5.45}$$

We choose J_y as the resonant action and define the resonant actions and angles as following:

$$\bar{J}_x = J_x - \frac{l}{n}J_y, \tag{5.46}$$

$$\bar{J} = \bar{J}_y = \frac{J_y}{n}, \tag{5.47}$$

$$\bar{\theta}^x = \theta^x = \frac{\pi\mathcal{F}(\frac{x}{2}, \kappa_x)}{2\mathcal{K}(\kappa_x)}, \tag{5.48}$$

$$\bar{\theta} = \bar{\theta}^y = l\theta^x + n\theta^y + \bar{\theta}^0 = l\theta^x + ny + \bar{\theta}^0. \tag{5.49}$$

For the conversion to the standard map, $\Delta \bar{J}$ is defined as

$$\Delta \bar{J} = \bar{J} - \bar{J}_{\mathrm{res},y}, \tag{5.50}$$

with $\bar{J}_{\mathrm{res},y}(E_{\mathrm{res}}) = p_{y0}/l$.

Using Eq. 2.36, we calculate an explicit representation of $\bar{\Omega}'$:

$$\begin{aligned}
\bar{\Omega}' &= \frac{\partial \bar{\Omega}}{\partial \bar{J}} = \frac{\partial \bar{\Omega}}{\partial J_x}\frac{\partial J_x}{\partial \bar{J}} + \frac{\partial \bar{\Omega}}{\partial J_y}\frac{\partial J_y}{\partial \bar{J}} \tag{5.51}\\
&= l\frac{\partial \bar{\Omega}}{\partial J_x} + n\frac{\partial \bar{\Omega}}{\partial J_y} \tag{5.52}\\
&= l\frac{\partial (l\Omega^x + n\Omega^y)}{\partial J_x} + n\frac{\partial (l\Omega^x + n\Omega^y)}{\partial J_y} \tag{5.53}\\
&= l^2\frac{\partial \Omega^x}{\partial J_x} + \frac{n^2}{m} \tag{5.54}\\
&= l^2\frac{\partial \Omega^x}{\partial \kappa_x}\frac{\kappa_x(J_x,J_y)}{\partial J_x} + \frac{n^2}{m} \tag{5.55}\\
&= l^2\frac{\partial \Omega^x}{\partial \kappa_x}\left(\frac{dJ_x}{d\kappa_x}\right)^{-1} + \frac{n^2}{m}. \tag{5.56}
\end{aligned}$$

Chapter 6

Numerical analysis of the models

In this chapter, the previously presented models are examined numerically. Different initial conditions and perturbations are examined to discuss the resulting value of the stochasticity parameter K.

Also, the obtained numerical results for the $(\Delta \bar{J}, \bar{\theta})$ phase space around a specific are compared to the standard map and its applicability for the presented models is discussed.

6.1 Free particle motion in one dimension

A time-harmonic perturbation is introduced with

$$H_1 = |H_k|\cos(kx - \omega t), \tag{6.1}$$

where $k = 1$ and the perturbation frequency $\omega = 2.0\omega_0$. The initial conditions are chosen in an interval of $[0.5E_{\text{res}}, 1.5E_{\text{res}}]$ around the resonance energy of $E_{\text{res}} = 2.0$, where the resonance condition $l\Omega - \omega = 0$ is satisfied, with $l = 1$. To illustrate the development of stochastic regions in phase space, $|H_k|$ was chosen in a range of $[0.01, 0.15]$ and the stochasticity parameter K was calculated using Eq. 5.6.

As shown in Fig. 6.1, the standard map describes the motion near the resonance and is in accordance to the numerical results for the $(\Delta \bar{J}, \bar{\theta})$ phase space given in Eq. 5.21 and 5.20. As predicted by theory, there are supertrapped particles around the resonance with initial conditions of $E \approx E_{\text{res}} \pm 0.2$. Particles with less or more energy are not trapped around the resonance and are therefore superpassing particles. The width of the resonance given in Eq. 2.38 is in accordance with the numerical experiments shown in Fig. 6.1.

The twist of the standard map compared to the numerical results arises as the standard map describes a system with a perturbation with $\delta(t - \tau_b)$, whereas the analytical system is perturbed with harmonics in t. Moreover, the standard map describes a infinite set

of equidistant resonances, whereas here, only several resonances are interacting with arbitrary distance and amplitude.

For a perturbation of $|H_k| = 0.15$, the stochasticity parameter K exceeds the critical value of $K \approx 1$ and stochastic motion occurs as it becomes evident in Fig. 6.1 (c). Now, resonances overlap and this implies that a particle can cross one resonance after another and is not confined in phase space anymore as all KAM surfaces have broken.

Fig. 6.2 compares the numerical results for the $(\Delta \bar{J}, \bar{\theta})$ phase space and the standard map for the critical value of $K = 0.9716$. Here, the used time-harmonic perturbation also includes higher order resonances of the form:

$$H_1 = |H_k|\cos(kx - \omega t) + |H_k|\cos(kx - 2\omega t) + |H_k|\cos(kx - 3\omega t), \qquad (6.2)$$

with $k = 1$ and $\omega = 2.0\omega_0$. The resulting plot is similar to Fig. 3.11: higher order chains are evolving around the fixed elliptic points as discussed in chapter 3.

6.2 Pendulum in one dimension

For the one-dimensional pendulum, a time-harmonic perturbation is introduced with

$$H_1 = |H_k|\cos(kx - \omega t), \qquad (6.3)$$

where $k = 1$ and the perturbation frequency $\omega = 1.5\omega_0$. As discussed in [1], every mode in coordinate space results in several modes in $\boldsymbol{m} \cdot \boldsymbol{\theta}$, where the amplitude decreases with larger m as shown in Fig. 6.3. The initial conditions are chosen in an interval of $[0.95E_{res}, 1.05E_{res}]$ around the resonance energy of E_{res}, shown in Fig. 6.3, where the resonance condition $l\Omega - \omega = 0$ is satisfied.

As trapped and passing particles have to be distinguished as two distinct kinds of motion, there exist two resonances for every mode l in θ, one passing and one trapped respectively as shown in Fig. 6.3. For both kinds, the standard mapping and the analytical calculation have been performed to calculate the resulting stochasticity parameter. For the used perturbation frequency ω, trapped modes only arise for $l > 1$.

As shown in Fig. 6.6, the standard map is in accordance to the numerical results for the $(\Delta \bar{J}, \bar{\theta})$ phase space given in Eq. 5.28 and 5.27. Resonances with $l > 2$ are very close to the separatrix of the unperturbed system and change the type of motion by crossing the separatrix causing high values of K and therefore stochasticity. This also explains the difference for the numerical results for the $(\Delta \bar{J}, \bar{\theta})$ phase space and the standard map, as the latter is not sensitive about the separatrix.
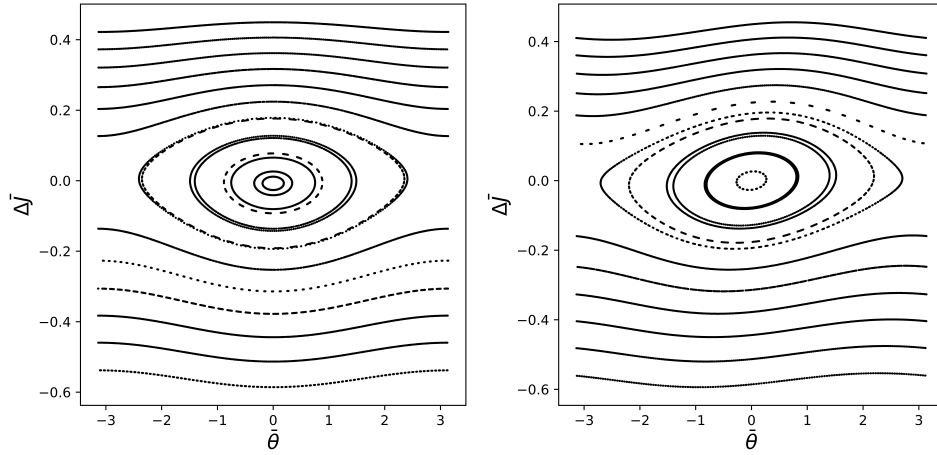
(a) $|H_k|/U_0 = 0.01$, $K = 0.098$.
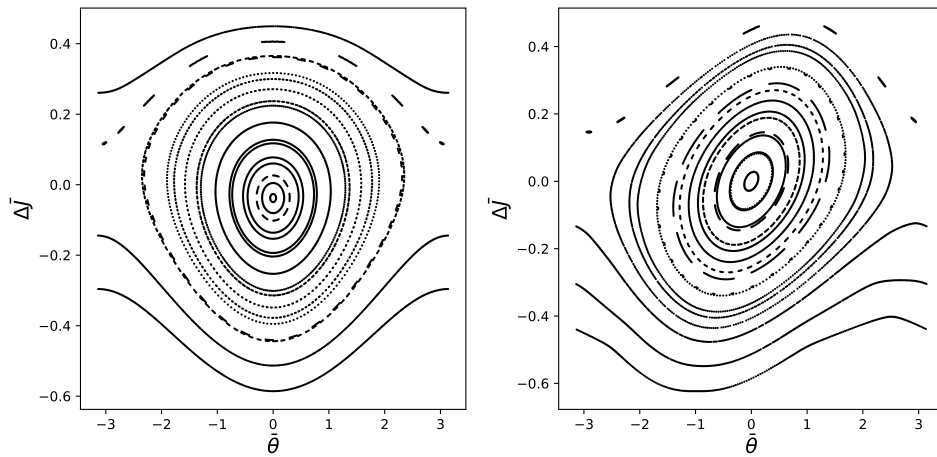
(b) $|H_k|/U_0 = 0.05$, $K = 0.493$.
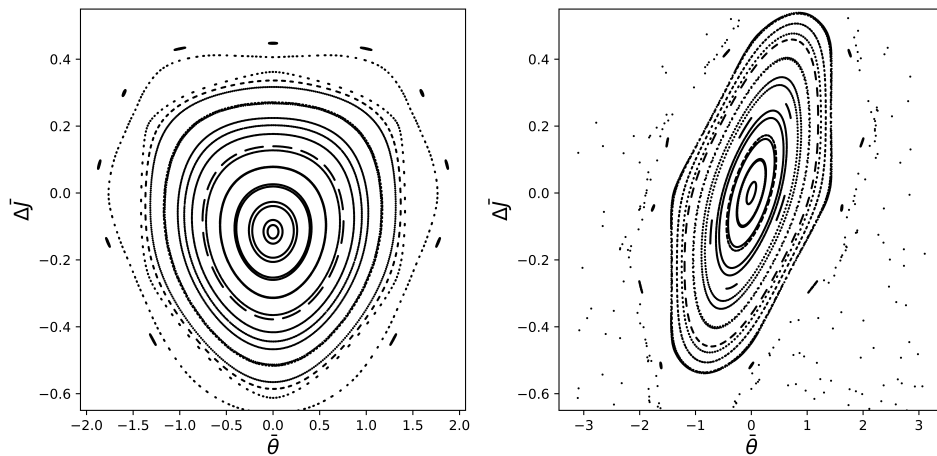
(c) $|H_k|/U_0 = 0.15$, $K = 1.480$.

Figure 6.1: Free particle: Comparison of the numerical results for $\Delta\bar{J},\bar{\theta}$ (left) and the standard map (right) for different values of $|H_k|/U_0$. 20 initial conditions and $N = 500$ iterations for each map were used.
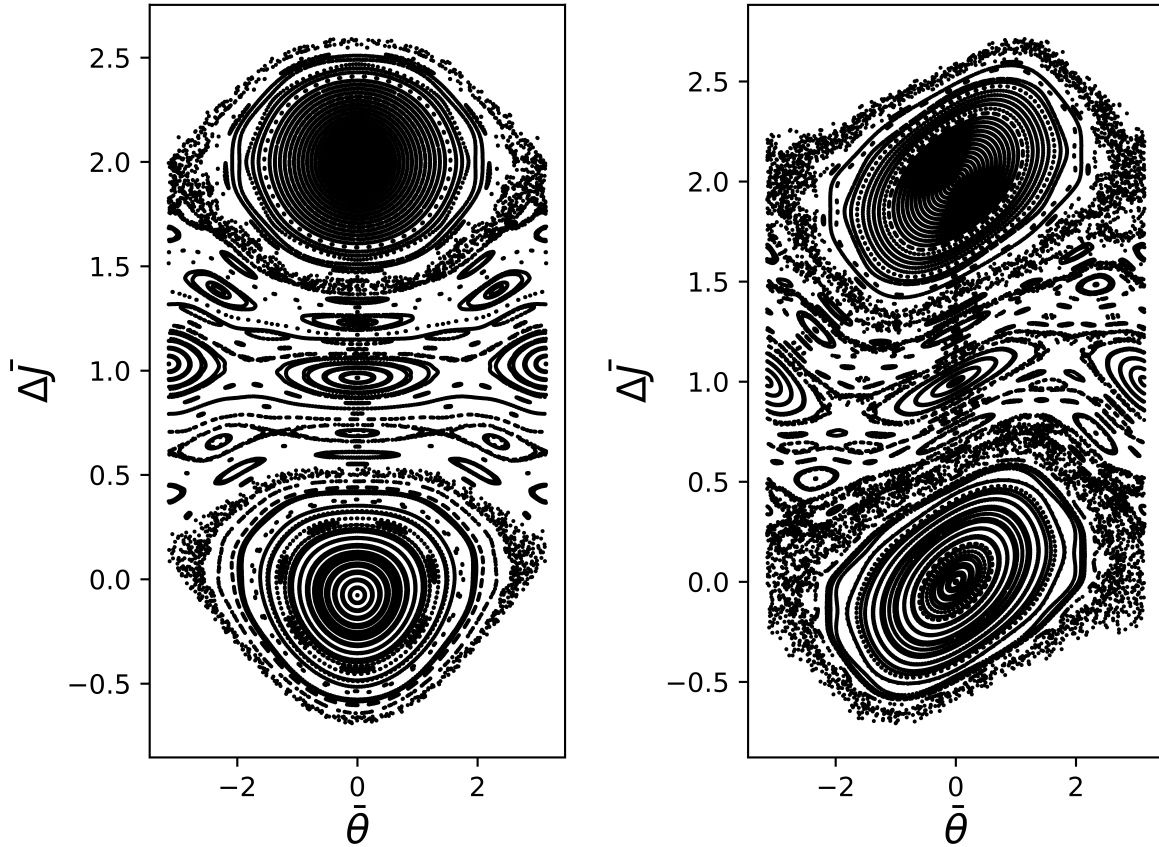
Figure 6.2: Free particle: Comparison of the numerical results for $\Delta\bar{J},\bar{\theta}$ (left) and the standard map (right) for $|H_k|/U_0 = 0.1$. The stochasticity parameter is $K = 0.98$.

6.3 Pendulum with two degrees of freedom

For the pendulum with two degrees of freedom, a harmonic perturbation was introduced with

$$H_1 = |H_k|\cos(kx - ny), \tag{6.4}$$

with $k = 1$ and $n = 3$. As for the one-dimensional pendulum, every mode in coordinate space results in several modes in $\boldsymbol{m} \cdot \boldsymbol{\theta}$ with decreasing amplitude. For this model, initial conditions are chosen in an interval of $p_y = [-4,4]$ and the resonance energy was calculated using the resonance condition

$$l\Omega^x + n\Omega^y = l\Omega^x + n\frac{p_y}{m} = 0. \tag{6.5}$$
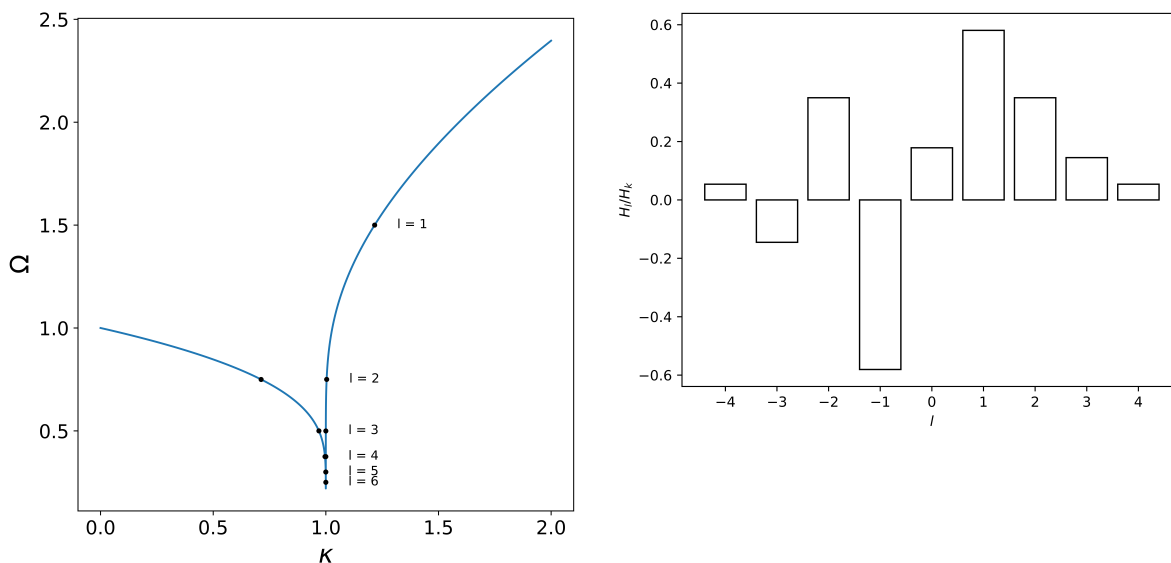
Figure 6.3: Left: Dependency of the canonical frequency Ω on the energy with harmonic resonances ($l < 7$) and their separatrix width. The separatrix width is in point size. Right: Spectrum for a perturbation $\propto \cos(kx)$ with $k = 1$ in harmonics l of the canonical angle for $E_{\mathrm{res}} = 1.4252 U_0$ [1]

.

Using this result, the initial condition of p_x was set as $p_x = \sqrt{2mE_{\mathrm{res}} - p_y^2}$. The system was perturbed in an interval of $\Delta p_y = [0.965 p_{y,\mathrm{res}}, 1.03 p_{y,\mathrm{res}}]$. As shown in Fig. 6.6, the standard map is in accordance to the numerical results for the $(\Delta \bar{J}, \bar{\theta})$ phase space given in Eq. 5.50 and 5.49. The mappings exhibit the same behaviour as the one-dimensional free particle and pendulum.

For this model, resonance lines (Fig. 6.7) were calculated for a comparison with the data of a tokamak, because of the similarity of the model to the system of a tokamak as discussed in chapter 8. For the calculation of the resonance lines, p_y was chosen in an interval of $p_y = [-4, 4]$ to calculate the resonance energy for modes $l = [-4, 4]$ and $n = 3$.

The resonance lines are perfectly symmetric in the canonical momentum p_y, because the canonical frequency Ω^y is directly proportional to the canonical momentum. The particles with $E/E_{\mathrm{sep}} > 1$ are passing particles, whereas particles on the left side of the separatrix are trapped particles. For $l = 0$, the resonance condition 6.5 can only be satisfied if $p_y = 0$. This resonance corresponds to the superbanana resonance in the tokamak.
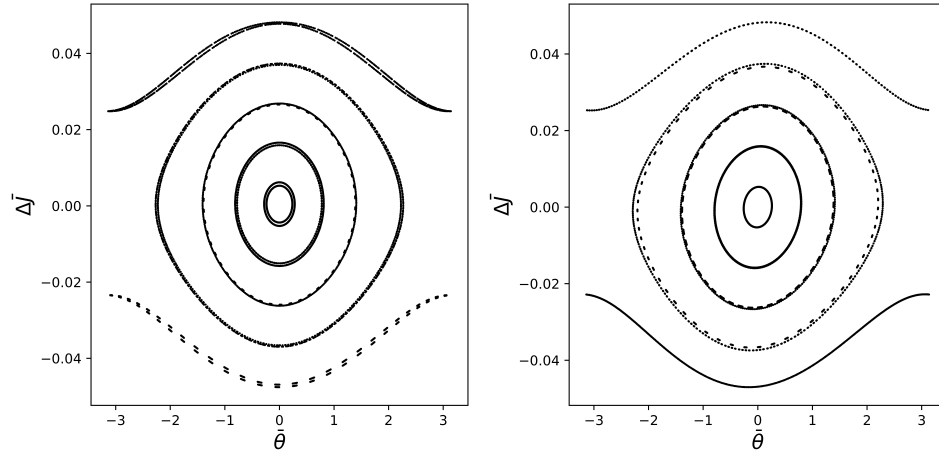
(a) $n = 2$, $|H_k|/U_0 = 10^{-3}$, $E_{\mathrm{res}} = 1.4252 U_0$, $K = 0.02$.
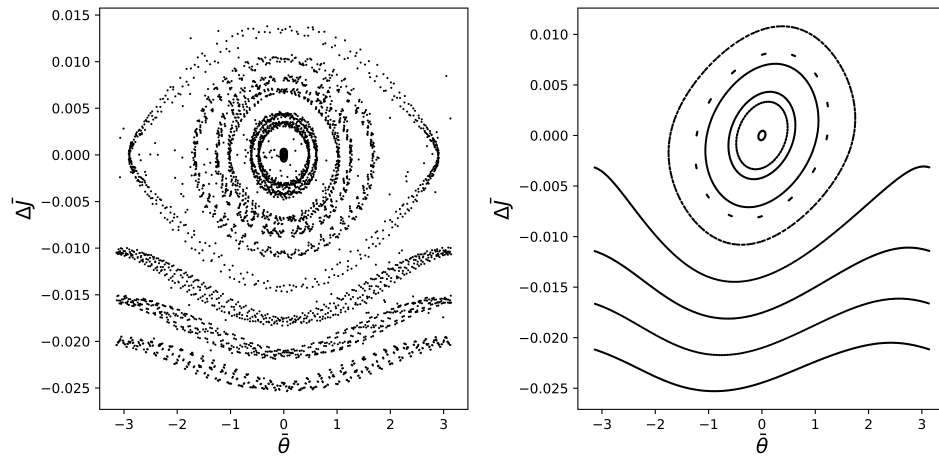
(b) $n = 3$, $|H_k|/U_0 = 10^{-3}$, $E_{\mathrm{res}} = 1.9382 U_0$, $K = 0.24$.
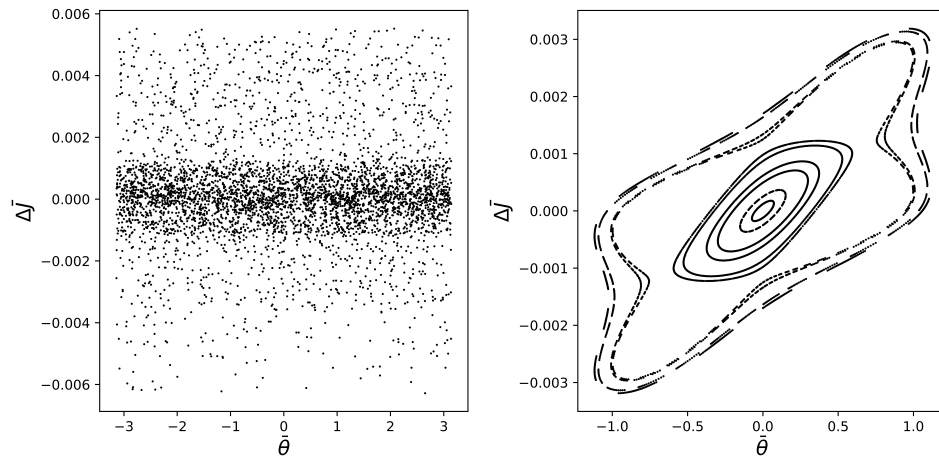
(c) $n = 4$, $|H_k|/U_0 = 10^{-3}$, $E_{\mathrm{res}} = 1.9925 U_0$, $K = 2.17$.

Figure 6.4: Pendulum in one dimension: Comparison of the numerical results for $\Delta \bar{J}, \bar{\theta}$ (left) and the standard map (right) for several trapped resonances for $\omega = 1.5\omega_0$. 10 initial conditions and $N = 500$ iterations for each map were used.
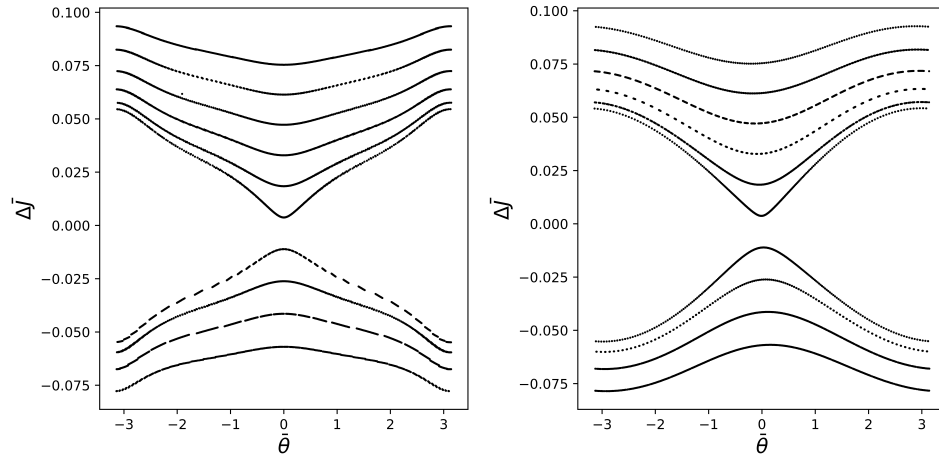
(a) $n = 1$, $|H_k|/U_0 = 10^{-3}$, $E_{\mathrm{res}} = 2.4332U_0$, $K = 0.02$.
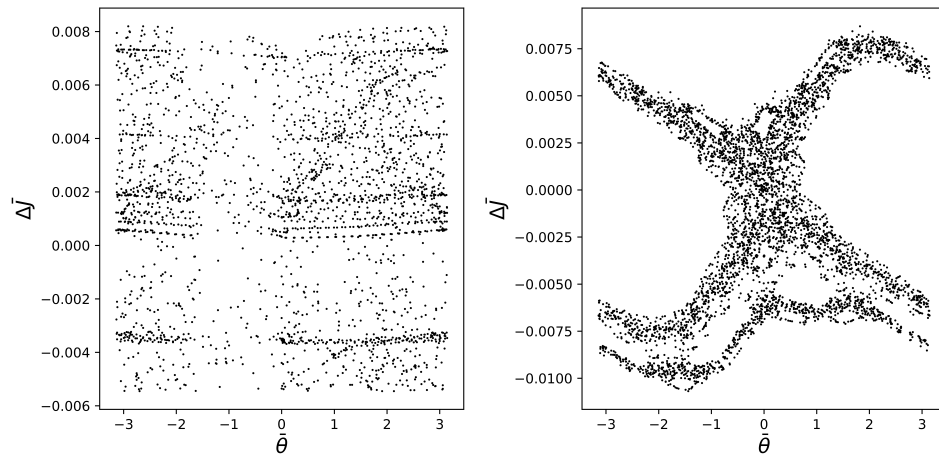
(b) $n = 2$, $|H_k|/U_0 = 10^{-3}$, $E_{\mathrm{res}} = 2.0073U_0$, $K = 1.10$.
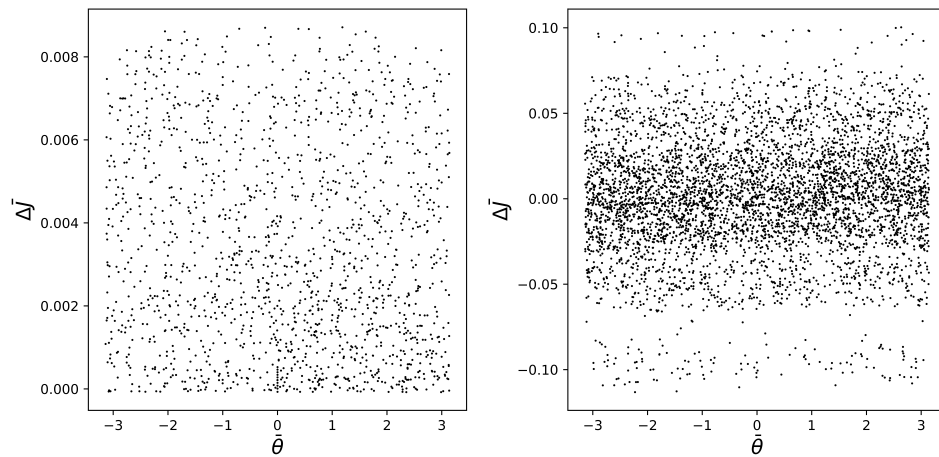
(c) $n = 3$, $|H_k|/U_0 = 10^{-3}$, $E_{\mathrm{res}} = 2.0001U_0$, $K = 64.93$.

Figure 6.5: Pendulum in one dimension: Comparison of the numerical results for $\Delta\bar{J},\bar{\theta}$ and the standard map for several passing resonances for $\omega = 1.5\omega_0$. 10 initial conditions and $N = 500$ iterations for each map were used.
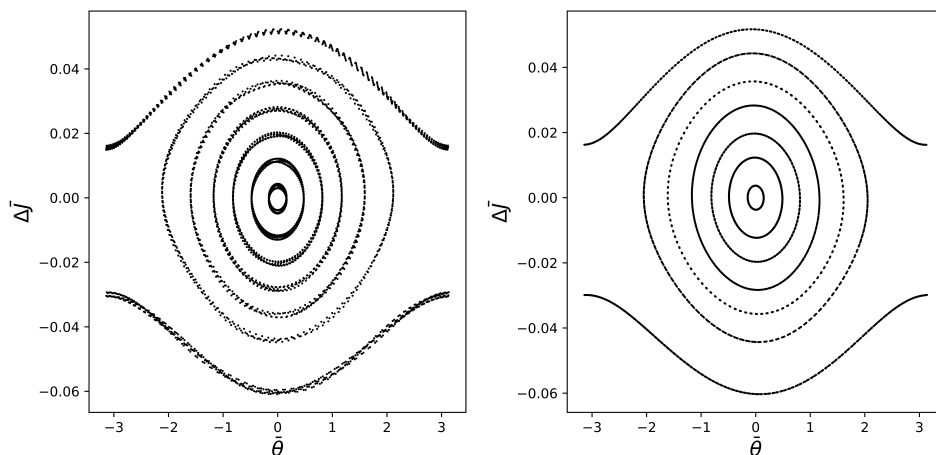
Figure 6.6: Pendulum with two degrees of freedom: Comparison of the numerical results for $\Delta \bar{J}, \bar{\theta}$ (left) and the standard map (right) for a trapped resonance of modes $n = -2$ and $l = 1$. $|H_k|/U_0 = 10^{-3}$, $E_{\text{res}} = 2.409U_0$, $p_{y,\text{res}} = 1.72$. 10 initial conditions in an interval of $\Delta p_y = [0.965p_{y,\text{res}}, 1.03p_{y,\text{res}}]$ and $N = 500$ iterations were used. The resulting stochasticity parameter is $K = 0.004$.

For further analysis, the resonance widths were calculated (Fig. 6.8). The resonance widths in E and p_y are given via the relations,

$$\Delta E \quad = \quad \pm 2H_{\boldsymbol{m}}, \tag{6.6}$$

$$\Delta p_y \quad = \quad \pm 2n\sqrt{\frac{H_{\boldsymbol{m}}}{\bar{\Omega}'}}, \tag{6.7}$$

resulting from secular perturbation theory (chapter 2).

Depending on the perturbation amplitude, resonance lines for trapped particles start overlapping not only with the separatrix, shown as a black line, but also with neighbouring resonance lines as shown in Fig. 6.9 and Fig. 6.10 for different perturbation amplitudes. The resonance width for passing orbits is within point size. If resonance lines are overlapping, it results in stochastic motion as particles can now pass from one resonance to another.

For the resonance lines $n = 3$ and $l = [1,2,3,4]$, the resulting stochasticity parameter K was calculated for the perturbation amplitude $|H_k| = 10^{-2}$ (Fig. 6.11). The degree of chaos in the system increases while approaching the separatrix. At the separatrix, there is an asymptotic behaviour of K as the system there is unstable.
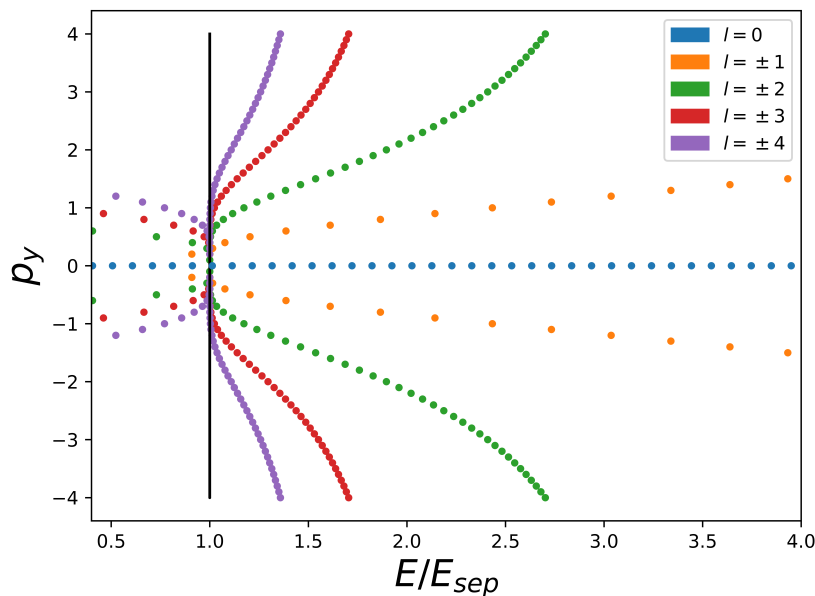
Figure 6.7: Resonance lines for $l = 3$ calculated using Eq. 6.5, normalized by the separatrix energy E_{sep}. The initial conditions are $p_y = [-4,4]$. The black line denotes the separatrix.
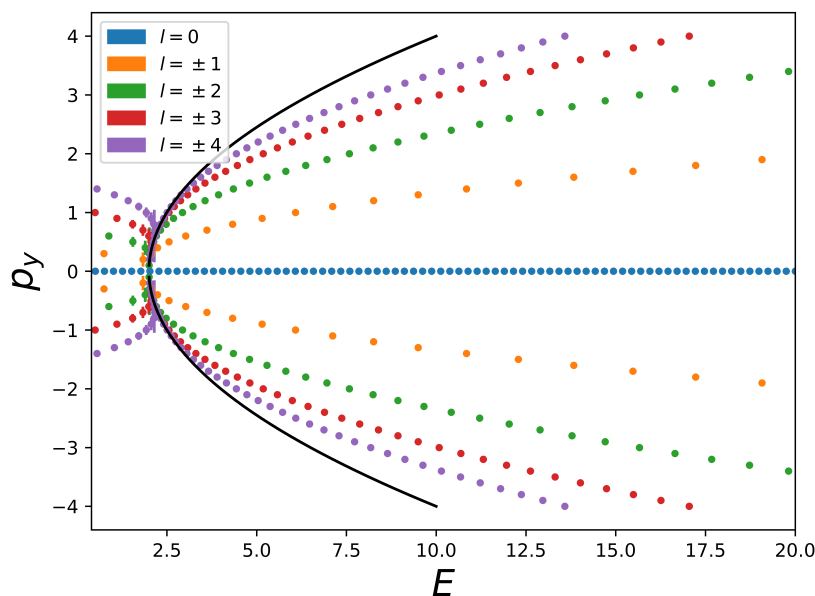
Figure 6.8: Resonance lines for $l = 3$ calculated using Eq. 6.5. The initial conditions are $p_y = [-4,4]$ and the perturbation amplitude $|H_k|/U_0 = 10^{-2}$. The black line denotes the separatrix. The resonance width in E and p_y are calculated using Eq.6.6 and 6.7.
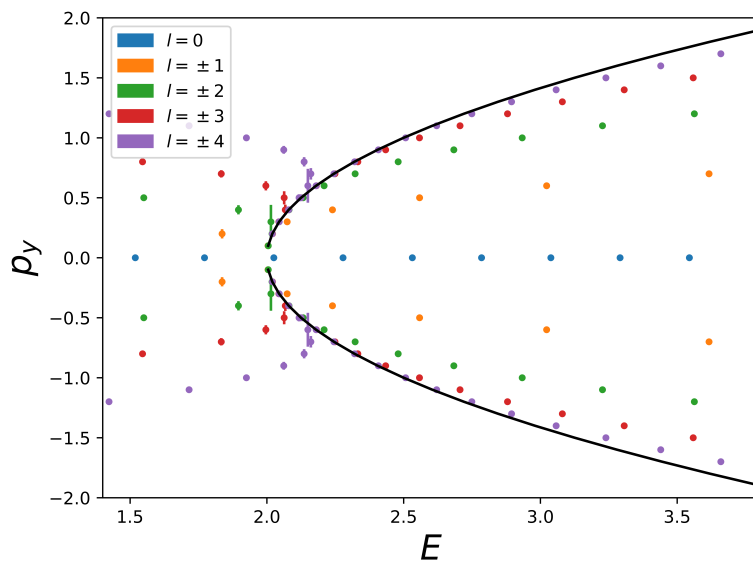
Figure 6.9: Magnification of the region around the separatrix for the resonance lines for $l = 3$ calculated using Eq. 6.5. The initial conditions are $p_y = [-4,4]$ and the perturbation amplitude $|H_k|/U_0 = 10^{-3}$. The black line denotes the separatrix. The errorbars in E and p_y are calculated using Eq. 6.6 and 6.7.
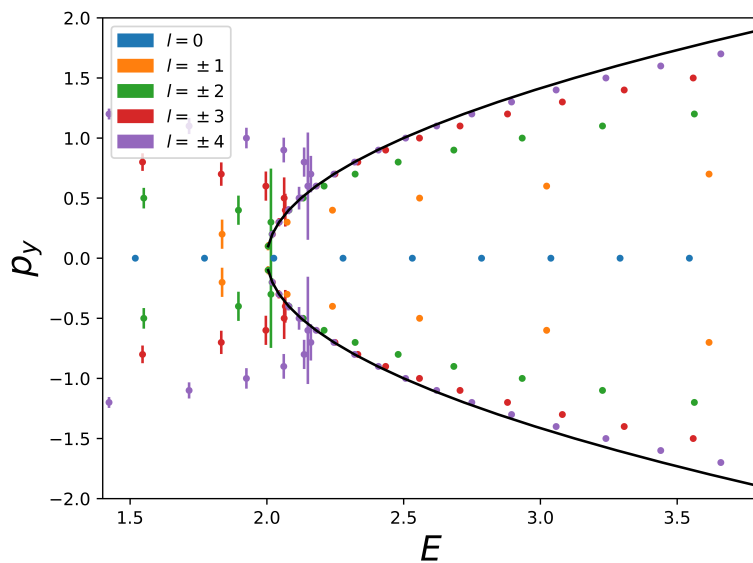
Figure 6.10: Magnification of the region around the separatrix for the resonance lines for $l = 3$ calculated using Eq. 6.5. The initial conditions are $p_y = [-4,4]$ and the perturbation amplitude $|H_k|/U_0 = 10^{-2}$. The black line denotes the separatrix. The errorbars in E and p_y are calculated using Eq. 6.6 and 6.7.
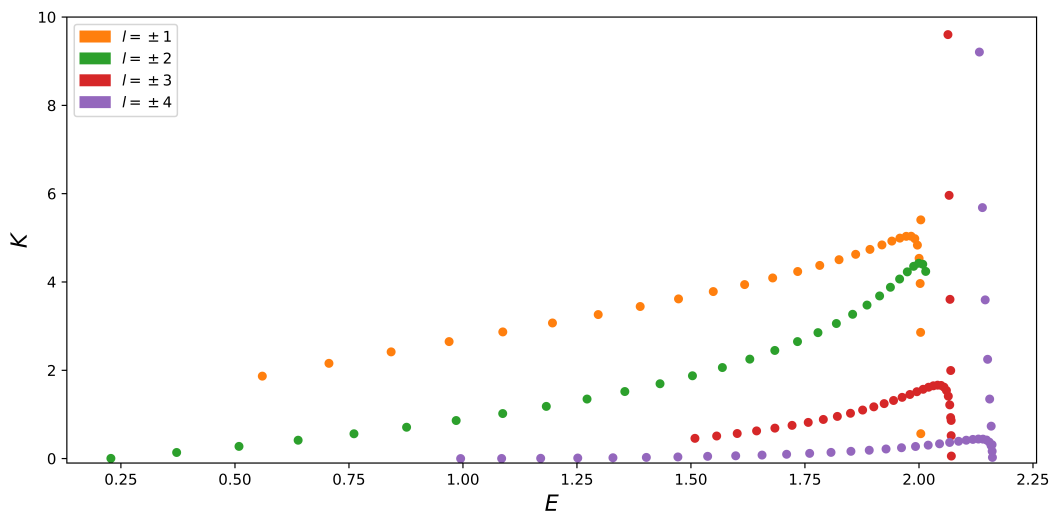
Figure 6.11: Stochasticity parameter K for the resonance lines $n = 3$ as a function of the energy, normalized with E_{sep}. The initial conditions are $p_y = [0.1, 0.8]$ and the perturbation amplitude $|H_k|/U_0 = 10^{-2}$.

Chapter 7

Hamiltonian theory in the tokamak

The core of the physics of plasma are the physics of motion of charged particles in an electromagnetic field. In a homogeneous magnetic field $\boldsymbol{B}$, a charged particle gyrates in a helix along magnetic field lines, while conserving its kinetic energy. In a constant electric field $\boldsymbol{E}$, the particle experiences uniform acceleration in the direction of the field. If, however, both fields act simultaneously on the particle, the motion gets more complex, as the particle experiences other drift forces.

Moreover, a realistic field is not globally uniform and a spatially inhomogeneous and non-stationary field complicates the equations of motion to a set of non-linear equations. For slowly varying fields in time and space, *guiding center theory* can be used. Slowly varying means that the characteristic length l and time τ are large compared to the gyoradius and the gyroperiod respectively, satisfying

$$\frac{\rho}{l} \ll 1, \tag{7.1}$$

$$\frac{1}{\omega_c \tau} \ll 1, \tag{7.2}$$

where ω_c is frequency of gyration (cyclotron frequency) given by

$$\omega_c = \frac{eB}{cm}, \tag{7.3}$$

with e is the charge and m is the mass of the particle. B is the magnetic field strength. The aim is to describe the motion of a particle as a fast gyration around a slowly drifting guiding center.

In this chapter, the simple aspects of the motion of a single charged particle in electromagnetic fields and the occurring drifts are studied. Guiding center theory is introduced. As the radius of gyration is small compared to the plasma radius, the average particle position can be determined by following the guiding center through phase space. The guiding center phase space Lagrangian is introduced in section 7.2 and is transformed

to its canonical form. Finally, the construction of action-angle variables for charged particle motion in an axisymmetric toroidal system is summarized.

7.1 Motion of a charged particle in an electromagnetic field

The equation of motion of a charged particle in a spatially and temporally uniform electromagnetic field takes the form

$$m\frac{d\boldsymbol{u}}{dt} = e(\boldsymbol{E} + \frac{\boldsymbol{u}}{c} \times \boldsymbol{B}), \tag{7.4}$$

where c is the speed of light, $\boldsymbol{u}$ the particle velocity, m is the particle mass and $\boldsymbol{E}$ and $\boldsymbol{B}$ are the electric and magnetic field, respectively. The particle velocity is split into components parallel and perpendicular to the magnetic field,

$$\boldsymbol{u} = u_\parallel \boldsymbol{b} + \boldsymbol{u}_\perp, \tag{7.5}$$

where $\boldsymbol{b} = \boldsymbol{B}/B$ is the unit vector in the direction of the magnetic field. $u_\parallel$ is only affected by the electrical field,

$$\frac{du_\parallel}{dt} = \frac{e}{m}E_\parallel. \tag{7.6}$$

The perpendicular component $\boldsymbol{u}_\perp$ is driven by the Lorentz force, that forces the particle to gyrate around the magnetic field line with a gyration radius ρ_L,

$$\rho_L = \frac{|\boldsymbol{u}_\perp|}{\omega_c}. \tag{7.7}$$

The result for $\boldsymbol{u}_\perp$ is

$$\boldsymbol{u}_\perp = \frac{\boldsymbol{E} \times \boldsymbol{B}}{B^2} + \rho_L\omega_c(\boldsymbol{e}_1\sin(\omega_c t + \gamma_0) + \boldsymbol{e}_2\cos(\omega_c t + \gamma_0)), \tag{7.8}$$

where $\boldsymbol{e}_1, \boldsymbol{e}_2$ are unit vectors perpendicular to each other and to $\boldsymbol{B}$. Hence, the motion can be decomposed into gyration around the magnetic field with the gyrofrequency ω_c and a steady drift at velocity $\boldsymbol{v}_E$,

$$\boldsymbol{v}_E = c\frac{\boldsymbol{E} \times \boldsymbol{B}}{B^2}. \tag{7.9}$$

$\boldsymbol{v}_E$ is called electric drift velocity due to the $(E \times B)$-*drift*, that is identical for all species as it does not depend on the sign of the charge. This drift can be understood qualitatively: a particle moving in the direction of $\boldsymbol{E}$ accelerates and is hence bent less by the magnetic field resulting in a gradual increase of ρ_L. However, going against the electrical field, the particle is slowed down and the gyroradius decreases to its original value.

If another constant force $\boldsymbol{F}$ acts on the particle, the particle experiences another drift arising from the perpendicular component of $\boldsymbol{F}$,

$$\boldsymbol{v}_{g,\perp} = \frac{c}{eB^2}\boldsymbol{F}_\perp \times \boldsymbol{B}. \tag{7.10}$$

An example of an additional constant force is the gravitational force $\boldsymbol{F}_g = m\boldsymbol{g}$. However, the resulting drift is negligible in fusion plasmas.

Another modification of the gyromotion is due to the curvature of magnetic field lines. If a particle moves along a curved field line, it experiences a centrifugal force giving rise to a slow drift perpendicular to both the local direction of the magnetic field and the direction to the local center of curvature of the field,

$$\boldsymbol{v}_c = \frac{mcu_\parallel^2}{eB^4}\boldsymbol{B} \times (\boldsymbol{B} \cdot \nabla)\boldsymbol{B}. \tag{7.11}$$

Moreover, in a non-uniform magnetic field, a particle will acquire a drift velocity

$$\boldsymbol{v}_{\nabla B} = \frac{mcu_\perp^2}{2eB^3}\boldsymbol{B} \times (\boldsymbol{B} \cdot \nabla)\boldsymbol{B}, \tag{7.12}$$

due to the called ∇B-*drift*.

Finally, if the electric field depends on time, the $(E \times B)$-*drift* is not constant and gives rise to the *polarization drift*,

$$\boldsymbol{v}_p = \frac{cm}{eB^2}\frac{\partial \boldsymbol{E}}{\partial t}, \tag{7.13}$$

that takes into account the constantly changing polarization of the plasma medium.

The motion of a particle in an magnetic field can be described in guiding center theory as a motion split into the slow motion of the guiding center of gyration $\boldsymbol{r}$ and the rapidly changing radius of gyration $\boldsymbol{\rho_L}$,

$$\boldsymbol{R} = \boldsymbol{r} - \boldsymbol{\rho_L}. \tag{7.14}$$

Besides the transformation of the spatial coordinates, the parallel velocity $v_\parallel$ is introduced,

$$v_\parallel = \boldsymbol{b} \cdot \dot{\boldsymbol{R}}. \tag{7.15}$$

To fully describe the six dimensional phase space, the gyroaction variable $J_\perp$,

$$J_\perp = \frac{m^2 c |\boldsymbol{w}|^2}{2eB}, \tag{7.16}$$

where $\boldsymbol{w} = \boldsymbol{v}_\perp - \boldsymbol{v}_E$ is the perpendicular velocity in the local frame moving with the $(E \times B)$-drift velocity, is used. The sixth phase space variable is the gyrophase ϕ that gives the location of the particle around the guiding center.

This change of variables $(\boldsymbol{r}, \boldsymbol{v}) \to (\boldsymbol{R}, v_\parallel, J_\perp, \phi)$ is done in such a way that the new spatial guiding center variables are free of oscillations along the particle trajectory, which are performed only by the ignorable variable ϕ.

7.2 Guiding center Lagrangian

To obtain the guiding center Lagrangian as presented in [19], the following approximations are used. Several terms are of the order ϵ as the radius of gyration $\rho_L \propto \epsilon$ and will be neglected. Furthermore, the gyrophase ϕ is averaged over one gyroperiod.

Thus, the Lagrangian in terms of guiding center variables $(\boldsymbol{R}, v_\parallel, J_\perp, \phi)$ is

$$L = \left(m v_\parallel(\boldsymbol{R}, J_\perp, H) \boldsymbol{b}(\boldsymbol{R}) + \frac{e}{c} \boldsymbol{A}(\boldsymbol{R}) \right) \dot{\boldsymbol{R}} + J_\perp \dot{\phi} - H_{gc}, \tag{7.17}$$

with $\boldsymbol{A}(\boldsymbol{R})$ being the vector potential for the magnetic field and the guiding center Hamiltonian

$$H_{gc} = \frac{m v_\parallel^2}{2} + e\Phi(\boldsymbol{R}) + J_\perp \omega_c(\boldsymbol{R}). \tag{7.18}$$

There is no dependency on the gyrophase ϕ in this approximation, so we conclude that $J_\perp$ is conserved. Also, the total energy H_{gc} is conserved as there is no time dependence.

The Euler-Lagrange equations are calculated as presented in chapter 1. The variation of L with respect to $v_\parallel$ gives

$$0 = \frac{\partial L}{\partial v_\parallel} = m\dot{\boldsymbol{R}} \cdot \boldsymbol{b} - \frac{\partial H_{gc}}{\partial v_\parallel}$$
$$= m\dot{\boldsymbol{R}} \cdot \boldsymbol{b} - mv_\parallel, \tag{7.19}$$

which yields

$$v_\parallel = \dot{\boldsymbol{R}} \cdot \boldsymbol{b}. \tag{7.20}$$

Hence, $v_\parallel$ is the velocity of the guiding center in the direction of the magnetic field. The variation of L with respect to the guiding center position $\boldsymbol{R}$ gives

$$0 = \frac{\partial L}{\partial \boldsymbol{R}} = \nabla L$$
$$= \left(\nabla \left(mv_\parallel(\boldsymbol{R}, J_\perp, H)\boldsymbol{b}(\boldsymbol{R}) + \frac{e}{c}\boldsymbol{A}(\boldsymbol{R}) \right) \dot{\boldsymbol{R}} \right) - J_\perp \nabla \omega_c - e\nabla\Phi. \tag{7.21}$$

Introducing $\boldsymbol{A}^* = \frac{c}{e}mv_\parallel\boldsymbol{b} + \boldsymbol{A}$, we get

$$m\dot{v}_\parallel\boldsymbol{b} = \frac{e}{c}\dot{\boldsymbol{R}} \times (\nabla \times \boldsymbol{A}^*) - \mu\nabla B - e\nabla\Phi. \tag{7.22}$$

Taking now the cross product with $\boldsymbol{b}$, introducing $\boldsymbol{B}^* = \nabla \times \boldsymbol{A}^*$ and using $v_\parallel = \dot{\boldsymbol{R}} \cdot \boldsymbol{b}$, we get

$$\boldsymbol{b} \times \left(m\dot{v}_\parallel\boldsymbol{b} \right) + \mu\boldsymbol{b} \times \nabla B + e\boldsymbol{b} \times \nabla\Phi = \frac{e}{c}\boldsymbol{b} \times \left(\dot{\boldsymbol{R}} \times \boldsymbol{B}^* \right). \tag{7.23}$$

We use now the vector identity $((\nabla\boldsymbol{v}) \cdot \boldsymbol{w} - (\boldsymbol{v} \cdot \nabla)\boldsymbol{w}) = \boldsymbol{w} \times (\nabla \times \boldsymbol{v})$ and get for the LHS of Eq. 7.23

$$(\boldsymbol{b} \cdot \boldsymbol{B}^*)\dot{\boldsymbol{R}} - (\boldsymbol{b} \cdot \dot{\boldsymbol{R}})\boldsymbol{B}^* = (\boldsymbol{b} \cdot \boldsymbol{B}^*)\dot{\boldsymbol{R}} - v_\parallel\boldsymbol{B}^* \tag{7.24}$$

Dividing by $\boldsymbol{b} \cdot \boldsymbol{B}^*$, we get the equation of motion

$$\dot{\boldsymbol{R}} = \frac{1}{\boldsymbol{b} \cdot \boldsymbol{B}^*}(v_\parallel\boldsymbol{B}^* + \mu\boldsymbol{b} \times \nabla B + e\boldsymbol{b} \times \nabla\Phi) \tag{7.25}$$

The drifts mentioned earlier are apparent in this equation of motion. The second term the ∇B-drift and the third term is the $(E \times B)$-drift. The polarization drift does not appear here, as there was no explicit time dependence of the electric field. The curvature

drift depends on the curvature of the magnetic field lines and by studying the first term only in first order we get

$$\frac{v_\parallel \boldsymbol{B}^*}{\boldsymbol{b} \cdot \boldsymbol{B}^*} = \frac{ev_\parallel}{mc} \left(v_\parallel (\nabla \times \boldsymbol{b}) \times \boldsymbol{b} B - B v_\parallel (\nabla \times \boldsymbol{b}) - \omega_c \boldsymbol{B} \right). \tag{7.26}$$

As $\boldsymbol{b} \times (\nabla \cdot \boldsymbol{b})\boldsymbol{b} = -\boldsymbol{b} \times \boldsymbol{b} \times ((\nabla \times \boldsymbol{b})) = -\boldsymbol{b} \cdot (\nabla \times \boldsymbol{b})\boldsymbol{b} + (\nabla \times \boldsymbol{b})$, we take the cross product with $\boldsymbol{b}$ and get

$$\frac{ev_\parallel}{mc} \left(-\boldsymbol{b} \times ((\nabla \cdot \boldsymbol{b}) \cdot \boldsymbol{b})v_\parallel B - \omega_c \boldsymbol{B} \right) = v_\parallel \boldsymbol{b} - \boldsymbol{b} \times ((\nabla \cdot \boldsymbol{b}) \cdot \boldsymbol{b})\frac{v_\parallel^2}{\omega_c}. \tag{7.27}$$

The first term represents the parallel motion along the field lines and the second term is equivalent to the curvature drift.

For the construction of action-angle coordinates in the axisymmetric geometry of a tokamak, straight field-line flux coordinates $\boldsymbol{R} = \boldsymbol{R}(r,\theta,\varphi)$ are used [7]. Here, the radial component of the vector potential $\boldsymbol{A}$ vanishes and the Lagrangian reduces to

$$L = mv_\parallel b_r \dot{r} + (mv_\parallel b_\theta + \frac{e}{c}A_\theta)\dot{\theta} + (mv_\parallel b_\varphi + \frac{e}{c}A_\varphi)\dot{\varphi} + J_\perp \dot{\phi} - H_{gc}, \tag{7.28}$$

with

$$H_{gc} = H_{gc}(r, \theta, J_\perp, v_\parallel) = \frac{mv_\parallel^2}{2} + \frac{J_\perp e}{mc}B + e\Phi. \tag{7.29}$$

To illustrate the general principle, one can neglect cross-field drifts. Then, motion only occurs along magnetic field lines and dynamics are driven by the mirroring force due to the increase of the magnetic field modulus on the inboard side of the torus. Moreover, if variations of $e\Phi$ are assumed to be small and the limit of large aspect ratio is considered, the magnetic field $\boldsymbol{B}$ can be approximated by

$$B(r,\theta) \approx B_0(r) \cdot (1 - \epsilon_t \cos(\theta)), \tag{7.30}$$

with $\epsilon_t = r/R_0$, the inverse aspect ratio describing the ratio between minor r and major R_0 radii of the flux surface. With the definition $p_\parallel = mv_\parallel$ and the neglection of the constant term $e\Phi$, the Hamiltonian is equivalent to the Hamiltonian of the one-dimensional pendulum,

$$H_{gc}(\theta, p_\parallel) = \frac{p_\parallel^2}{2m} + \frac{J_\perp e}{mc}B_0(1 - \epsilon_t \cos(\theta)). \tag{7.31}$$

The guiding center orbits in a tokamak are described by the pitch-angle variable η, defined as

$$\eta = \frac{2\mu}{mv^2}. \tag{7.32}$$

If a particle, with a given energy E and magnetic moment μ, moves on a flux surface, on which the magnetic field strength varies between B_{min} and B_{max} on the outboard and inboard side of the torus respectively, it can never enter a region where $\mu B > E - e\Phi$. Thus, particles with

$$\frac{1}{B_{max}} < \eta < \frac{1}{B_{min}} \tag{7.33}$$

are referred to as *trapped* as particles are reflected by the mirror force. At the reflection points, $v_{\parallel} = 0$. Particles with

$$0 < \eta < \frac{1}{B_{max}} \tag{7.34}$$

are *passing* particles and free to move along the whole flux surface. The orbits for passing and trapped particles are shown in Fig. 7.1. As trapped particles have orbits of a distinct shape, they are often referred to as banana orbits.

Thus, particle motion in a large aspect ratio tokamak is analogous to the motion of a pendulum, where trapped and passing motion in the tokamak corresponds to libration and rotation of a pendulum.

As drifts act on the particles, guiding center orbits are toroidally precessing with the average toroidal precession velocity $\langle \dot{\varphi} \rangle = \Omega_t$ as illustrated in Fig. 7.2.

7.3 Action angle variables in a tokamak

In [1], exact expressions for action-angle variables in a tokamak have been constructed based on the canonical form of the guiding center Lagrangian given in Eq. 7.28. The main steps are summarized here. The *small orbit width approximation* was used implying that the orbit width is small compared to the radial scale of fields. Therefore all higher order terms than first order of $r - r_{\varphi}$ are neglected, where r_{φ} specifies the banana tip radius.

As there are three constants of motion for a particle in a stationary axisymmetric magnetic field [17],
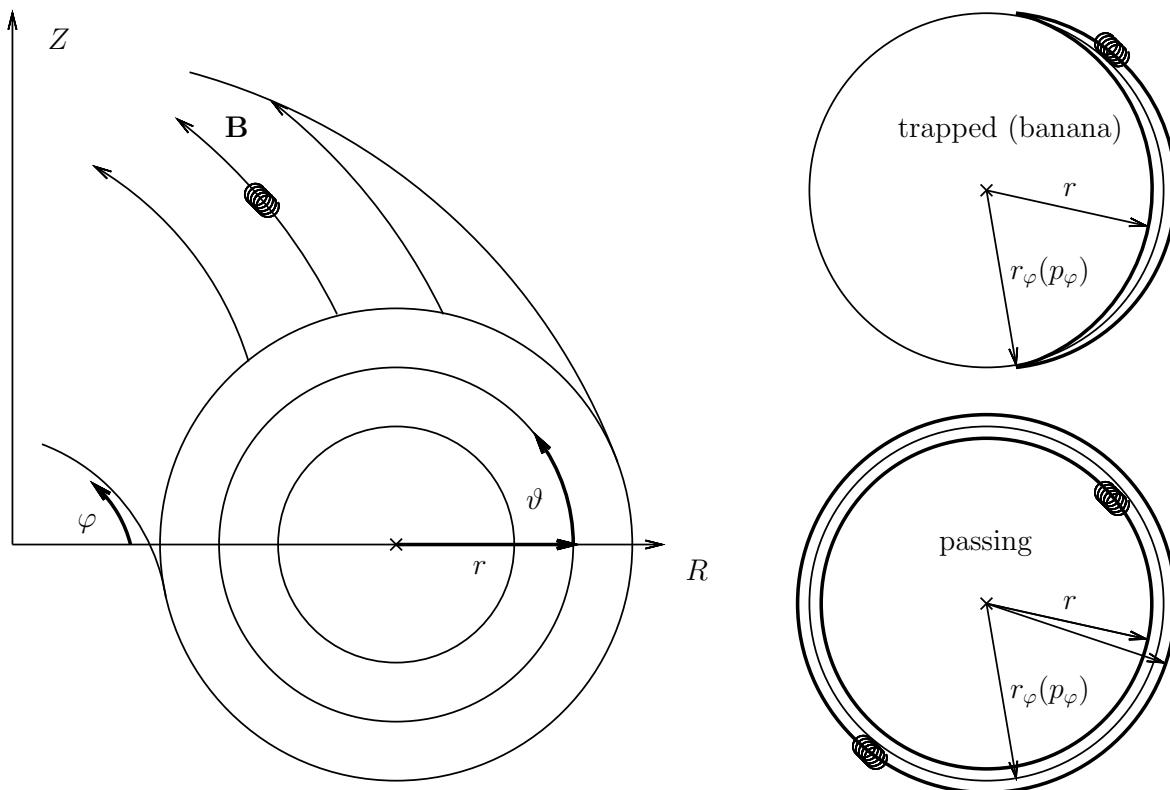
Figure 7.1: Illustration of guiding center orbits in a tokamak for trapped and passing particles. Trapped particles are reflected by the mirror force as the magnetic field modulus increases on the inboard side of the torus.

$$E \quad = \quad \frac{mv_\parallel^2}{2} + e\Phi + \frac{J_\perp e}{mc}B, \tag{7.35}$$

$$J_\perp \quad = \quad \frac{m^2 c |\boldsymbol{w}|^2}{2eB}, \tag{7.36}$$

$$p_\varphi \quad = \quad \frac{e_\alpha}{c} A_\varphi(r_\varphi) = -\frac{e_\alpha}{c}\psi_{pol}(r_\varphi), \tag{7.37}$$

they are used as constants of motion $\boldsymbol{\alpha} = (J_\perp, E, p_\varphi)$. For the transformation to action-angle variables, the phase space is defined by the coordinates $(\phi, \theta, \varphi, \boldsymbol{\alpha})$. This is a quasi 1D system, because $H = H(\theta, \boldsymbol{\alpha})$ and hence, there are only spatial dependencies on one coordinate. The actions of (ϕ, φ) are their two invariant momenta,

$$J_1 = J_\perp, \tag{7.38}$$

$$J_3 = p_\varphi. \tag{7.39}$$
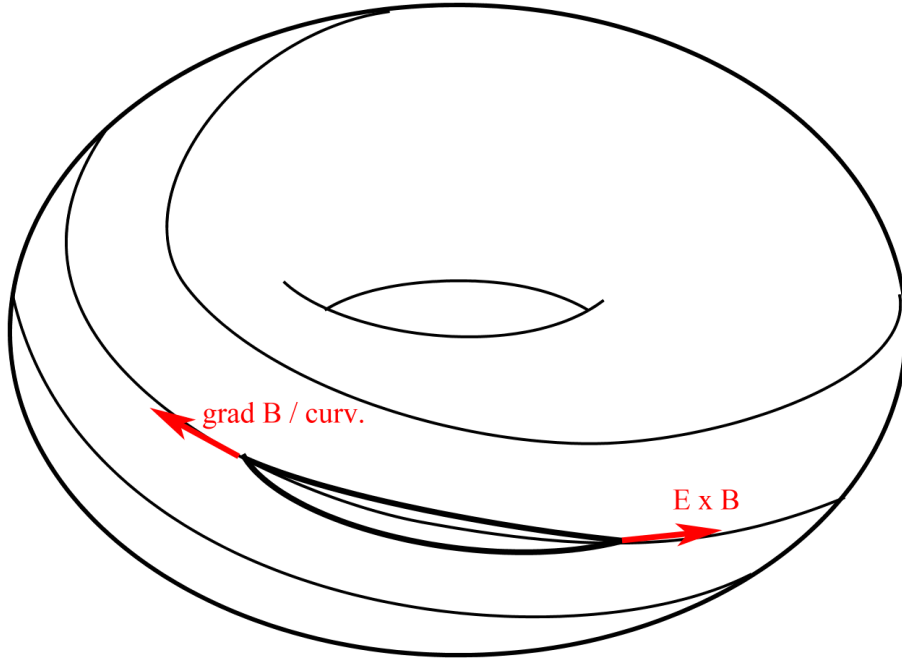
Figure 7.2: Orbits in the tokamak experience magnetic and electric drifts. On average over bounce time, orbits are toroidally precessing with the average toroidal precession velocity $\langle \dot{\varphi} \rangle$.

For the poloidal action $J_2 = J_\theta$ an integral over the bounce time τ_b has to be performed (see [1, chapter 3]). Applying the *small orbit width approximation*, we get an approximate expression for the poloidal action,

$$J_\theta = \frac{1}{2\pi} \int d\theta p_\theta = \frac{e}{c} A_\theta \delta_{tp} + J_\parallel + \mathcal{O}(\varepsilon^2), \tag{7.40}$$

where δ_{tp} is 0 for trapped, and 1 for passing particles. $J_\parallel$ is the adiabatic invariant proportional to the bounce average of $v_\parallel^2$,

$$J_\parallel \propto \langle v_\parallel^2 \rangle_b. \tag{7.41}$$

The corresponding canonical frequencies defining the resonance condition are given by,

$$\Omega^\theta = \omega_b, \tag{7.42}$$
$$\Omega^\phi = \langle \omega_c \rangle_b, \tag{7.43}$$
$$\Omega^\varphi = q\omega_b \delta_{tp} + \Omega_t, \tag{7.44}$$

where q is the safety factor, Ω_t is the toroidal canonical frequency $\Omega_t = \langle v_g^\varphi \rangle_b$ and v_g^φ is the toroidal precession frequency of a particle generated by $(E \times B)$ and magnetic drift on the flux surface. Ω_t can be decomposed into its electric and magnetic part, as later used for the resonance condition,

$$\Omega_t = \langle \Omega_{tE} \rangle_b + \langle \Omega_{tB} \rangle_b. \tag{7.45}$$

Chapter 8

Analysis of drift-orbit resonances in tokamak plasmas

In this chapter, resonance overlap and the subsequent appearance of chaotic motion for drift-orbit resonances in tokamak plasmas is studied to test the validity range of the results of [1].

8.1 Background

A non-axisymmetric quasistatic magnetic perturbation to the originally axisymmetric field is introduced by changing the magnetic module $B = |\boldsymbol{B}_0| + B_1$ in Boozer magnetic coordinates [1]. The Hamiltonian is of the form $H = H_0 + H_1 + \mathcal{O}((B_1/B_0)^2)$, with

$$
\begin{aligned}
H_0 &= \frac{mv_\parallel^2}{2} + J_\perp \omega_c, & (8.1) \\
H_1 &= \left(\omega_c J_\perp + mv_\parallel^2\right) \frac{B_1}{B_0}, & (8.2)
\end{aligned}
$$

where the non-axisymmetric quasistatic magnetic perturbation is given as

$$
B_1(\vartheta,\varphi) = \sum_n B_n(\vartheta)e^{in\varphi}. \tag{8.3}
$$

This corresponds to a harmonic perturbation of the form

$$
H_1 = \sum_{\boldsymbol{m}} H_{\boldsymbol{m}} e^{im_k \theta^k}. \tag{8.4}
$$

The Fourier modes of H_1 in $\boldsymbol{\theta}$ are calculated by bounce averaging

$$H_{\boldsymbol{m}} = \left\langle H_n(\vartheta(\tau))e^{inq\vartheta(\tau)-i(m_2+nq\delta_{\mathrm{tp}})\omega_b\tau}\right\rangle_b, \tag{8.5}$$

where q is the safety factor, δ_{tp} is 1 for passing orbits and 0 for trapped orbits, ω_b is the bounce frequency, and where the toroidal harmonics $H_n(\vartheta)$ depend on the perturbation of the magnetic modulus $B_n(\vartheta)$ on the flux surface with $r = r_\varphi$,

$$H_n(\vartheta) = \left(\frac{e}{mc}J_\perp B_0(\vartheta) + mv_\parallel^2\right)\frac{B_n(\vartheta)}{B_0(\vartheta)}. \tag{8.6}$$

The harmonics were specified to be $m_1 = 0$ (canonical gyro), $m_2 = l$ (canonical poloidal) and $m_3 = n$ (canonical toroidal) of H_1. The harmonic for the gyration was chosen to be zero, as only this harmonic allows to fulfill the resonance condition, since ω_c is much larger than ω_b and $\Omega^{\varphi 1}$. The considered perturbation, a *RMP-like case*, is a long scale perturbation with $n = 3$ and is typical for the perturbations produced by ELM mitigation coils.

The velocity space (implying the energy space) was parametrized for calculations and values for the normalized perpendicular invariant η, related to $J_\perp$ and $v_\parallel$ via

$$J_\perp = \frac{mv^2}{2}\frac{mc}{e}\eta, \tag{8.7}$$

$$v_\parallel = \sigma v\sqrt{1-\eta B}, \tag{8.8}$$

were found for which the resonance condition

$$m_k\Omega^k(v,\eta,p_\varphi) = l\Omega^2 + n\Omega^3 \tag{8.9}$$

$$= (l + qn\delta_{\mathrm{tp}})\omega_b + n\Omega_t = 0 \tag{8.10}$$

holds.

Here, the bounce-averaged toroidal drift frequency Ω_t is given by

$$\Omega_t = \langle\Omega_{tB}\rangle_b + \langle\Omega_{tE}\rangle_b \tag{8.11}$$

where the bounce averaged is used as defined as in Eq. 5.43 and contains magnetic (∇B- and curvature) drift Ω_{tB} and electric ($E \times B$)-drift Ω_{tE} on a flux surface. This gives us the resonance line in the (v, η) phase space for a fixed value of $p_\varphi(r_\varphi)$.

---

[1]Finite modes in m_2 describe heating by cyclotron resonance.

For orbit resonances, two cases have to be distinguished: superbanana resonances and bounce resonances. If the average toroidal precession velocity $\langle \dot{\varphi} \rangle_b$ vanishes, implying that electric and magnetic drift sum up to zero, and if $l = 0$, the resonance condition for trapped particles becomes the superbanana resonance

$$\langle \Omega_{tB} \rangle_b + \langle \Omega_{tE} \rangle_b = 0, \tag{8.12}$$

and the transit resonance for passing particles

$$q\omega_b + \langle \Omega_{tB} \rangle_b + \langle \Omega_{tE} \rangle_b = 0. \tag{8.13}$$

Hence, for a non-axisymmetric perturbation a new kind of orbit arises, where the motion is trapped within the resonance. Here, secular perturbation theory applies. If $l \neq 0$, the resonance is called *bounce resonance* and corresponds to a resonance of the bounce frequency ω_b with the bounce-averaged toroidal drift frequency.

For further analysis, the energy was calculated using

$$E = \frac{mv^2}{2} + e\Phi \approx \frac{mv^2}{2}, \tag{8.14}$$

the last expression is valid in the approximation as we assume the electric potential to be small, what is true for sub-sonic rotations.

Following chapter 2, resonant actions are defined,

$$J_1 = J_\perp = \bar{J}_1 + m_1 \bar{J} = \bar{J}_1 \text{ (gyro-harmonic } m_1 \text{ is zero)}, \tag{8.15}$$
$$J_2 = J_\vartheta = \bar{J}_2 + m_2 \bar{J}, \tag{8.16}$$
$$J_3 = p_\varphi = n\bar{J}. \tag{8.17}$$

to calculate $\bar{\Omega}'$,

$$\begin{aligned}
\bar{\Omega}' &= \frac{\partial \bar{\Omega}(\bar{J}_1, \bar{J}_2, \bar{J})}{\partial \bar{J}} = \frac{\partial \bar{\Omega}(J_1, J_2, J_3)}{\partial J_k} \frac{\partial J_k(\bar{J}_1, \bar{J}_2, \bar{J})}{\partial \bar{J}} \\
&= m_2 \frac{\partial \bar{\Omega}}{\partial J_\vartheta} + n \frac{\partial \bar{\Omega}}{\partial p_\varphi} = m_2 \left(\frac{\partial \bar{\Omega}}{\partial E} \frac{\partial E}{\partial J_\vartheta} + \frac{\partial \bar{\Omega}}{\partial \eta} \frac{\partial \eta}{\partial J_\vartheta} \right) + n \frac{\partial \bar{\Omega}}{\partial r_\varphi} \frac{\mathrm{d}r_\varphi}{\mathrm{d}p_\varphi}.
\end{aligned} \tag{8.18}$$

For the analysis of the Chirikov criterion, the resonance width was calculated,

$$\Delta J_\perp = 0, \tag{8.19}$$

$$\Delta E = \frac{\partial E}{\partial \bar{J}} \Delta \bar{J} + \frac{\partial^2 E}{\partial \bar{J}^2} \Delta \bar{J}^2 = \bar{\Omega} \Delta \bar{J} + \frac{1}{2} \bar{\Omega}' \Delta \bar{J}^2 = \frac{1}{2} \bar{\Omega}' \Delta \bar{J}^2, \tag{8.20}$$

$$\Delta p_\varphi = n \Delta \bar{J}. \tag{8.21}$$

At the separatrix, the width in the resonant action is given by Eq. 2.38 and therefore we have

$$\Delta E = \frac{1}{2} \bar{\Omega}' \left(2 \sqrt{H_{\boldsymbol{m}}/\bar{\Omega}'} \right)^2 = \pm 2 H_{\boldsymbol{m}}, \tag{8.22}$$

$$\Delta p_\varphi = \pm 2 n \sqrt{H_{\boldsymbol{m}}/\bar{\Omega}'}. \tag{8.23}$$

Here, instead of the momentum p_φ, the banana tip radius r_φ is used. The resonance width in r_φ is calculated by

$$\Delta r_\varphi = \frac{\partial r_\varphi}{\partial J} \Delta J = \frac{\partial p_\varphi}{\partial J} \frac{\partial r_\varphi}{\partial p_\varphi} \Delta J = \Delta p_\varphi \frac{dr_\varphi}{dp_\varphi}. \tag{8.24}$$

8.2 Application to a circular tokamak

The input data to compute the present results was calculated using NEO-RT [1]. First, a tokamak configuration with circular concentric flux surfaces and typical parameters for a realistic medium sized tokamak has been used. This configuration is representative for a low-collisional plasma with resonant magnetic perturbations. The parameters of the configuration are: major radius $= 1.8\,m$, minor radius $= 0.46\,m$ and $B = 2\,T$ on the magnetic axis.

Fig. 8.1 shows the resonance lines in the $(1/\eta, r_\varphi)$-plane for $E_0 \approx 3\,keV$, normalized with η_{tp} to visualize the analogy to the pendulum. NEO-RT discretizes the radius r_φ, which explains the smearing in the resonance lines. Also, a certain range in E was selected around the cut at E_0.

As for the pendulum with two degrees of freedom, there are trapped and passing resonances in the whole range of r_φ. The particles are trapped for higher η. In contrast to the model, the resonance lines are not symmetric as the canonical frequency for passing particles for the tokamak is not only dependent on the canonical toroidal frequency, but also on the bounce frequency ω_b, whereas the canonical toroidal frequency for trapped particles does not depend on ω_b.
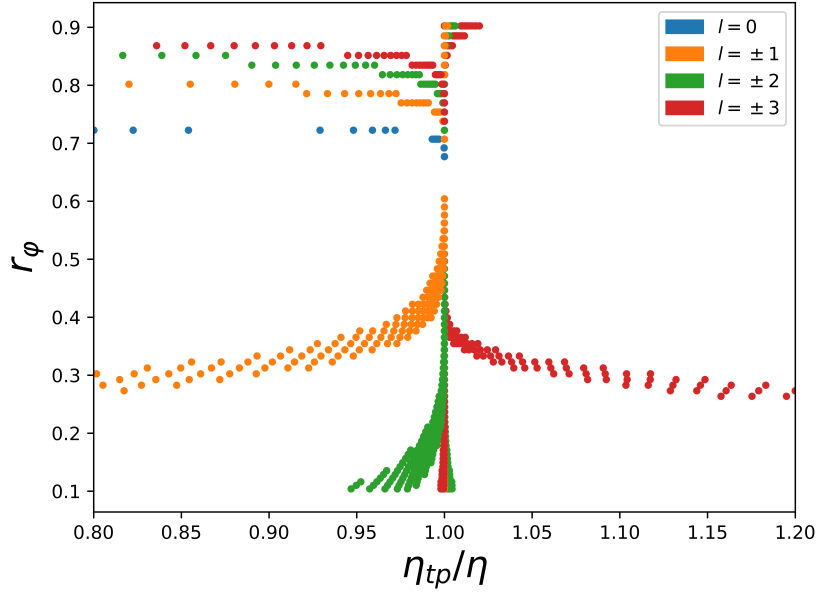
Figure 8.1: Circular tokamak: Resonance lines for $E_0 \approx 3\,keV$ for modes $n = 3$, $l = \{-3, -2, -1, 0, 1, 2, 3\}$ in $(1/\eta, r_\phi)$, normalized with η_{th}.

The superbanana resonance ($l = 0$) occurs only for trapped particles, at $r_\phi \approx 0.69$, where the toroidal electric canonical frequency is $\Omega_{tE} \approx 0$ (Fig. 8.5). Ω_{tE} is related to the radial electric field and at this radius, the radial electric field E_r vanishes. For the superbanana resonance, magnetic and electric drift have to sum up to zero. As usually the $(E \times B)$-drift is significantly bigger than the magnetic drift, this is only possible in this region, where $\Omega_{tE} \approx 0$. In theory, the $l = 0$ resonance can also occur for passing particles, but only very close to the trapped-passing-boundary as there is the additional term dependent on ω_b that is significantly larger than the toroidal canonical frequencies.

Three different cases for the calculation of the resonance lines are considered:

- included electric and magnetic drift,

- without shear,

- without magnetic drift.

In Fig. 8.2, the resonance lines in the (η, r_φ)-plane for $E_0 \approx 3\,keV$ with their corresponding resonance widths are shown. Here, the relation between toroidal precession frequencies, due to the $(E \times B)$-drift and the magnetic drift has been fixed. Additionally, resonance lines for calculations where the magnetic shear term has been neglected in Ω_{tB} are shown in Fig. 8.3. In Fig. 8.4, resonance lines with the magnetic drift neglected ($\Omega_{tB} = 0$) are shown. For all cases, the resonance width in r_φ was calculated using Eq. 8.24.

As discussed in [1], magnetic shear plays a small role for flux surfaces close to the axis, but is significant for flux surfaces further outwards due to the safety factor profile as shown in Fig. 8.5. For larger radii, there is a slight shift of the distance of the resonance lines noticeable compared to Fig. 8.2.

If the magnetic drift is neglected (Fig. 8.4), the bounce frequency is in resonance with the toroidal drift frequency due to the $(E \times B)$-drift. By comparing Fig. 8.2 and Fig. 8.4, the structure of the resonance lines is preserved, however the superbanana resonance does not occur without magnetic drift, as the resonance condition cannot be satisfied.

As evident in all plots, trapped resonances for outer radii are overlapping with the separatrix and with neighbouring resonance lines. Therefore, the motion is expected to become stochastic as the particle can pass from one resonance in l to another. Naturally, the motion is unstable at the separatrix. The same behaviour was observed for the two-dimensional pendulum (Fig. 6.9). For outer radii there are naturally more and also closer spaced resonance lines possible, as the radial electric field E_r is very steep and passes through a big interval as shown in Fig. 8.5.

For the comparison with the standard map, the stochasticity parameter K that estimates the overlap of resonances was calculated. In Fig. 8.6, the calculated stochasticity parameter for resonance lines for trapped orbits in the (η, r_φ)-plane is shown in dependence on r_φ and η. The behaviour of K here is analogous to the pendulum (Fig. 6.11). At the separatrix, $K \to \infty$, because of the asymptotic behaviour of $\bar{\Omega}$ and the increasing bounce time τ_b. Especially the motion near the separatrix of a non-linear resonance is important to investigate. As shown in [5], even for an arbitrarily small perturbation the motion is stochastic in the so-called stochastic layer in the vicinity of the separatrix. This layer occurs naturally as even small perturbations may change the kind of motion, libration or rotation. Here, the simplest form of the overlap criterion as presented in chapter 4 was used as the resonance widths are also calculated in lowest order. K exceeds the critical value of $K_{\text{crit}} \approx 2.5$ when the particle is close to the separatrix and/or resonance lines are overlapping.

In Fig. 8.7, the resonance lines for $n = 3$ for the (η, E)-plane for a fixed value of the radius $r_\varphi = 0.22$ are shown. They converge at the separatrix, denoted by the black solid line. As $\Omega_{tE} = \text{const.}$ for $r_\varphi = \text{const.}$, the scaling variable is Ω_{tB} being proportional to E.
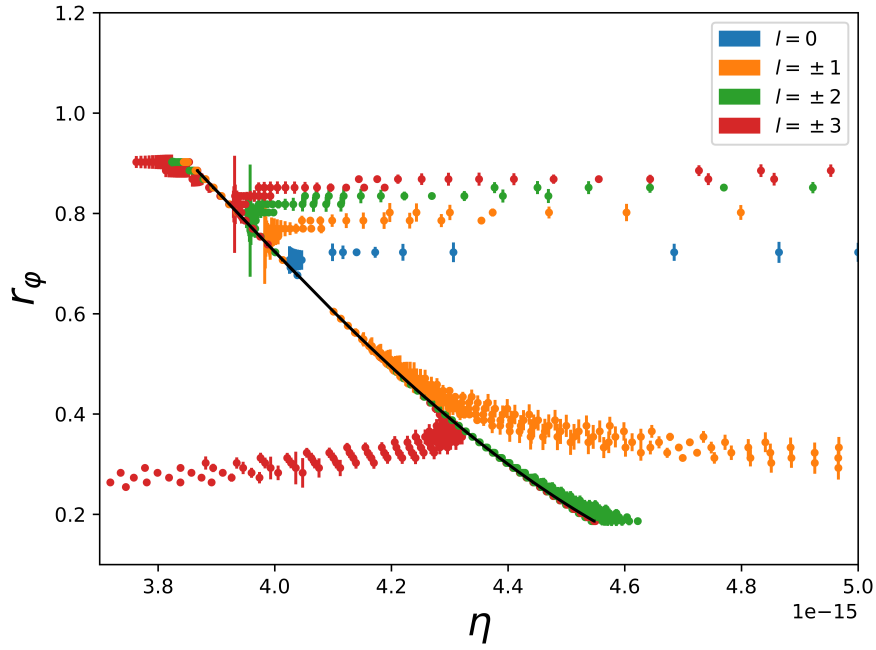
Figure 8.2: Circular tokamak: Resonance lines for $E_0 \approx 3\,keV$ for modes $n = 3$, $l = \{-3, -2, -1, 0, 1, 2, 3\}$ in (η, r_φ) with the corresponding resonance width calculated using Eq. 8.24. The separatrix is denoted by the black line.
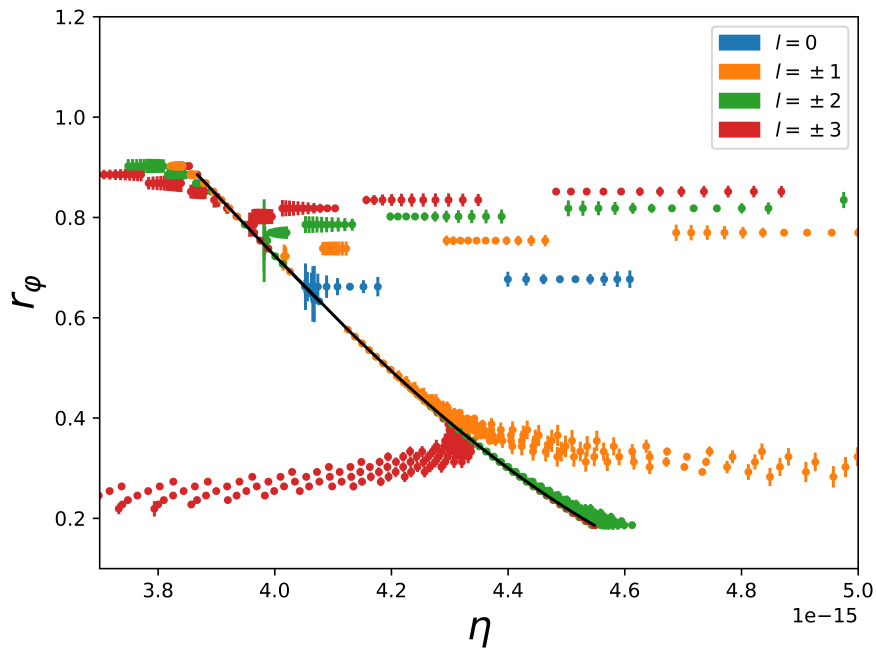
Figure 8.3: Circular tokamak: Resonance lines **without magnetic shear** with parameters as in Fig. 8.2.
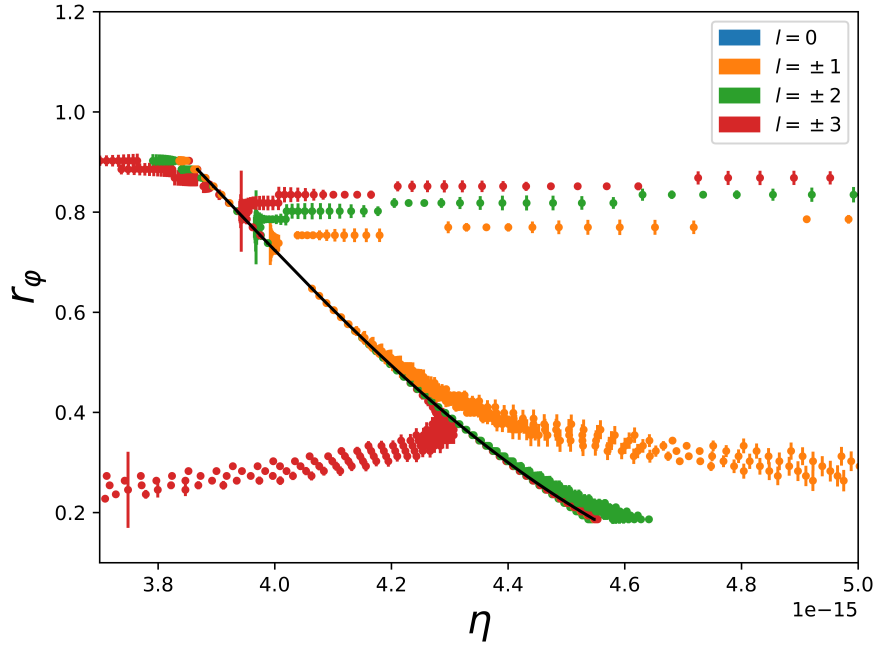
Figure 8.4: Circular tokamak: Resonance lines **without magnetic drift** with parameters as in Fig. 8.2.
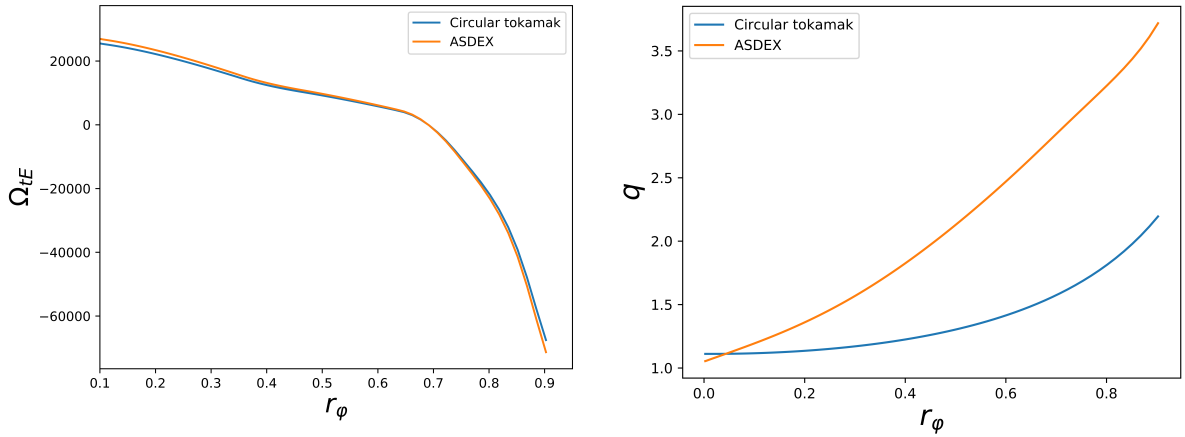
Figure 8.5: Left: Toroidal electric rotation frequency Ω_{tE} in dependency on r_φ for the circular tokamak and ASDEX Upgrade. At $r_\varphi \approx 0.69$, Ω_{tE} changes its sign, as the radial electric field $E_r = 0$. Right: Safety factor q in dependency on r_φ for the circular tokamak and ASDEX Upgrade.
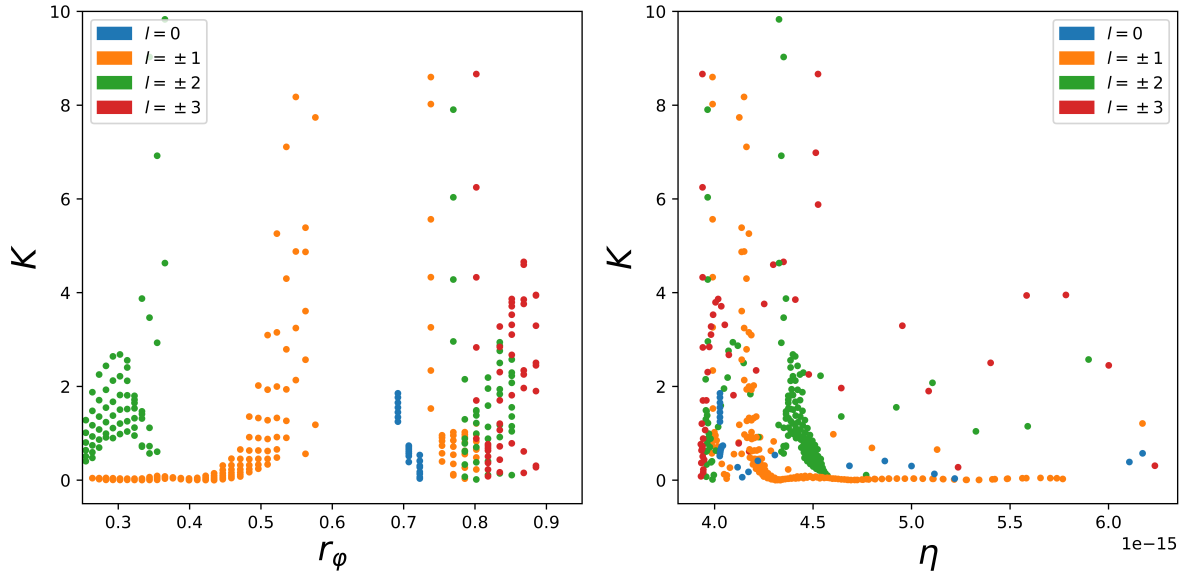
Figure 8.6: Stochasticity parameter K for resonance lines $l = [-3, -2, -1, 0, 1, 2, 3]$, $n = 3$ for $E_0 \approx 3\,keV$ in dependence on r_φ and η in the left and right plot respectively.
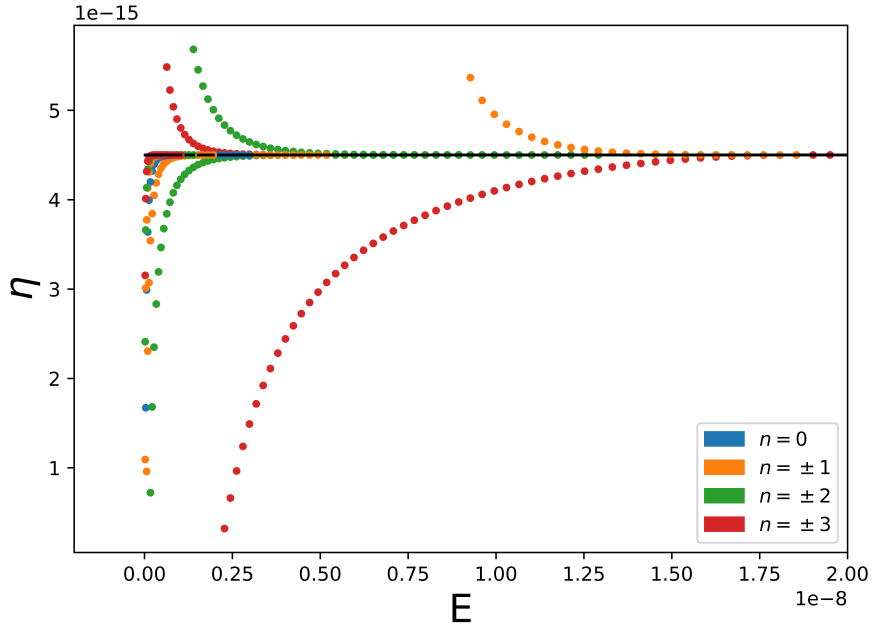
Figure 8.7: Resonance lines for $r_\varphi = 0.22$ for modes $n = 3$, $l = \{-3, -2, -1, 0, 1, 2, 3\}$ in (E, η) with the corresponding resonance width calculated using Eq. 8.22. The separatrix is denoted by the black line.

8.3 Application to experiments on ASDEX Upgrade

Drift-orbit resonances have been computed for a perturbed tokamak equilibrium based on experiments on ASDEX Upgrade in a low-collisional plasma with RMPs by ELM mitigation coils using NEO-RT. The used data is the same as in [20].

Fig. 8.8 pictures the normalized resonance lines for $E_0 \approx 3\,keV$ for the mode $n = 3$ in $(1/\eta, r_\phi)$. Again, the structure of the resonance lines is similar to the ones of the pendulum and resonances can be found in the whole range of r_φ. By comparing Fig. 8.1 and 8.8, it is evident that the resonance lines for smaller radii differ both in range and shape due to the different profile of the safety factor for inner radii. For outer radii, the resonance lines are similar for the circular tokamak and ASDEX Upgrade as the difference in the profile of the safety factor gets smaller.

Again, three different cases are considered: first, calculation with both electric and magnetic drift included, but with fixed ratio (Fig. 8.9), second, with neglected shear (Fig. 8.10) and third, with neglected magnetic drift (Fig. 8.11). As for the circular tokamak, the resonance lines computed for the different cases are similar in structure, but with a big difference in the resonance widths (calculated by Eq. 8.24) as both, magnetic drift and shear have an influence on $\bar{\Omega}'$. As the shear is stronger in ASDEX Upgrade (Fig. 8.5), the neglection of the magnetic shear has a stronger influence on the resulting resonance lines.

In comparison to the circular tokamak, the overlap of the resonance lines is bigger, as the resonance width is proportional to $H_{\boldsymbol{m}}$ and the perturbation for ASDEX Upgrade is bigger than for the circular tokamak as depicted in Fig. 8.13 (different scaling).

Also the stochasticity parameter K is calculated (Fig. 8.12). Here, the same arguments are valid as for the circular tokamak.
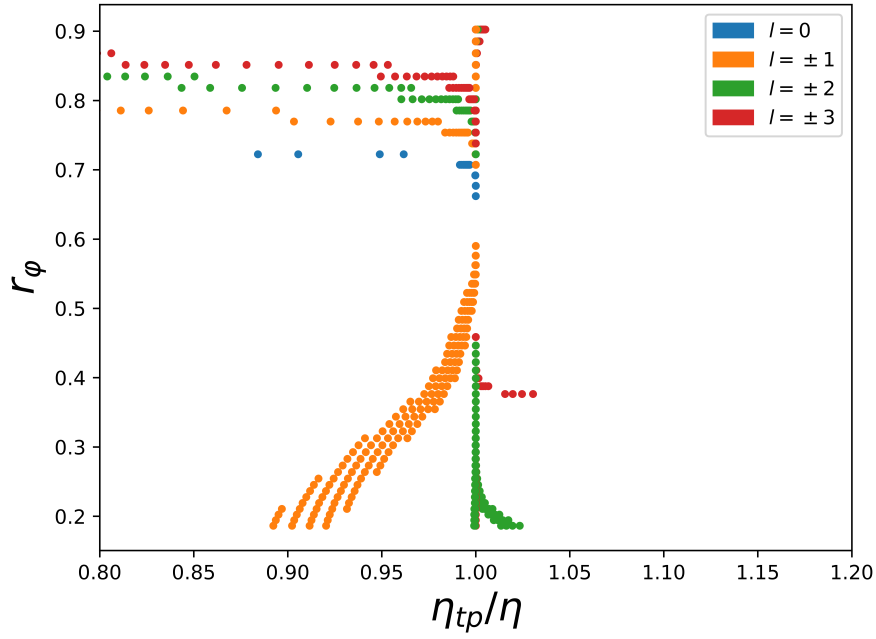
Figure 8.8: ASDEX Upgrade: Resonance lines for $E_0 \approx 3\,keV$ for modes $n = 3$, $l = \{-3, -2, -1, 0, 1, 2, 3\}$ in $(1/\eta, r_\phi)$, normalized with η_{th}.
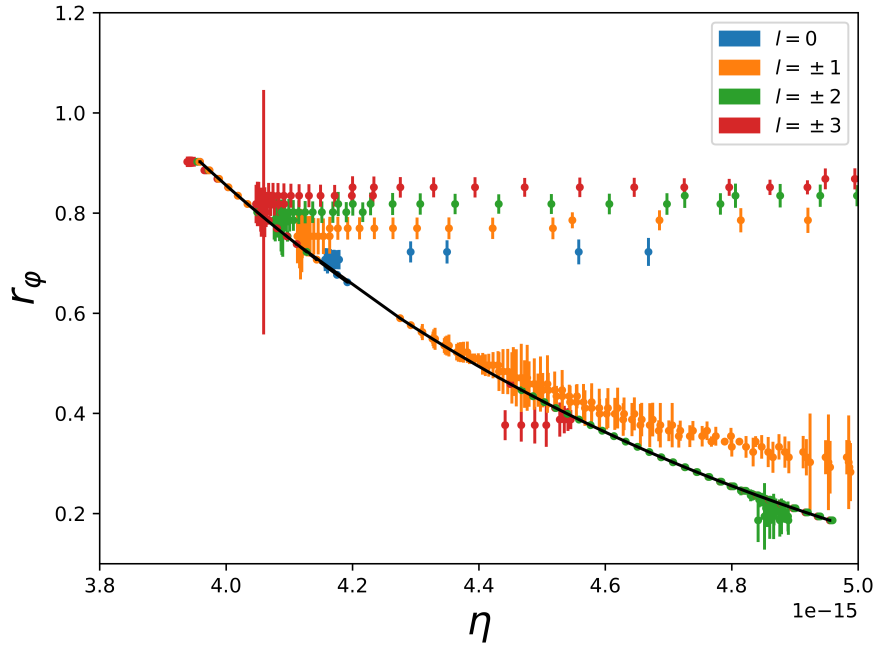
Figure 8.9: ASDEX Upgrade: Resonance lines for $E_0 \approx 3\,keV$ for modes $n = 3$, $l = \{-3, -2, -1, 0, 1, 2, 3\}$ in (η, r_φ) with the corresponding resonance width calculated using Eq. 8.24. The separatrix is denoted by the black line.
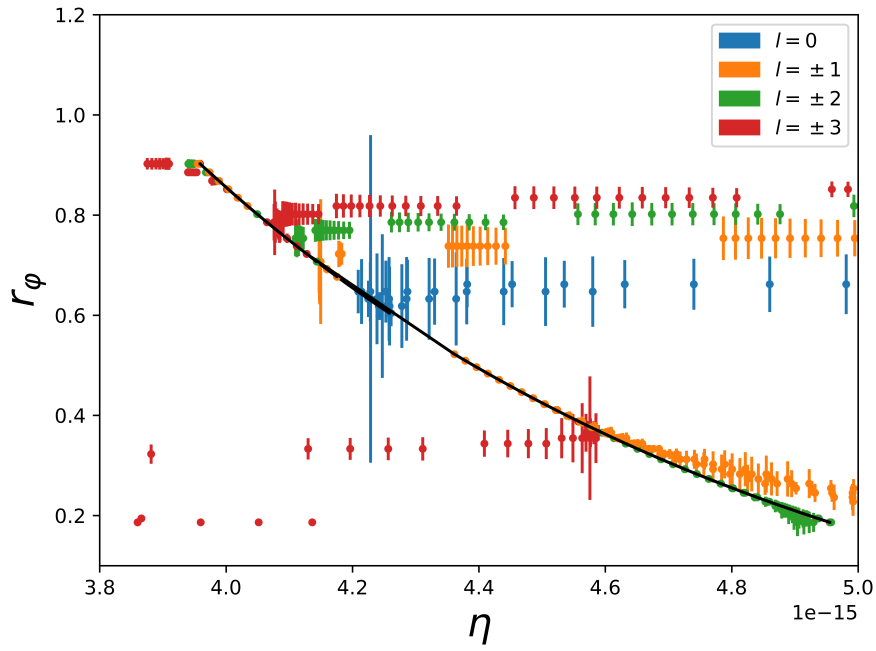
Figure 8.10: ASDEX Upgrade: Resonance lines **without magnetic shear** with parameters as in Fig. 8.9.
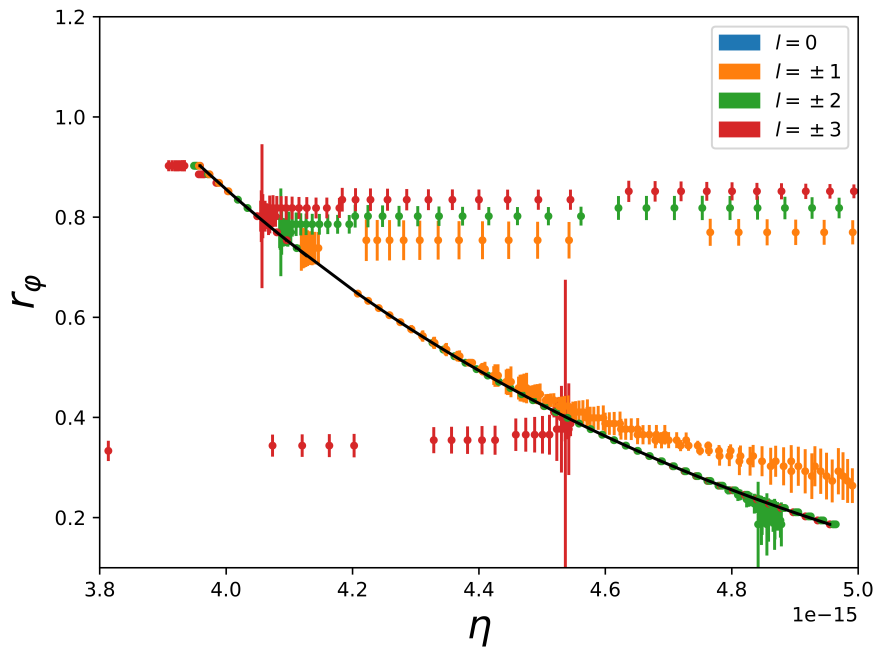
Figure 8.11: ASDEX Upgrade: Resonance lines **without magnetic drift** with parameters as in Fig. 8.9.
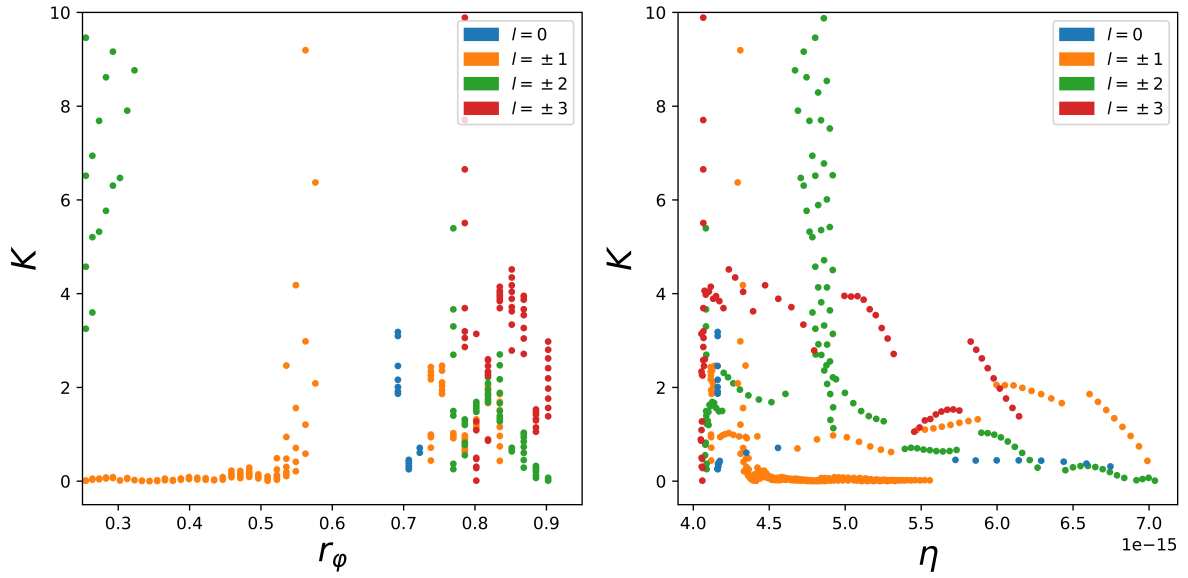
Figure 8.12: ASDEX Upgrade: Stochasticity parameter K for resonance lines $l = [-3, -2, -1, 0, 1, 2, 3]$, $n = 3$ for $E_0 \approx 3\,keV$ in dependence on r_φ and η in the left and right plot respectively.
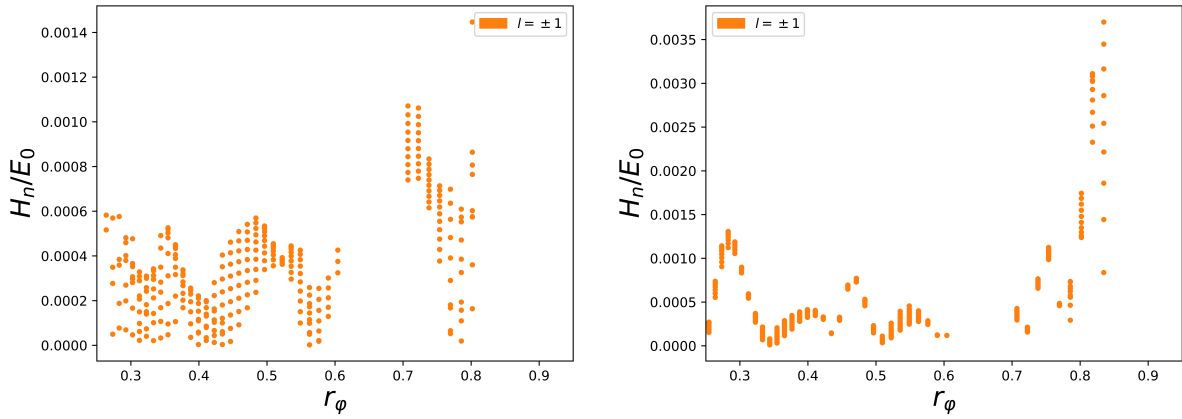
Figure 8.13: Left: Toroidal harmonics H_n of the perturbation normalized with E_0 for the circular tokamak. Right: Toroidal harmonics H_n of the perturbation normalized with E_0 for ASDEX Upgrade.

Chapter 9

Summary

Within this thesis, an analysis of the width and distance of drift-orbit resonances of NEO-RT [1] for a typical medium sized tokamak for a low-collisional plasma with resonant magnetic perturbations has been performed. Resonance overlap and the subsequent appearance of chaotic motion has been studied to test the validity range of NEO-RT. The stability analysis relies upon the Chirikov criterion of resonance overlap and is enhanced by the comparison with the standard map.

The pendulum was introduced as an example of a non-linear oscillator with the property of non-isochronicity. For an external perturbtion and using secular perturbation theory, it was found that for a non-linear oscillator, the motion is bounded under small perturbations around the resonance and is hence stabilized. Free oscillations of a pendulum simulate the phenomenon of a single, well-separated resonance as shown by the *standard Hamiltonian*. However, in non-linear systems the non-linear stabilization is destroyed and stochasticity arises if resonances are interacting and not well-separated.

Two concepts to study resonance overlap were presented: the overlap criterion by [4] and the standard map. The overlap criterion estimates the border of stability by the width and distance of the resonances. It states that as long as the separatrices of two neighbouring resonances do not touch each other, the motion is stable. The standard map, on the other hand, represents the system of a kicked rotator and applies only to an infinite set of resonances of the same amplitude.

To discuss the applicability of the standard map for the presented system, numerical experiments were performed. The exact equations of motion for the $(\Delta \bar{J}, \bar{\theta})$ phase space were compared to the standard map and it was found that even though the standard map describes a set of equidistant resonances of the same amplitude, there is a good correspondence. Also, an analysis on the resonance width was performed by using secular perturbation theory. For the pendulum with two degrees of freedom, it was shown, that resonance lines for trapped particles start overlapping not only with the separatrix but also with neighbouring resonances depending on the perturbation amplitude. It was concluded that this results in stochastic motion, as particles can now pass from one resonance to another. Moreover, the stochasticity parameter K was calculated and

it was found that the degree of chaos in the system increases while approaching the separatrix.

For the application of the method in the tokamak, Hamiltonian theory in the tokamak was presented along with a sketch of guiding center theory. It was shown that the guiding center Hamiltonian can be approximated by an Hamiltonian similar to the pendulum Hamiltonian. Therefore, particle motion in a large aspect ratio tokamak is analogous to the motion of a pendulum, where trapped and passing motion correspond to libration and rotation.

Finally, data for drift-orbit resonances from NEO-RT were analysed with respect to resonance overlap and stability. Two setups were used: first, a tokamak configuration with circular concentric flux surfaces and typical parameters for a realistic medium sized tokamak for a low-collisional plasma and second, equilibria from the experiment ASDEX Upgrade with resonant magnetic perturbations. It was shown that for outer radii r_φ, resonance lines for trapped orbits are overlapping with each other and the separatrix. Hence, non-linear theory that assumes well-separated resonances is not applicable there. Further analysis taking collisions into account is required. For inner radii, non-linear theory should be applicable in this form.

Appendix A

Lie transformation method

Following the procedure presented in Chapter 1 that uses generating functions for canonical transformations, we arrive at some difficulties when expanding to higher orders in the perturbation parameter ϵ. As the generating functions of the canonical transformation are mixed functions of the old and the new variables, the inverse of the transformation equations can hardly be calculated. Moreover, it is not possible to set additional restrictions to the transformation, such as eliminiation of certain variables or analytical coefficients. A new method was introduced to calculate the transformation in an explicit form and without mixed variables [3, 18]. Using the *Lie transformation method*, the old variables x can be expressed in series of the new variables $\bar{x}$ (and vice versa) with repeating Poisson brackets.

A Lie generating function $w(\bar{x},\epsilon)$ is a function satisfying,

$$\frac{d\bar{x}}{d\epsilon} = [\bar{x},w], \tag{A.1}$$

which components are in principle only Hamilton's equation in Poisson bracket notation and $x = (p, q)$ representing canoncial variables. Therefore, a transformation generated by Eq. A.1 is always canonical. We introduce an evolution operator T to evaluate the initial position and momenta at the transformed point,

$$\bar{x} = Tx. \tag{A.2}$$

Using the Lie operator L,

$$L = [w,], \tag{A.3}$$

Eq. A.1 can be rewritten as,

$$\frac{dT}{d\epsilon} = -TL, \tag{A.4}$$

yielding the solution for T,

$$T = \exp[-\int_\epsilon L(\epsilon')d\epsilon'].$$ (A.5)

The transformed Hamiltonian $\bar{H}(\bar{x}(x,\epsilon))$ is related to the original Hamiltonian H via

$$\bar{H}(\bar{x}(x,\epsilon)) = H(x).$$ (A.6)

If the Hamiltonian is not explicitly time-dependent, we get from Eq. A.2

$$\bar{H} = T^{-1}H,$$ (A.7)

whereas for time-dependent systems, we get an additional term that takes into account that the energies of the old and the new Hamiltonian are not equal,

$$\bar{H} = T^{-1}H + T^{-1}\int_0^\epsilon d\epsilon' T(\epsilon')\frac{\partial w(\epsilon')}{\partial t}.$$ (A.8)

From the general transformation theory, we construct a method for perturbation as done in Ref. [6]. We expand w, L, T, H and $\bar{H}$ as power series in ϵ and insert those expressions into A.8 to get explicit expressions for the nth-order term of the transformation.

For H, $\bar{H}$ and T we have,

$$H = \sum_{n=0}^{\infty} \epsilon^n H_n,$$ (A.9)

$$\bar{H} = \sum_{n=0}^{\infty} \epsilon^n \bar{H}_n,$$ (A.10)

$$T = \sum_{n=0}^{\infty} \epsilon^n T_n,$$ (A.11)

but we assume a different form for w as the integration in Eq. A.8 will increase the order to w by 1. As the map $w \to L(w)$ is linear, this form also applies to L,

$$w = \sum_{n=0}^{\infty} \epsilon^n w_{n+1},$$ (A.12)

$$L = \sum_{n=0}^{\infty} \epsilon^n L_{n+1}.$$ (A.13)

To get explicit expressions for T and T^{-1}, the series representations are inserted into Eqn. A.4 and result in,

$$T_n = -\frac{1}{n}\sum_{m=0}^{n-1} T_m L_{n-m}, \tag{A.14}$$

$$T_n^{-1} = \frac{1}{n}\sum_{m=0}^{n-1} L_{n-m} T_m^{-1}. \tag{A.15}$$

Using Eq. A.8, multiplying it by T, differentiating with respect to ϵ and again multiplying it by T^{-1}, we arrive at,

$$\frac{\partial w}{\partial t} = \frac{\partial \bar{H}}{\partial \epsilon} - L\bar{H} - T^{-1}\frac{\partial H}{\partial \epsilon}. \tag{A.16}$$

Now we insert the series expansions for $\bar{H}$, H and T, we get,

$$\frac{\partial w}{\partial t} = n\bar{H}_n - \sum_{m=0}^{n-1} L_{n-m}\bar{H}_m - \sum_{m=1}^{n} mT_{n-m}^{-1}H_m. \tag{A.17}$$

Due to the definition of the Lie operator L, terms of the sum can be rewritten,

$$L_n\bar{H}_0 = L_n H_0 = [w_n, H_0], \tag{A.18}$$

where the last term is $nT_0^{-1}H_n = nH_n$, as $T_0 = T_0^{-1} = 1$. We can combine the sums and get,

$$\frac{\partial w}{\partial t} + [w_n, H_0] = n(\bar{H}_n - H_n) - \sum_{m=1}^{n-1}(L_{n-m}\bar{H}_m + mT_{n-m}^{-1}H_m). \tag{A.19}$$

Defining $D_0 = \frac{\partial}{\partial t} + [, H_0]$, Eq. A.19 can be written in the following from up to third order,

$$D_0 w_1 = \bar{H}_1 - H_1, \tag{A.20}$$

$$D_0 w_2 = 2(\bar{H}_2 - H_2) - L_1(\bar{H}_1 - H_1), \tag{A.21}$$

$$D_0 w_3 = 3(\bar{H}_3 - H_3) - L_1(\bar{H}_2 - 2H_2) - L_2(\bar{H}_1 - \frac{1}{2}H_1) - \frac{1}{2}L_1^2 H_1. \tag{A.22}$$

Eq. A.22 are called Deprit's equations and give perturbation terms for arbitrary orders.

Bibliography

[1] C. Albert. *Hamiltonian Approach to Resonant Transport Regimes due to Non-Axisymmetric Magntic Perturbations in Tokamak Plasmas*. PhD thesis, Technische Universiät Graz, 2017.

[2] A. J. Brizard. Action-angle coordinates for the pendulum problem. *ArXiv e-prints*, Aug. 2011.

[3] J. R. Cary. Lie transform perturbation theory for hamiltonian system. *Physics Reports*, 79(2):129–159, 1981.

[4] B. V. Chirikov. Resonance processes in magnetic traps. *Journal of Nuclear Energy. Part C, Plasma Physics, Accelerators, Thermonuclear Research*, 1(4):253, 1960.

[5] B. V. Chirikov. A universal instability of many-dimensional oscillator systems. *Physics Reports*, 52(5):263 – 379, 1979.

[6] A. Deprit. Canonical transformations depending on a small parameter. *Celestial mechanics*, 1(1):12–30, 1969.

[7] W. D'haeseleer. *Flux coordinates and magnetic field structure: a guide to a fundamental tool of plasma structure*. Springer series in computational physics. Springer-Verlag, 1991.

[8] A. J. Dragt and J. M. Finn. Insolubility of trapped particle motion in a magnetic dipole field. *Journal of Geophysical Research*, 81(13):2327–2340, 1976.

[9] H. Goldstein, C. Poole, and J. Safko. *Classical Mechanics*. Addison Wesley, 2002.

[10] J. M. Greene. Two-dimensional measure-preserving mappings. *Journal of Mathematical Physics*, 9(5):760–768, 1968.

[11] J. M. Greene. A method for determining a stochastic transition. *Journal of Mathematical Physics*, 20(6):1183–1201, 1979.

[12] F. Izraelev. Nearly linear mappings and their applications. *Physica D: Nonlinear Phenomena*, 1(3):243 – 266, 1980.

[13] E. Jackson. *Perspectives of Nonlinear Dynamics:*. Perspectives of Nonlinear Dynamics. Cambridge University Press, 1991.

[14] J. José and E. Saletan. *Classical Dynamics: A Contemporary Approach*. Cambridge University Press, 1998.

[15] W. Kernbichler, S. V. Kasilov, G. Kapper, A. F. Martitsch, V. V. Nemov, C. Albert, and M. F. Heyn. Solution of drift kinetic equation in stellarators and tokamaks with broken symmetry using the code neo-2. *Plasma Physics and Controlled Fusion*, 58(10):104001, 2016.

[16] A. Khinchin and H. Eagle. *Continued Fractions*. Dover books on mathematics. Dover Publications, 1964.

[17] C. N. Lashmore-Davies. Collisional transport in magnetized plasmas, by per helander and dieter j. sigmar, cambridge monograph on plasma physics, cambridge university press (2002) -. *Journal of Plasma Physics*, 70(4):501–502, 2004.

[18] A. Lichtenberg and M. Lieberman. *Regular and chaotic dynamics*. Applied mathematical sciences. Springer-Verlag, 1992.

[19] R. G. Littlejohn. Variational principles of guiding centre motion. *Journal of Plasma Physics*, 29(1):111–125, 1983.

[20] A. Martitsch, S. Kasilov, W. Kernbichler, G. Kapper, C. Albert, M. Heyn, H. Smith, E. Strumberger, S. Fietz, W. Suttrop, et al. Asdex upgrade team, and eurofusion mst1 team. *Plasma. Phys. Controlled Fusion*, 58:074007, 2016.

[21] R. A. M. Todd E. Evans. Edge stability and transport control with resonant magnetic perturbations in collisionless tokamak plasmas. *Nature Physics 2*, 4(1):419 – 423, 2006.